Multiscale Simulation and Experimental Analysis of Zn Growth Process on Secondary Battery Negative Electrodes

Zn二次電池負極におけるZn析出成長のマルチスケールシミュレーション及び実験的解析

July, 2022

Yusuke ONABUTA
女部田　勇介

Multiscale Simulation and Experimental Analysis of Zn Growth Process on Secondary Battery Negative Electrodes

Zn二次電池負極におけるZn析出成長のマルチスケールシミュレーション及び実験的解析

July, 2022

Waseda University Graduate School of Advanced Science and Engineering

Department of Applied Chemistry, Research on Functional Surface Chemistry

Yusuke ONABUTA
女部田　勇介

Contents

Chapter 1:

General Introduction

1.1. Requirements of large-scale energy storage devices

1.1.1. Large-scale energy storage for the use of renewable energies and demand responses

Currently, global climate change is observed all over the world, which is due to the effects of greenhouse gases by increased carbon dioxide emissions, and it is required to reduce them. In 2015, Sustainable Development Goals (SDGs) was adopted by the United Nations to maintain our world sustainable, and they compose of 17 goals for the next generation [1]. Especially, Goal 7: Affordable and clean energy and Goal 13: Climate change remind us to make the actions. In this context, power generation accounts for a large share of CO_2 emissions, and as of fiscal year (FY) 2019, CO_2 emissions from the sector of electricity and energy sources conversion including power plants and oil refinery amounted to approximately 39% in Japan [2]. The most effective means of transforming power generation into something cleaner is the use of renewable energy. In a broad sense, renewable energy refers to energy derived from solar, geophysical, and biological sources and replenished by nature at a rate faster than it is used [3,4]. Specifically, power is generated from energy resources that are constantly (or repeatedly) replenished by natural forces, such as solar power, wind power, wave and tidal power, running water and tides, geothermal power, and biomass [4]. However, the instability of the power supply is a general challenge to the spread of these renewable energies. In FY2020, the annual amount of electricity generated by solar power in Japan was only approximately 8.9% [5], which reflects the difficulty of the use of the renewable energy. Since solar power generation varies between daytime and nighttime, with an oversupply during the day and a shortage at night, it is required to be balanced in daytime and nighttime. The introduction of solar power can cause the introduction of distributed power sources that can work as small power plants at several places such as factories, offices, and houses, but in such a situation there is also a problem of fine frequency fluctuations [6], which are due to fluctuations in the output of renewable energy. Large-scale energy storage devices can be an effective approach to these

challenges. In order to balance the demand and supply in daytime and nighttime, excess daytime power supply can be stored and used at night, and frequency fluctuations can be absorbed and adjusted, thus simultaneously storing excess power and adjusting electricity frequencies [7-10]. This will lead to the spread of the use of renewable energy.

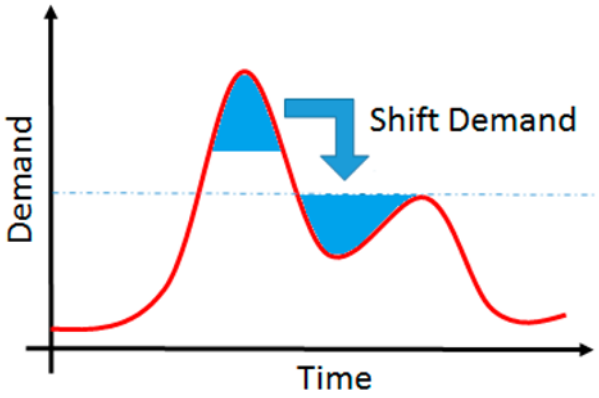

Figure 1.1. Concept of demand response [11].

To address the instability of the use of renewable energy and improve the efficiency of energy as a whole, a new approach for adjusting the balance of electricity supply and demand, called Demand Response (DR), has been developed [11-13]. DR is claimed to be defined as: “Changes in electric use by demand-side resources from their normal consumption patterns in response to changes in the price of electricity, or to incentive payments designed to induce lower electricity use at times of high wholesale market prices or when system reliability is jeopardized” [14]. Electricity demand and supply must always match in order to achieve a balance between supply and demand. Until now, power companies (thermal power plants, etc.) on the supply side have adjusted the amount of electricity generated, but with DR, it is possible to actively control electricity consumption on the demand side and contribute to adjusting the supply-demand balance. Thus, in DR, it is important to change electricity demand patterns. In particular, suppliers allow consumers to participate in the electricity system by "setting electricity rates by time of day" and "paying compensation to consumers who use less during peak hours" [11,12]. In this approach, each small-scale distributed energy resource owned by factories and households will be remotely integrated and controlled by aggregators with advanced energy management technology using the

Internet of Things (IoT) to adjust the supply-demand balance of electric power. As the entire system functions as if it were a single power plant, this system is called a virtual power plant (VPP) [15-19]. VPPs are expected to play an active role in the power system as a function of load leveling, absorption of renewable energy oversupply, and supply during power shortages. The current supply flow of electricity, as described above, is generally one-direction by power companies using electricity produced at power plants. In this case, power is supplied unilaterally and used by consumers, and the issues of power shortages or excesses is handled solely by the power company. On the other hand, as mentioned above, the consumers can also play a role in adjusting the supply and demand of electricity in a VPP. At this time, the owner of the energy storage can contribute to maintaining the balance of the energy supply, i.e., charge and discharge the storage devices will allow consumers to have the same functionality as a power plant.

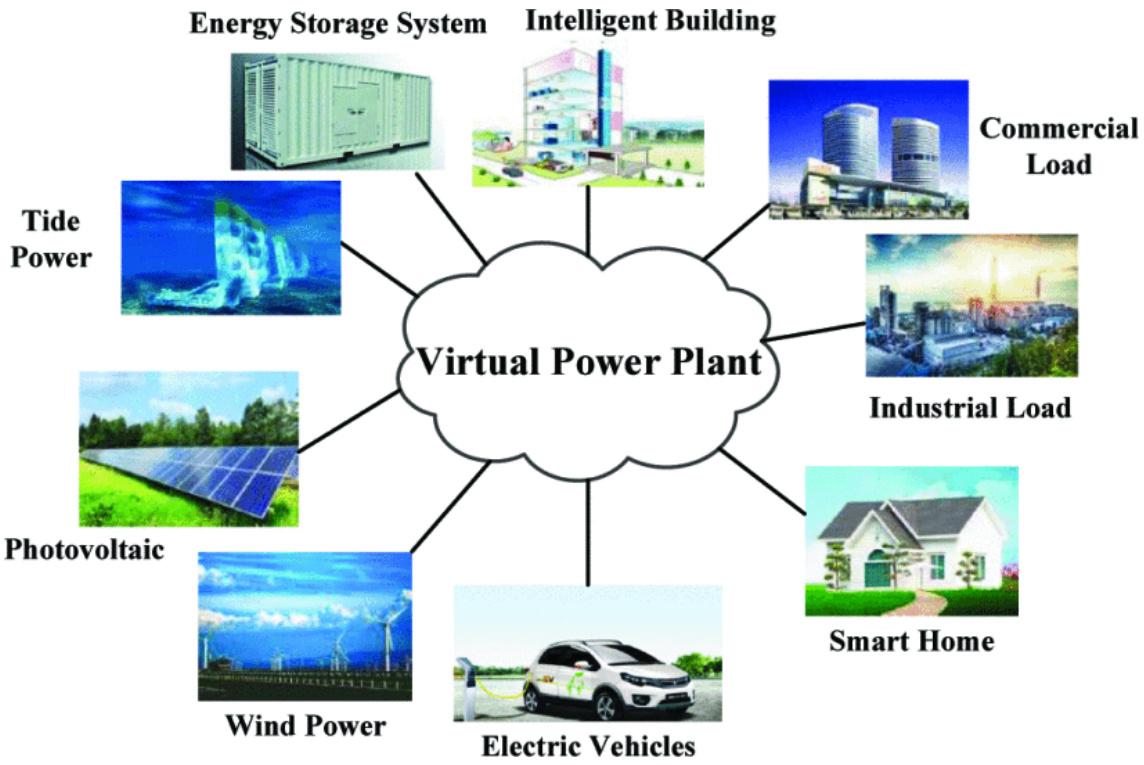

Figure 1.2. Cocept of virtual power plant [20].

Devices capable of adjusting the power by charge-discharge at the consumer's end are essential to match the power supply from the power plant. Large-scale storage batteries are important for this power supply and demand system [8,10,21-23]. For example, it is possible to temporarily store electricity from renewable energy sources at the consumer side and release it according to the electricity supply-demand balance. The unstable supply of renewable energy can also be solved by introducing large-scale storage batteries. When conditions are favorable for charging the devices in daytime, consumers can recharge the large-scale storage batteries, and when the amount of generated electricity is low, the discharge of the batteries can lead to save the electricity fee and the efficient use of the electricity on the consumer side. This is expected to increase the use of renewable energy in society as a whole and move us toward solving problems caused by power generation, such as carbon dioxide emissions. Demand for large-scale storage batteries has been increasing; as an example, the market size of stationary batteries in Japan in 2018 was worth 300 billion yen [24]. In FY2019, the cost of an energy storage system for house-use was around 140,000 yen/kWh. The average price of energy storage systems for business and industry was now 98,000 yen/kWh, and further cost reductions are important in the future. The conditions required for these large-scale storage batteries differ depending on the application. For applications for load leveling, it is necessary to deal with fluctuation control, peak shaving, and peak shifting. Each application requires storage batteries with different capacities and outputs [21-23].

1.1.2. Types of the present large-scale energy storage devices

The following specific types of batteries are known as large-scale storage batteries; a) Li-ion batteries, b) redox flow batteries, c) sodium sulfur batteries, and d) lead-acid batteries, etc.

a) Li-ion batteries are currently the most popular battery, and their use is expanding for mobile applications and power storage. It is capable of rapid recharging, has low self-discharge, and is easy to monitor the state of charge. On the other hand, the

electrolyte is a flammable liquid [25], and large-volume installations of Li-ion batteries will face with the safety for the use of such electrolyte [26,27]. For this reason, extremely delicate management and control of charging voltage is required during charging. The considerable skills are required for control design, including protection circuits [28]. The main materials used for the positive electrode are transition metal oxides and polyanion compounds which has a space for intercalation of Li. The conversion materials are mainly made of fluorides, chlorides, and lithium sulfides. The main materials used for the negative electrode are graphite and lithium titanium oxide [29].

b) Redox flow batteries that utilize vanadium as the battery material are widely used [10]. In addition, redox flow batteries have been reported to operate at room temperature with little degradation [30]. The main characteristics of this battery can be an extremely long charge-discharge cycle life of more than 10,000 cycles, instantaneous responsiveness on the millisecond level, and the ability to produce several times larger output for a short period of time than expected when it is designed [31]. On the other hand, the energy density is low and the need for a pump to circulate the electrolyte makes the equipment complicated [32-34].

c) Sodium sulfur batteries are MWh-class storage batteries commercialized by NGK, which is developed for load leveling, output stabilization, and a backup power source [35]. It uses sulfur for the cathode, sodium for the negative electrode, and aluminum oxides for the electrolyte. These materials are abundant in resources, which leads to cost reduction in mass production. However, there are some drawbacks, such as the need to maintain the temperature at around 300°C during operation, which requires extra electricity for heat retention, and the difficulty of extinguishing a fire once it starts.

d) Lead-acid batteries have been widely used. They are also considered to be already mature. The main constituent material utilizes PbO_2 on the cathode side and Pb on the negative electrode side; $PbO_2 + Pb^+ 2H_2SO_4 \rightarrow 2PbSO_4 + 2H_2O$ is the overall discharge reaction [36].

1.2. Zn negative electrode for the large-scale energy storage

1.2.1. Characteristics of Zn negative electrodes

A Rechargeable batteries with Zn negative electrode are one of the promising batteries for the large-scale storage batteries as well as the ones described above. Zn secondary batteries are expected as a baseload device that can provide a stable supply of wind and photovoltaic power energy at low cost. The main advantages are high energy density, safety, and material abundance [37-40]. The specific energy density is 820 mAh g^{-1} and the capacity density is about 5850 mAh cm^{-3} [40-44]. It can achieve a volumetric energy density equivalent to that of a stationary lithium-ion battery. (about 200 watt-hours per liter of battery volume). In addition, Zn secondary batteries use an aqueous solution instead of flammable organic solvents in the electrolyte, which makes the battery operation safer [37].

The metal-air batteries using Zn and other negative electrodes are shown in Table 1.1, which shows the theoretical voltage, specific energy density, volumetric energy density, and other important properties of various metal-air batteries. Among the metals listed in Table 1.1, Zn is expected to be widely used as a negative electrode material due to its abundance, cost competitiveness, environmental friendliness, high capacity, and stability in aqueous electrolyte [45-49].

Table 1.1. Physical properties for various metal negative electrodes [50]

Negative electrode materials for metal-air batteries	Reduction potential / V vs. SHE	Volumetric capacity / mA h cm^{-3}	Specific capacity / mA h g^{-1}
Zn	−0.8	5851	820
Li	−3.0	2062	3861
Na	−2.7	1128	1166
Mg	−2.4	3833	2205
Al	−1.7	8046	2980
Fe	−0.44	23376	2974

Compared to current lithium-ion batteries, the material of the Zn secondary battery is particularly inexpensive [37,38]. For example, the price difference of Zn with cobalt and molybdenum, which is the typical materials for the positive and negative electrodes of Li-ion batteries is as much as 10 times (Co: $30,000-100,000/t, Mo: $20,000-40,000/t, Zn: $2,000-3,500/t during 2017-2022) [51-53]. However, in recent years, interest has been focused on the rising price of zinc. Zinc futures traded on the London Metal Exchange (LME) are above the $3,700/ton level. This is the highest price in about 15 years, since 2007. In addition, the rise in the non-ferrous metals market has been remarkable, and other inexpensive metals have also seen high prices across the board in recent years. This is due to expectations of increased demand as the world economy returns to normalcy after a period of stagnation caused by the new coronavirus infection and the uncertainty due to the war, as well as successive production cuts at smelters in response to power shortages in Europe and China [54]. However, despite these high price conditions, Zn still has a significant cost advantage.

The Zn secondaty battery is also expected to be provided at a low price when actually used as a battery. Canadian startup Zinc8 Energy Solutions (Zinc8) has attracted attention for its Zinc8 ESS, an energy storage system that uses zinc air battery technology [55]. This system can be operated at up to one-fifth the cost of Li-ion batteries. The capital cost for 8 hours of energy storage with the Zinc8 ESS is about $250/kWh, $100/kWh if the capacity is expanded to 32 hours, and $60/kWh for 100 hours. On the other hand, they estimate that a system using lithium-ion batteries would require more than two batteries to achieve a storage capacity of more than four hours, at a cost of about $300/kWh. In this Zinc8 ESS system, there is no net consumption of zinc, oxygen, or water during the operation of the battery, but the electrodes and power stack will degrade and need to be replaced every few years depending on usage. The energy efficiency of Zinc8 ESS (the percentage of energy ultimately output out of the input energy) is about 65%, which is not as high as the 95% of lithium-ion batteries, but considering the cost of energy storage, the use of Zinc8 ESS is considered highly valuable, and further development and simplification of Zn rechargeable batteries is important in the future Further development and simplification of Zn rechargeable batteries are important in the future.

1.2.2. Cost evaluation of Zn negative electrode secondary batteries

As described above, Zn negative electrodes are expected to eventually lead to the widespread use of rechargeable batteries with a Zn negative electrode. Secondary batteries using Zn negative electrode have many advantages over Li-ion batteries. The advantages include the low cost of the material and the safety of the aqueous solution system. In particular, the spread of rechargeable batteries for the large-scale energy storage that can be produced inexpensively is an urgent need in the future. The price of Zn itself is lower than that of Li oxide or materials such as Mo and Co used in Li-ion batteries, and Zn has advantages in terms of energy density. Hence, the material price of Zn negative electrode secondary batteries is estimated when it is used in a secondary battery cell. Therefore, based on previous estimates [56,57], the price is estimated by setting some conditions to examine the applicability of Zn negative electrodes and the energy density that should be aiming for. The assumptions are as follows [56]:

(i) The structure is the same cylindrical cell as the previous study
(ii) The costs other than electrode materials and electrolyte are the same as the previous study
(iii) The material prices of Zn battery are calculated by multiplying the price in the previous study and the ratio of the materials cost in the market
(iv) The specific energy density is the same as the previous study (200 Wh kg-battery^{-1})

Based on the above assumptions, the calculated results are shown in the table below.

Compared to the previously estimate material cost of the conventional Li-ion battery, the price of the Zn secondary battery is about half the price of the current Li-ion battery. In addition to this comparison, the promising batteries for the large-scale energy storage is evaluated by the previous study [58,59]. The redox flow battery using vanadium ion shows higher price of the electrolyte than that of the Zn secondary battery,

that is 35 Y/Wh. According to the brief estimation, sodium sulfur battery (NAS) can show the as half price as the redox flow battery. Although the detail estimation of the material price is required for the comparison, the Zn secondary battery can be effective for the large-scale energy storage. Since the result is based on the weight and electric energy of the batteries, the price varies depending on the capacity of the cathode and negative electrode and the price of the positive electrode. Therefore, it is aimed to provide a guideline for realistic battery design by changing the capacity of the negative and positive electrodes. The estimated prices are compared with other current Li ion batteries. The results are shown in Figure 1.3. Material price was calculated by the following equation (1.1) and (1.2).

Table 1.2. Price comparison of Zn and Li-ion secondary batteries.
* indicates this study. The specific energy density of the battery is assumed as 200 Wh $kg_{battery}^{-1}$

	Li-ion [56]	Prices (Y / Wh)	Zn battery*	Prices* (Y / Wh)
Positive electrode material	$LiCoO_2$	7.208	C6	2.448
Negative electrode material	C6	2.448	Zn	1.310
Electrolyte	EC + $LiPF_6$	1.36	6 M KOH aq.	0.0230
Others		0.952		0.952
Separator		1.632		1.632
Total		**13.6**		**6.365**

$$\begin{aligned}&\text{Material price}\\&= (\text{As calculated material price when 200 Wh})\\&\quad\times\frac{200\ \text{Wh}\ \text{kg}_{\text{battery}}^{-1}}{(\text{Calculated specific energy density})}\end{aligned}\tag{1.1}$$

$$\text{Calculated specific energy density} = \frac{V}{\frac{1}{q_{anode}}+\frac{1}{q_{cathode}}}\tag{1.2}$$

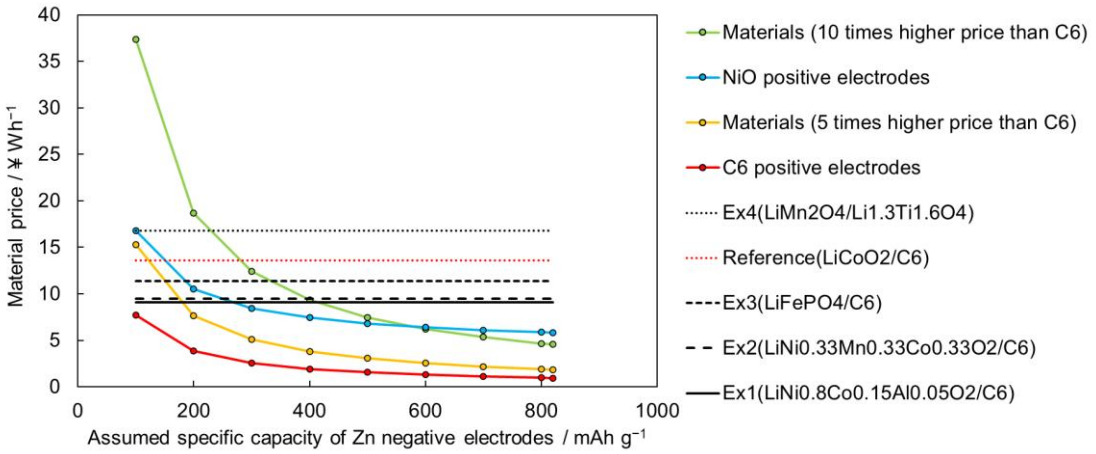

Figure 1.3. Estimation of material prices of the Zn secondary battery with respect to the specific capacity. Curves indicate the material prices of the Zn battery with the different positive electrode materials. Lateral straight lines indicate the price of the current Li-ion batteries.

The theoretical capacity of the Zn negative electrode is 820 mAh g^{-1} [60], which is the maximum value of the lateral axis. When the negative electrode is graphite (C6), the capacity is determined solely by the performance of the Zn negative electrode since an air secondary battery is assumed. The value of voltage also varies, but this is not considered in this study. Comparing the C6 positive electrodes, Materials (5 times higher price than C6) and Materials (10 times higher price than C6) curves with the price of conventional Li-ion batteries, it is expected that even if the positive electrode material is expensive, the Zn negative electrode that can produce a capacity of nearly 500 mAh g^{-1} will lead to a price in the 8 yen, which is lower than that of the current Li-ion battery. If the positive electrode is changed to a NiO-based material, the assumed voltage will also change [61]. In such a positive electrode, a battery with a capacity of around 400 mAh g^{-1} can be expected to reach the 8-yen range.

In practice, although it is considered that there will be deviation to some extent from the assumptions listed above due to the initial investment and operating costs involved in the manufacturing process, it is expected that the high safety of the Zn negative electrode means that safety management in large-scale storage batteries will become easier. The manufacturing process including the assembly of the moisture-sensitive components of the Li-ion battery such as the processes of electrolyte injection

is required for the manufacturing process of the Li-ion battery. The NAS battery is also considered to undergo the same process to avoid the condition including moisture, and the Zn secondary battery has an advantage in this respect. Although the long life of the NAS battery is an advantage [59], the high temperature required for its operation should be avoided if possible. The redox flow batteries have the advantage of being able to operate at room temperature, making it easy to control the state of charging and discharging. However, the excessive cost of vanadium and complex electrolyte systems are required for stationary use [58]. In the process of the Zn battery manufacturing, these processes are not required, and the safety is easily maintained in the process. Hence, it is expected to reduce the cost of maintaining safety and long-term cost.

The values used in these calculations are shown below.

Table 1.3. Price comparison of Zn and Li-ion secondary batteries

Cathode materials [56,57]	Prices (Y / Wh kg-battery^{-1})
Ex1($LiNi_{0.8}Co_{0.15}Al_{0.05}O_2$/C6)	9.1
Ex2($LiNi_{0.33}Mn_{0.33}Co_{0.33}O_2$/C6)	9.5
Ex3($LiFePO_4$/C6)	11.4
Ex4($LiMn_2O_4$/$Li_{1.3}Ti_{1.6}O_4$)	16.8
Reference($LiCoO_2$/C6)	13.6

Table 1.4. Theoretical capacity and voltage of the battery

Cathode materials	Theoretical capacity, $q_{cathode}$ / mAh g-1	Voltage (w/ Zn negative electrode) / V
NiOOH [61]	289	1.735
C6 (Air)	-	1.65

Table 1.5. Commercial prices of the materials

Materials	Mass / g	Price / Y	Price per weight / Y g^{-1}	References
Co_3O_4	500	18500	37	[62]
$CoSO_4$ $7H_2O$	500	37700	75.4	[63]
$Co(OH)_2$	250	31200	124.8	[64]
Li_2CO_3	500	12500	25	[65]
LiOH H_2O	500	5800	11.6	[66]
$CoCO_3$	500	64000	128	[67]
Ethylene Carbonate	500	7000	14	[68]
$LiPF_6$	50	10500	210	[69]
C6	500	4800	9.6	[70]
Zn	500	3700	7.4	[71]
KOH	5000	13000	2.6	[72]
$Ni(OH)_2$	500	13500	27	[73]

1.2.3. Problem for the application of the Zn negative electrode during charge process

Zn negative electrodes can be operated in various conditions electrolyte such as acid, mild, and alkaline. The alkaline Zn/MnO_2 battery using the KOH solution is an early and basic system of the Zn secondaty battery. Alkaline electrolytes using aqueous solutions with KOH or NaOH are mainly used to maintain the alkaline condition [74]. In this context, Zn/MnO_2 secondary batteries using a mild ZnSO4 electrolyte have been realized to show high cycle stability [75]. Furthermore, it was also proposed to use $ZnSO_4$ (zinc sulfate) or $Zn(NO_3)_2$ (zinc nitrate) as an electrolyte to intercalate Zn^{2+} into

MnO_2, thereby using it as a Zn-ion battery [74]. A zinc ion battery with a medium Co(III)-rich-Co_3O_4/Zn gel electrolyte was also reported, which delayed the damage and degradation of the separator during Zn-ion battery operation [76].

Figure 1.4. Schematic of a typical rechargeable Zn negative electrode (anode) battery [50]. *Republished with permission of Royal Society of Chemistry, from Challenges, Mitigation Strategies and Perspectives in Development of Zinc-electrode Materials/Fabrications for Rechargeable Zinc-air Batteries, J. Yi, 11, 2018; permission conveyed through Copyright Clearance Center, Inc.*

The study of Zn-based rechargeable batteries (ZBRBs) has become extensive because of its advatanges. Hence, the reaction mechanisms of Zn negative electrode secondaty batteries are gradually analyzed as a result of the many studies. Wang et al. summarized recent studies of solutions used in Zn rechargeable batteries [37]. The number of the research related to mild aqueous ZBRBs has been increasing, and new ZBRBs using acidic electrolyte environments are beginning to appear after 2019. This indicates that aqueous ZBRBs aree highly expected to apply in the real society. Although the energy density of aqueous zinc batteries cannot exceed that of the Li-ion battery, their power density has reached a level where they can be applied to supercapacitors [37]. In addition, the energy density of Zn secondary batteries with alkaline electrolyte is higher than that of Zn batteries with mild electrolytes. However, it is known the elementary processes on the surface of the Zn negative electrode reduce the battery capacity, and it is important to solve this problem. By solving the problems

of alkaline Zn negative electrode secondary batteries, further development of other Zn battery systems is expected to be featured as well. In the alkaline system, the redox potential is lower than in other solution systems and the hydrogen evolution reaction can be suppressed [77,78]. The energy density of the Zn system is higher, low-cost and simple, making it a useful system for large-scale storage batteries. The main reaction steps during charging in alkaline systems are known as follows [79].

$$H_2O + e^- \rightarrow H_{ad} + OH^- \quad (1.3)$$
$$Zn(OH)_4^{2-} \leftrightharpoons Zn(OH)_2 + 2OH^- \quad (1.4)$$
$$Zn(OH)_2 + e^- \rightarrow Zn(OH)_{ad} + OH^- \quad (1.5)$$
$$Zn(OH)_{ad} + H_{ad} \rightarrow Zn + H_2O \quad (1.6)$$
$$Zn(OH)_{ad} + e^- \rightarrow Zn + OH^- \quad (1.7)$$
$$Zn(OH)_4^{2-} \rightarrow ZnO + H_2O + 2OH^- \quad (1.8)$$

The discharge reaction is the backward direction of these equaitions which the precursor is oxidized. During the discharge reaction, the following chemical reaction occurs due to the change in zincate concentration near the surface, resulting in the deposition of ZnO [80,81]. This ZnO is formed by the super saturation of zincate ion near the surface due to the increase in the concentration of zincate near the surface following the discharge reaction proceeds to leach Zn and form zincate. Since ZnO is an insulator, its formation is thought to cover the Zn surface and prevent the charge-discharge reaction from progressing by the passivation [80].

In Zn systems with such reaction processes, the irregular shape evolution of Zn during the electrodeposition is one of the problems that Zn battery has faced. In particular, dendrites [82] and nanofilament-like structures called mossy structures [83-85] are formed as the irregular shape deposition, and these structures cause several problems [86-91]. One is that the growth of such irregular shapes can break through the separator between the negative and positive electrodes, causing a short circuit in the battery. In addition, the irregular shape of electrordeposited Zn such as dendrites and mossy structures on the negative electrode will be so-called “dead Zn” during the discharge process, which cannot desolve into the solution due to the loss of the electron pass, resulting in a decrease in charge-discharge efficiency. Previous studies have approached to this problem for the development of the efficient Zn battery. However,

the fundamental solution to control the morphology of Zn and suppress its irregular shape evolution has not been developed yet. Even the aforementioned Zinc8 does not prevent such irregular shape evolution to deposit, but rather removes the deposits formed on the electrode and reuses them as zinc particles for energy storage for the recycling operation of the battery. If this fundamental solution can be achieved, it will be possible to create a simpler Zn secondary battery system, which is expected to make a great leap forward as a large-scale storage battery.

The irregular shape evolution that appears during charging of Zn negative electrodes is characterized as dendrites and nano-filamentous structures called mossy structures, respectively [82-85]. Dendrites shows branch-like structures that grow sharply. This deposit is known to appear in the electrodeposition of many metals under the condition of high current densities and low concentrations. In contrast, the mossy structure is a nanofilamentary structure, as shown in Figure 1.5(a).

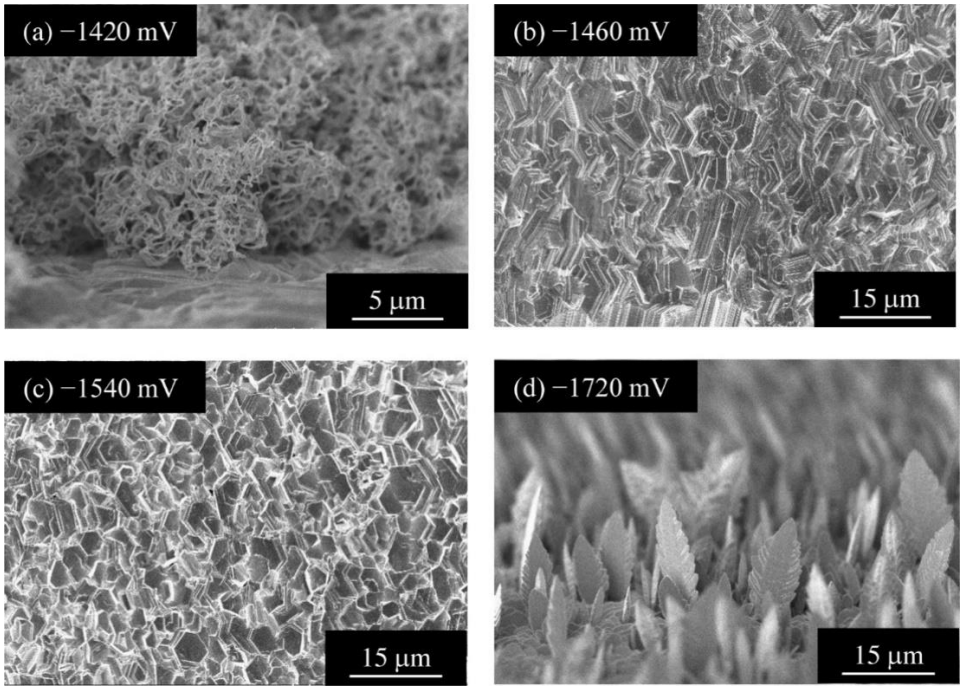

Figure 1.5. Zn deposits in the different applied potentials [83].

Reprinted from Morphological evolution of mossy structures during the electrodeposition of zinc from an alkaline zincate solution, 206, T. Otani et al., 366-373, Copyright (2016), with permission from Elsevier.

These mossy structures show the nano-filamentous strucutures, depositing in the conditions such as low current density, low overpotential, and high concentration environments. Figure 1.6 shows the low magnification of the mossy structures showing its moss-like strucrures. The mossy structures containing the nano-filamentous structures are not generally observed in metals other than Zn during the alkaline electrodeposition. As shown in Figure 1.5, previous studies have examined the conditions under which these irregular shape evolutions appear [83,92]. Since the deposition of such structures should be avoided, their mechanisms have been heat-debated. As for the dendritic growth which appears in many metals, its growth mechanism has been well studied. However, the mossy structures are unique to Zn, and its evolution mechanism is still in the investigation [93].

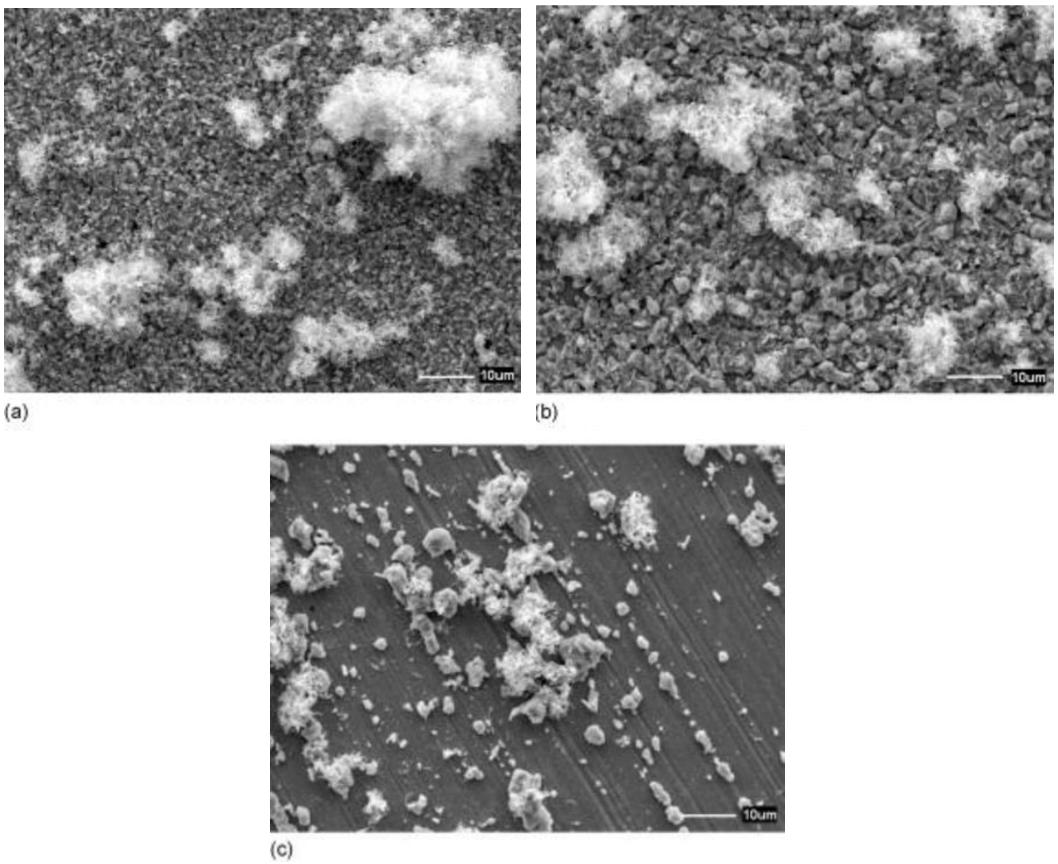

Figure 1.6. Mossy structures on different substrate on (a) Cu, (b) Ni, and (c) Fe [92]. *Used with permission of IOP Publishing, Ltd, from Effects of Deposition Conditions on the Morphology of Zinc Deposits from Alkaline Zincate Solutions, R. Y. Wang, D. W. Kirk, G. X. Zhang, 153; permission conveyed through Copyright Clearance Center, Inc.*

By the observation of the mossy structures in detail, the structures in Figure 1.7 are shown as a structure that seems to be in the process of its deposition. The protruding deposits in Figures 1.7(b)-(d) may be the structures at the initial stage of deposition, and the one in Figure 1.7(e) may be the beginning of these nano filaments. Furthermore, layered structures are observed under the all of the nanofilament structures. However, it is not clear at this point whether these protrustions can truly grow as nanofilaments.

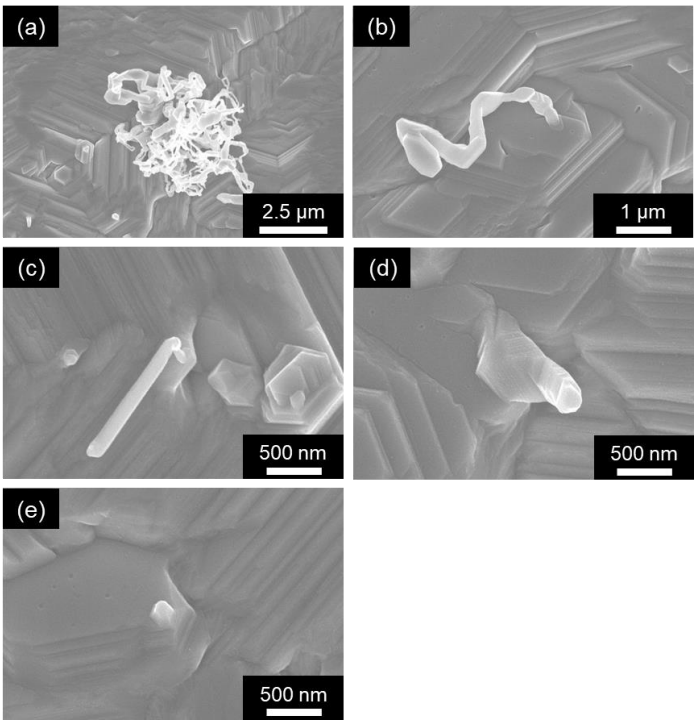

Figure 1.7. Electrodeposition structures of Zn: (a) nanofilaments, (b)-(d) nanofilaments in the short length, and (e) nanoscale protrusion.

As mentioned above, the mossy structures is composed of the nanofilamentous structures. The inside structure of the nanofilaments are previously analyzed [81]. This nanofilemnts are compsed of polycrystalline elongated to the [0001] direction, with branching and bending. Figure 1.8 shows a STEM image of the mossy structure in a previous study. It can be seen that the filament grows to the [0001] direction. It is thought that the grain boundary is formed during growth due to the instability of the tip.

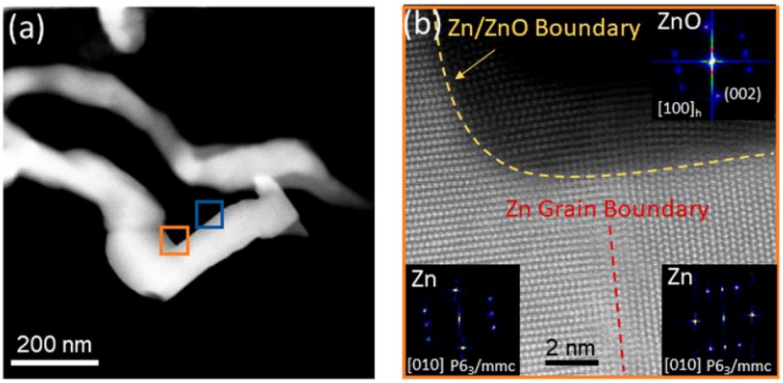

Figure 1.8. Zn deposits in the different applied potentials [81].
Reprinted with permission from The Mechanism of Zn Diffusion Through ZnO in Secondary Battery: A Combined Theoretical and Experimental Study, V. Yurkiv et al. J. Phys. Chem. C 124 15730-15738. Copyright 2020 American Chemical Society.

1.2.4. Analysis and hypothesis related to the growth of the mossy structures

The Zn deposition structures are analyzed during the growth of the mossy structures. Figure 1.9 shows the results of an *in-situ* optical microscope observation of filament elongation in a previous study [83]. Following the white square in Figure 1.9 from left to right, it can be seen that there is no significant change from 120 to 840 seconds. This indicates that no electrodeposition occurs outside of the mossy structure during the growth of the mossy structure. It may be considered that preferential deposition occur especially around the mossy structures.

Based on the above results, the following growth mechanism of the mossy structure can be hypothesized with the condition of the low overpotential. First, layer-by-layer structure of the (0001) facets are deposited on the surface as shown in stage (i). After the layer-by-layer structures deposit for a while, a protrusion appears on top of it. Once these protrusions appear, it is thought that growth does not occur in other areas according to the *in-situ* observation, so that only these protrusions continue to grow. The protrusion then become nanofilaments, which eventually form the mossy structure. The mechanism of the deposition of the protrusion in particular has been mentioned in a

previous study [84]. The mechanism of the elongation of protrusions in the similar system has been reported such as the screw dislocations which is caused by the dislocation of the atoms of the surface and the impurity-induced catalysis at the tips of the protrusions. The screw dislocations have often been observed in ZnO growth [94], and an impurity mechanism has been proposed as one of the mechanisms of the growth of Zn-Ni alloys [95].

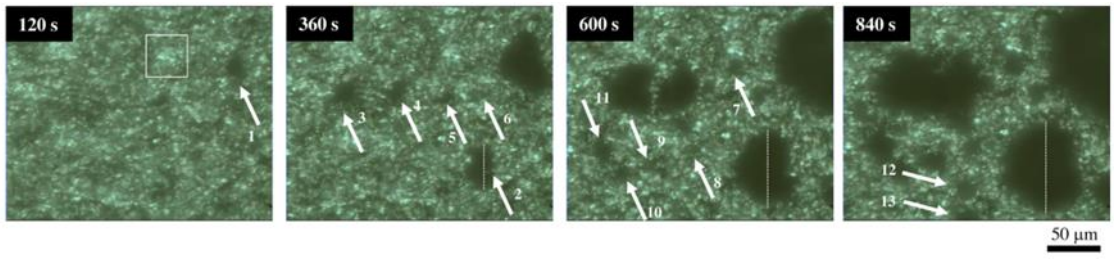

Figure 1.9. *In-situ* optical microscope observation during the mossy evolution [83]. *Reprinted from Morphological evolution of mossy structures during the electrodeposition of zinc from an alkaline zincate solution, 206, T. Otani et al., 366-373, Copyright (2016), with permission from Elsevier.*

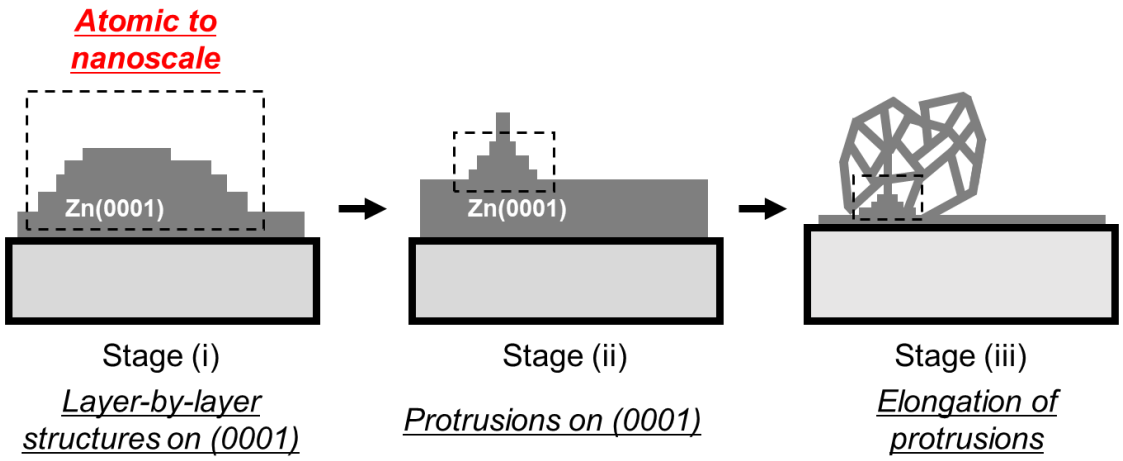

Figure 1.10. Hypothesis of the growth mechanism of the mossy structure. Dashed squares show the same scale in the different growth stage.

However, It is unclear why the layer-by-layer structures appear at the initial stage of the Zn electrodeposition. In addition, the mechanisms of the protrusion and its

elongation are not known well. Without understanding the growth mechanism of the initial structures, it would be difficult to examine how stages (ii) and (iii) could proceed. In other words, clarifying first why this layer-by-layer structure deposits is important for further analysis of the growth mechanism of the mossy structure. The deposition of the layer-by-layer structures is considered to be related to the behavior of the atoms on the surface because it is in the early stage of the deposition. Providing atomic-level knowledge of this deposition phenomena may be helpful toward understanding the growth mechanism. As for stages (ii) and (iii), the appearance of the active sites such as screw dislocations and points with impurity catalysts can also be atomic-level phenomena. Hence, understanding at the atomic level is important in such a deposition phenomena. However, these phenomena are not easy to analyze such deposition phenomena by conventional experimental methods, as will be shown in the next section.

1.2.5. Atomic behavior on metal negative electrodes during charge process

As mentioned above, the mechanism of the shape evolution at the initial stage of the electrodeposition process should be understood because the deposition structure at the initial stage can provide information of the cause of the initiation of the shape evolution. In general, the deposition step in electrodeposition proceeds with the several steps in the atomic level. The reaction precursors approach at the surface, react, deposit, diffuse on the surface, and crystallize [96,97]. The detail is explained as follows.

Figure 1.11 shows the steps in the electrodeposition until the main deposits appear on the surface. During the deposition process, electrons are transferred to reaction precursors and a reaction occurs as the first step at the atomic level phenomena to obtain the main deposit shown as (a) in Figure 1.11. This step determines the deposition potential in the proecss. Furthermore, the deposited atoms diffuse on the surface shown as (b-i) in Figure 1.11. Through such a surface diffusion of adsorbed atoms, they aggregate with other atoms and crystallize as shown in (b-ii). The deposited atoms are also adsorbed on the deposited crystals and surface diffusion proceeds on the surface which consists of the deposited atoms. In the type of surface diffusion, the step-edge diffusion, which is the migration from the upper step to the lower edge of the deposited terraces, is known as the most characteristic diffusion in surface diffusion shown in (b-

iii), and its activation energy is called the Ehrlich-Schwoebel (ES) barrier [98,99]. Since the electrodeposits are formed through these steps, it is important to consider the role of each step in order to study how the morphology is shaped.

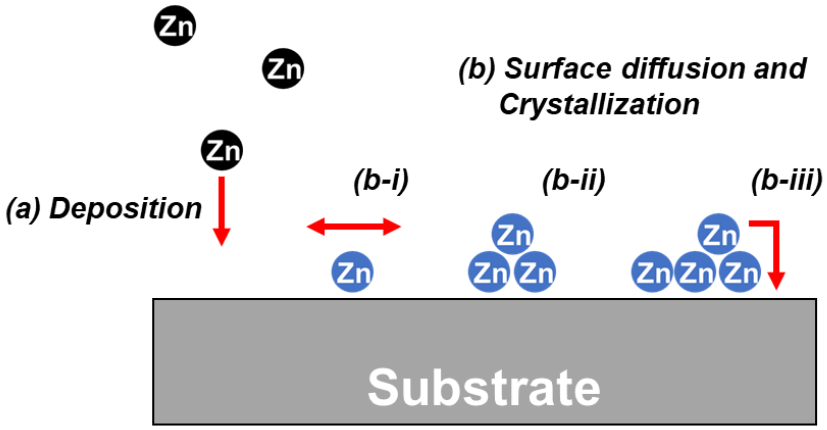

Figure 1.11. Representative steps of the deposition from atomic scale during the electrodeposition. Black balls indicate Zn precursor. Blue balls indicate Zn adatom on the surface.

1.2.6. Suppression of the irregular shape evolution by additives

To control the shape evolution of the electrodeposited Zn on the surface morphology through the above steps, the approach used commonly is the use of additives. In particular, since Zn is an important material not only in batteries but also in surface treatment processes, studies have been performed to enhance such smoothness. The comparison of additive effects indicates that the smoothing effects can be in the order of citric acid > succinic acid > tartaric acid > phosphoric acid [100]. In addition, a comparison of the effectiveness of benzylideneacetone, benzylacetone, and butylbenzene have been studied as brightners [101], which are compounds containing aromatic rings. The various types of organic additives have been reported: trisodium nitrilotriacetic [102], oxalate anion [103], sorbitol [104], Tween20 [105], and the polymeric Polyethyleneimine [106-108], polyethylene oxide [109], polyethylene glycol [110], and polyacrylic acid [111]. Furthermore, the use of cationic polymers [112], ionic liquids [113,114], anionic sodium dodecyl sulfate (SDS), neutral Triton X-100, and cationic cetyltrimethlammonium bromide (CTAB) [111,115,116], and others have

considered as ionic additives. Other studies have also suggested the use of ionic additives [117] and the usefulness of cationic additives such as tetrabutylammonium sulfate [118] and 1-Ethyl-1-methyl pyrrolidinium bromide [119] in addition to STAC [111].

Because of the effect of these particularly cationic additives, alkali metal ions have also attracted attention to control the morphology. It is suggested that several molecular additives exhibit synergistic effects with Na^+, and that the presence of Na^+ leads to stronger adsorption on the electrode [120]. The other study reported that Li^+ improves the discharge capacity of Zn-air batteries in the presence of K^+ [121]. In addition to the synnergystic effects, an effect of the Li^+ addition was also reported that test cell including LiCl into the electrolyte showed better stability in long-cycle tests [122]. For the discharge process, Li^+ has also shown the effect, reducing the deposition of ZnO during discharge. This efffect results in a smooth deposition [123]. Li^+, which has the largest charge density among alkali cations, is considered to interact with surface species at the outermost Helmholtz plane [124], which is an interesting distinction from other types of additives that act as adsorbed species. Hence, understanding such effects of Li^+ at the molecular level will provide valuable insight for electrolyte design.

In addition to the alkali metals, the use of the other metal additives such as Sn, Bi, and Pb, which show the more positive deposition potential than Zn, has been investigated to suppress both dendrite and mossy structures. Fe and In are also known to be effective on the surface [125-128]. The additives such as Sn [84,87,129,130] and Bi [131-133] have been suggested to be effective on surfaces. In particular, it is indicated that Pb addition gives a characteristic nano-level Zn deposition structure at low current densities [84,134,135], but the deposition behavior of Zn and Pb responsible for this effect are not clear. Analysis of the mechanism of this effect of Pb, which can suppress the deposition of the irregular shape evolution at both high and low current densities, could provide important insight into the development of additive species that exert their effects at the surface. Previous studies have suggested that Pb does not affect the charge transfer process of Zn deposition [136], and the behavior of deposited Zn atoms after the charge transfer process is considered to be important.

However, even though the additive effects should be understood at molecular level, it is difficult to investigate the deposition behavior of the main deposits in electrodeposition with such additives at the nano-level, and the mechanism can be analyzed not only by electrochemical measurements but also by the complementary use of other techniques. For the analysis of these additive working near the surface in the solution such as the alkali metals and adsorbing or depositing with the main deposits,

the analysis should include the precise modelling of the solid-liquid interface during the electrodepostion. In addition, once the phenomena during the electrodeposition is visualized at the molecular level, understanding for the electrodeposition process on the surface will be deepen. It can provide valuable insight into the further development of the effective additives for the Zn negative electrode secondary battery.

1.3. Simulation methods of the phenomena at the electrochemical interfaces

1.3.1. First-principles calculations to reproduce the electrochemical interfaces

During electrodeposition, the analysis of the elementary processes at the atomic and molecular level is difficult at solid-liquid interfaces where electrons are transferred using only experimental methods. In such cases, simulations, which have already been widely used, are useful. Especially for understanding elementary processes at the atomic and molecular level, the density functional theory (DFT) has been widely used among first-principles calculations. The basis of DFT is based on two mathematical theorems proved by Kohn and Hohenberg and a set of equations introduced by Kohn and Sham. DFT is a method of obtaining solutions by modifying the Schrodinger equation to include only one electron and determining the electron density.

For the use of DFT for systems with surfaces, such as solid-liquid interfaces, the plane-wave basis is more effective than the localized basis which considers electrons only in the vicinity of atoms in the model. When the plane-wave basis set is used, a model called a supercell are constructed as waves for one period for the consideration of electrons. Some computational packages are available for such calculations, including Quantum ESPRESSO [137,138], VASP [139,140,141], and SIESTA [142]. In DFT calculations based on the first-principles calculations using the plane-wave basis described above, when the x-, y-, and z-axies are defined as $\mathbf{a}_1$, $\mathbf{a}_2$, and $\mathbf{a}_3$ for the supercell, repectively, the solution, $\Phi_{\mathbf{k}}(\mathbf{r})$, must be expressed as follows [143].

$$\Phi_{\mathbf{k}}(\mathbf{r}) = \exp(i\mathbf{k}\cdot\mathbf{r})u_{\mathbf{k}}(\mathbf{r}) \quad (1.9)$$

$$u_{\mathbf{k}}(\mathbf{r}) = u_{\mathbf{k}}(\mathbf{r} + n_1\mathbf{a}_1 + n_2\mathbf{a}_2 + n_3\mathbf{a}_3) \quad (1.10)$$

In this case, n_1, n_2, and n_3 are arbitrary integers. In other words, $u_{\mathbf{k}}(\mathbf{r})$ is a periodic function with the same period as the supercell. This theorem allows us to solve the Schrodinger equation by obtaining the Kohn-Sham equation as a functional of the electron density. The vector **k** is a vector in the reciprocal space and is called the reciprocal lattice vector. This vector in the reciprocal spaece correpponds to the lattice vector **r** (= ($\mathbf{a}_1$, $\mathbf{a}_2$, $\mathbf{a}_3$)) in real space. Since exp ($i\mathbf{k}\cdot\mathbf{r}$) is called a plane wave, the calculation of such a periodic system is called “computation using a plane wave basis”. By solving these equations, it is possible to calculate the energy and density of states of the system [143].

In first-principles calculations, surfaces are generally modeled using a slab model, in which a certain surface of a solid is cut out and a sufficient vacuum layer is inserted between the slabs. The model has a repeating structure of several layers of atoms, a vacuum layer, several layers of atoms, a vacuum layer, and so on. By inserting a vacuum layer, the model does not take into account the interaction between each atomic layer in the neighbor supercell, and it is possible to analyze elementary processes on the surface.

As for the first-principles calculations of electrochemical systems such as electrodeposition, it is important to model the solid-liquid interface, or electrochemical interface, at which electrons are transferred. The modelling methods of the sovent effect are important at the electrochemical interface. Previous study has proposed two major types of solvent modeling methods: explicit solvent modeling and implicit solvent modeling. In the explicit model, water molecules are literally placed as they are, and their electronic states and interactions can be explicitly considered [144-146]. On the other hand, the computational cost increases with respect to the increase of the number of electrons in the solvent species. For the optimization of the orientation of the solvent species, a procedure such as molecular dynamics to determine an appropriate initial configuration, followed by DFT calculations, can be effective. In the implicit method, the solvent effect is taken into account by approximately placing the solvent around the

model for the DFT calculation. The polarized continuum model [147], which sets the dielectric to incorporate polarization that can be assumed to be provided by the solvent molecules, is known as the main method. However, not only in these methods, but also in other widely used methods, it has been difficult to account for applied potential at the electrochemical interface.

Recently, effective screening medium (ESM)-reference interaction site model (RISM) has recently been developed to simulate the electrochemical interface with the consideration of the applied potential assuming the desired reference electrodes [148-150]. Here, a force field model is used in which the solvent molecule is approximated by a set of several point charges. This treatment allows us to analyze the distribution of the electrolyte species. In addition, the potential of the metal slab with respect to the reference electrode can be considered by defining the potential of the reference electrode in solution based on the difference in their free energies, whereas previously only the difference in potential in vacuum could be considered. The periodic boundary condition in the vertical direction of the slab is removed in order to establish a potential criterion, and the supercell is completely expanded to only two dimensions. This corresponds to the Laue-RISM calculation [148]. As shown in Figure 1.12, Nishihara et al. used a slab model of the Al(111) surface to reproduce its solid-liquid interface [148]. It can be observed that the solvent distribution in the vicinity is obtained with respect to the electrolyte species and the change of the applied potential. In this way, it is possible to reproduce the electrochemical interface even in the first-priciples calulations. Hence, among the methods to model the solid-liquid interface, ESM-RISM is expected to be particularly useful because it can even take the applied potential with respect to the reference electrode into account.

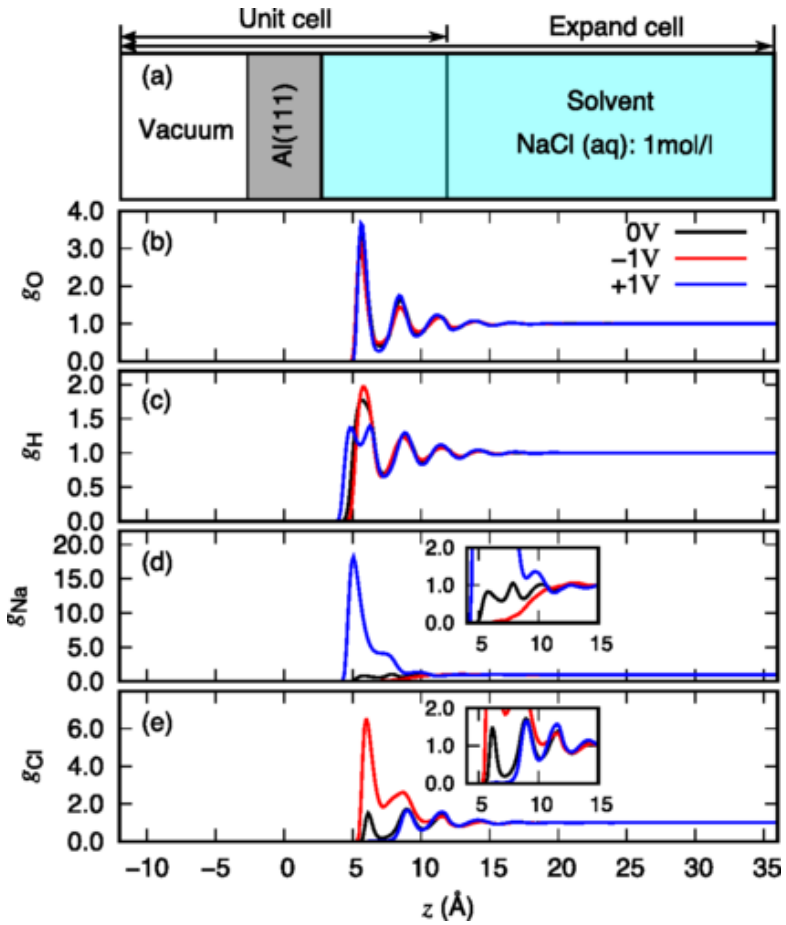

Figure 1.12. (a) Geometric configuration of the solid/liquid interface (vacuum/slab/solvent model). Normalized distribution function for (b) O, (c) H, (d) Na, and (e) Cl with different bias potentials. The Fermi energies of the systems are –5.3, –4.3, and –3.3 eV for –1.0, 0.0, and +1.0 V vs. pzc, respectively [148].

1.3.2. Nanoscale simulations of the shape evolution for electrodeposition processes

The electrodeposition processes corresponding to the charge processes in battery operation are a complex and simultaneous process of phenomena at several different scales. As mentioned in the previous section, on the surface, electrodeposits are deposited through the formation of adatoms, surface diffusion of adatoms, and crystallization at the atomic scale. On the solution side, mass transfer to the surface, convection, and the effect of electrical double layer should be cared. It is difficult to

deal with these phenomena completely in a single simulation. Therefore, the combination of the simulaions have been attempted to analyze these phenomena at different scales using various simulations. At the atomic and molecular level, first-principles calculations and molecular dynamics methods have been used as described above. For phenomena related to surface morphology at the nano- and micro-level, the phase field method and the kinetic Monte Carlo (KMC) method are often used [151-157].The phase field method expresses the presence or absence of a deposit at a certain location by probability, which is determined for each grid defined in the simulation. This procedure make it possible to examine the morphology of the deposit by the distribution of the grid. While this method has the advantage for handling somewhat large systems, it is unable to capture phenomena that accumulate at the atomic and molecular level.

In contrast, KMC can be applied for the observation of shape evolution by accumulating the movements of individual atoms. This method is capable of correlating the occurrence of phenomena with its time evolution by taking the sum of the rates of all phenomena in a certain state and treating them as stochastic processes corresponding to the rates of the respective phenomena. In KMC, it is assumed that the events follow a Poisson process (the number of events occurring at a given time t, $X(t)$, where $X(0) = 0$, the number of events occurring in non-overlapping time regions are independent of each other, and the number of events occurring in the time region $t_2 - t_1$ follows Equation (1.9)) [158].

$$\mathrm{Prob}\{X(t_2) - X(t_1))\} = \frac{[\lambda(t_2 - t_1)]^n}{n!} \mathrm{e}^{-\lambda(t_2 - t_1)} \ (n = 0, 1, 2 \ldots) \quad (1.11)$$

Prob is the probability density function of an event occurring. Equation (1.9) expresses the probability that an event can occur n times in $t_2 - t_1$. λ is the average number of events occuring per unit of time. In such a situation, assuming a very short time period Δt (= t/n (when $n \to \infty$)), where an event can occur only once within that Δt, and further assuming that each event is independent, the following equation is obtained.

$$\mathrm{Prob}\{X(t)=k\}=\frac{(\lambda t)^k}{k!}\mathrm{e}^{-\lambda t}\qquad(k=0,1,2\ldots) \tag{1.12}$$

In this case, λ is the average number of events per unit time, and the unit is [time^{-1}]. It is considered that a certain time interval Δt when an event occurs according to Poisson's density function. First, the probability that the first event does not occur is shown in the equation (1.11). T_1 is the time when the first event occurs, the events that occur during $T_1 > t$ (= no event occurs) and the event indicated by $X(t)=0$ (= no event occurs in time) are identical events.

$$\mathrm{Prob}\{T_1>t\}=\mathrm{Prob}\{X(t)=0\}=\frac{(\lambda t)^0}{0!}e^{-\lambda t}=e^{-\lambda t} \tag{1.13}$$

Furthermore, in this process, the occurrence of an event at a certain time t and $t + \Delta t$ is considered. If no event occurs during Δt, then this Δt can be regarded as the time progress between events. The following equation is derived by considering the probability density with reference to the above equation (1.11).

$$\mathrm{Prob}\{X(t+\Delta t)-X(t)=0\}=\mathrm{Prob}\{T_1>\Delta t\}=e^{-\lambda\Delta t} \tag{1.14}$$

In such a case, if the probability density on the left-hand side is the random number u∈[0,1), Δt can be expressed by the following equation.

$$\Delta t=-\frac{\ln(u)}{\lambda} \tag{1.15}$$

In this way, it is possible to perform the KMC method, which is a time evolution. In particular, since λ represents the number of events occurring per unit time in a given situation, it is determined by considering the sum of the rates of all possible events in a given situation. For example, if, in a given situation of electrodeposition, deposition occurs at a rate r_1, surface diffusion at r_2, and another surface diffusion at r_3 (unit for all of them is in s^{-1}), and these are all possible events in a given situation, λ can be

expressed as follows.

$$\lambda = r_1 + r_2 + r_3 \tag{1.16}$$

In order to calculate the rate for the Poisson process, rates corresponding to the behavior of each atom should be defined, which allows us to visualize how the shape evolution proceeds from the movement of each atom with the time progress. In particular, a certain movement, i, of each atom can be expressed by the following Arrhenius equation using the activation energy, $E_{\mathrm{a},i}$.

$$r_i = A\exp(\frac{-E_{\mathrm{a},i}}{\mathrm{R}T}) \tag{1.17}$$

Where A is the frequency factor, R is the gas constant, and T is the temperature. i refers to an event, r_i is the rate of an event, and $E_{a,i}$ is the activation energy of an event i. Hence, the KMC method can be scaled up from the atomic level to the nano-level by combining it with atomic-level calculations such as first-principles calculations.

For the analysis of the electrodeposition, simulations using the KMC method have been performed in previous studies. Here, the initial precipitation mechanism of Cu has been analyzed [154] and electrodeposition fulfilling inside a trench have been simulated [155]. In addition, KMC simulations for dendrite analysis in Li negative electrode have also been performed [157], providing knowledge at the atomic level. Hence, it is expected that such simulations can be further extended by giving physical meaning to the parameters used themselves. In particular, it is expected that the combination with advanced first-principles calculations such as DFT with ESM-RISM will make it possible to model the movement of atoms with information of the electronic state and the electrochemical interface and even to simulate crystal growth during the electrodeposition.

1.4. Aim of this dissertation

1.4.1. Multiscale simulation of the shape evolution of Zn from atomic to nano scales at the initial stage of the deposition

An atomic-level understanding is required to provide clues to explain the mechanism hypothesized above in order to suppress the irregular shape evolution, which shuold be overcome for the application of the Zn negative electrode in secondary batteries. In particular, the layer-by-layer structures are considered to appear as the atomic-level deposition as shown in stage (i). The analysis of the growth of the layer-by-layer structures at the atomic level can be expected to provide useful information for the verification of stages (ii) and (iii). However, since the layer-by-layer structures appear in the early stage of electrodeposition, the analysis for its evolution is difficult only by conventional electrochemical methods. Therefore, in this dissertation, a multiscale simulation to analyze the deposition mechanism from the atomic and molecular level to nanoscale is constructed to model the Zn deposition and elucidate the origin of the layer-by-layer structures which is observed under the mossy structures. The multiscale simulation here is a complementary combination of first-principles calculations for atomic- and molecular-level analysis and the KMC method, which extends the atomic-level motion to the nano-level. Such a combination of first-principles calculations and KMC has been used for solid-phase diffusion [153], but not for electrodeposition. In first-principles calculations, the ESM-RISM method is used to reproduce the solid-liquid interface. In KMC, the parameters themselves are inherently meaningless, which hence first-principles calculations can be used to assign meaning to the parameters. The activation energy calculated from first-principles calculations is introduced into the KMC method as the parameter, resulting in a multiscale simulation. This method allows us to focus on nano-level phenomena that are difficult to analyze using first-principles calculations alone. In addition, the the ESM-RISM method can give information of the solid-liquid interface to the parameters of the KMC simulations.

In Chapter 2, this multi-scale simulation with DFT and KMC are constructed to

analyze the surface diffusion behavior of deposited Zn atoms by first-principles calculations at the condition of the low current density, and then analyze the evolution mechanism of the layer-by-layer structures of Zn from a series of atomic-level phenomena by introducing the activation energy of the surface diffusions into KMC. The origin of the layer-by-layer structures are discussed from the atomic level to nanometer level. This clarifies how the layer-by-layer structures is caused by the behavior of deposited Zn atoms. In addition, the possible hypotheses of the mechanism of stages (ii) and (iii) will be discussed at the atomic scale based on the obtained simulation results of the layer-by-layer structure growth. In Chapter 3, the origin of the specific behavior of the deposited Zn atom from the electronic structure based on the results of first-principles calculations. In particular, the interaction between the deposited Zn atoms and the surface is discussed by analyzing the electronic state of them.

1.4.2. Effective combination of simulations and experimental analyses for the Zn atomic behavior with additives at electrochemical interfaces

By analyzing the factors of the deposition mechanism at the atomic scale, it is expected that the effective strategy can be obtained for the development of the bath condition during the electrodeposition with respect to the atomic viewpoint. From that viewpoint, the additives that exhibit an important influence on the shape evolution are focused on and investigated to clarify the mechanism of its effect and the behavior of deposited Zn atoms in the presence of the additives. In particular, the effect of the additives are analyzed effectively using the simulations described above to analyze these effects. Two types of the additives are focused on: one dissolved in the solution and the other deposited on the surface which deposits earlier than Zn. In addition, to compare the results with the combination of the experimental aspects, the conventional electrochemical methods shuold be also utilized.

In Chapter 4, the effect of the Li^+ addition which is expected to be effective from

solution at the solid-liquid interface is focused on. As mentioned above, Li^+ is expected to exhibit its effect from solution as an alkali metal. Since the KMC simulations based on activation energies obtained by DFT with ESM-RISM can involve the information of the electrolyte distribution near the surface, it is expected to elucidate the effect of Li^+ near the surface. In Chapter 5, the effect of Pb addition is analyzed. Unlike Li^+, Pb addition is suggested to deposit earlier than Zn deposition due to its positive deposition potential than Zn, which hence a different mechanism is expected. In order to analyze the mechanism of the additive effect on the surface or in the deposited film, the experimental measurements and DFT calculations analyze the behavior of the deposited Zn atoms behave on the surface. These analyses give general knowledge on how various additives behave in the vicinity of the surface to show their effects on the electrodeposition. This research for the Zn negative electrode secondary battery will provide valuable insight for its application. Hence, the contribution of this research to the application of large-scale energy storages for social implementation is discussed at the end of Chapter 5.

.

References

[1] United Nations, Resolution adopted by the General Assembly on 6 July 2017.

[2] Ministry of the Environment, https://www.env.go.jp/press/files/jp/115174.pdf, (Accessed on May 23rd, 2022).

[3] New Energy and Industrial Technology Development Organization, https://www.nedo.go.jp/content/100544816.pdf , (Accessed on May 23rd, 2022).

[4] O. Edenhofer, R. P. Madruga, Y. Sokona, Renewable Energy Sources and Climate Change Mitigation Special Report of the Intergovernmental Panel on Climate Change, *Cambridge University Press*, 1st Edition, (2012).

[5] Institute for Sustanable Energy Policies, https://www.isep.or.jp/archives/library/13427, (2021) (Accessed on February 2nd, 2022).

[6] Y. Tsujii, T. Tsuji, T. Oyama, Y. Nakachi, S. Chand Verma, A Study on the Frequency in Case of High Prenetration of Renewable Enegy Sources, *IEEJ Trans.* 136 (2015) 33-45.

[7] S. Arif, T. Aziz, Impact of Battery Energy Storage System on Post-Fault Frequency Fluctuation in Renewable Integrated Microgrid, *ECCE 2017*, Cox's Bazar, Bangladesh, (2017) 594-598.

[8] Y. Sun, Z. Zhao, M. Yang, D. Jia, W. Pei, B. Xu, Overview of Energy Storage in Renewable Energy Power Fluctuation Mitigation, *CSEE J. Power Energy Syst.* 6 (2020) 160-173.

[9] Q. Lei, Y. Si, Y. Liu, Energy Storage System Control Strategy to Minimize the Voltage and Frequency Flucutuation in the Microgird, *2018 IEEE Applied Power Electronics Conference and Exposition (APEC)* (2018) 1500-1505.

[10] A. Z. AL Shaqsi, K. Sopian, A. Al-Hinai, Review of Energy Storage Services, Applications, Limitations, and Benefits, *Energy Rep.* 6 (2020) 288-306.

[11] M. Short, S. Rodriguez, R. Charlesworth, T. Crosbie, N. Dawood, Optimal Dispatch of Aggregated HVAC Units for Demand Response: An Industry 4.0 Approach, *Energies* 12(22) (2019) 4320.

[12] I. Hussain, S. Mohsin, A. Basit, Z. A. Khan, U. Qasim, N. Javaid, A Review on Demand Response: Pricing,Optimization, and Appliance Scheduling, *Procedia Comput. Sci.* 52 (2015) 843-850.

[13] F. Shariatzadeh, P. Mandal, A. K. Srivastava, Demand Response for Sustainable Energy Systems: A Review, Application and Implementation Strategy, R*enew. Sust. Energ. Rev.* 45 (2015) 343-350.

[14] Federal Energy Regulatory Commission, Assessment of Demand Response and Advanced Metering. In: Staff Report, (2012).

[15] E. Mashhour, S. M. Moghaddas-Tafreshi, Bidding Strategy of Virtual Power Plant for Participating in Energy and Spinning Reserve Markets—Part I: Problem Formulation, *IEEE Trans. Power Syst.* 26 (2011) 949-956.

[16] J. Rodríguez-García, D. Ribó-Pérez, C. Álvarez-Bel, E. Peñalvo-López, Novel Conceptual Architecture for the Next-Generation Electricity Markets to Enhance a Large Penetration of Renewable Energy, *Energies* 12 (2019) 2605.

[17] H. M. Rouzbahani, H. Karimipour, L. Lei, A Review on Virtual Power Plant for Energy Management, *Sustain. Energy Technol. Assess.* 47 (2021) 101370.

[18] N. Naval, J. M. Yusta, Virtual Power Plant Models and Electricity Markets - A Review, *Renew. Sustain. Energy Rev.* 149 (2021) 111393.

[19] S. Ghavidel, L. Li, J. Aghaei, T. Yu, J. Zhu, A Review on the Virtual Power Plant: Components and Operation Systems, *2016 IEEE International Conference on Power System Technology (POWERCON)* (2016) 1-6.

[20] X. Wang, Z. Liu, H. Zhang, Y. Zhao, J. Shi, H. Ding, A Review on Virtual Power Plant Concept, Application and Challenges, *2019 IEEE PES Innov.* (2019) 4328-4333.

[21] E. Bullich-Massagué, F.-J. Cifuentes-García, I. Glenny-Crende, M. Cheah-Mañé, M. Aragüés-Peñalba, F. Díaz-González, O. Gomis-Bellmunt, A Review of Energy Storage Technologies for Large Scale Photovoltaic Power Plants, *Appl. Energy* 274 (2020) 115213.

[22] S. Hammer, J. L. Van Niekerk, A Review of Large-scale Electrical Energy Storage, *Int. J. Energy Res.* 39 (2015) 1179-1195.

[23] T. M. Gür, Review of Electrical Energy Storage Technologies, Materials and Systems: Challenges and Prospects for Large-scale Grid Storage, *Energy Environ. Sci.* 11 (2018) 2696-2767.

[24] Mitsubishi Research Institute, Inc.,
https://www.meti.go.jp/shingikai/energy_environment/storage_system/pdf/001_05_00.p

df, (Accessed on May 23rd, 2022).

[25] V. Etacheri, R. Marom, R. Elazari, G. Salitra, D. Aurbach, Challenges in the Development of Advanced Li-ion Batteries: A Review, *Energy Environ. Sci.* 4 (2011) 3243-3262.

[26] J. Yi, Y. Liu, Y. Qiao, P. He, H. Zhou, Boosting the Cycle Life of Li−O_2 Batteries at Elevated Temperature by Employing a Hybrid Polymer−Ceramic Solid Electrolyte, *ACS Energy Lett.*, 2 (2017) 1378-1384.

[27] S. Liu, L. Zhao, B. Cui, X. Liu, W. Han, J. Zhang, W. Xiang, A Long Life and High Efficient Rechargeable Hybrid Zinc-air/Co_3O_4 Battery with Stable High Working Voltage, *Ionics*, 26 (2020) 767-775.

[28] M. A. Rahman, X. Wang, C. Wen, High Enegy Density Metal-Air Batteries: A Review, *J. Electrochem. Soc.* 160 (2013) A1759-1771.

[29] N. Niita, F. Wu, J. T. Lee, G. Yushin, Li-ion Battery Materials: Present and Future, *Mater. Today*, 18 (2015) 252-264.

[30] K. Amini, M. D. Pritzker, Electrodeposition and Electrodissolution of Zinc in Mixed Methanesulfonate-based Electrolytes, *Electrochim. Acta*, 268 (2018) 448-461.

[31] I. Aramendia, U. Fernandez-Gamiz, A. Martinez-San-Vicente, E. Zulueta, J. M. Lopez-Guede, Vanadium Redox Flow Batteries: A Review Oriented to Fluid-Dynamic Optimization, *Energies* 14 (2021) 176.

[32] S. Peng, N.-F. Wang, X.-J. Wu, S.-Q. Liu, D. Fang, Y.-N. Liu, K.-L. Huang, Vanadium Species in CH_3SO_3H and H_2SO_4 Mixed Acid as the Supporting Electrolyte for Vanadium Redox Flow Battery, *Int. J. Elctrochem. Sci.* 7 (2012) 643-649.

[33] S. Kim, E. Thomsen, G. Xia, Z. Nie, J. Bao, K. Recknagle, W. Wang, V. Viswanathan, Q. Luo, X. Wei et al., 1 kW/1 kWh Advanced Vanadium Redox Flow Battery Utilizing Mixed Acid Electrolytes, *J. Power Sources* 237 (2013) 300-309.

[34] S. Kim, M. Vijayakumar, W. Wang, J. Zhang, B. Chen, Z. Nie, F. Chen, J. Hu, L. Li, Z. Yang, Chloride Supporting Electrolytes for All-vanadium Redox Flow Batteries, *Phys. Chem. Phys. Chem.* 13 (2011) 18186-18193.

[35] NGK INSULATORS, LTD., PRODUCTS about NAS Batteries, https://www.ngk-insulators.com/en/product/nas.html, (Accessed on February 2nd, 2022).

[36] G. J. May, A. Davidsonb, B. Monahovc, Lead Batteries for Utility Energy Storage:

A Review, *J. Energy Storage* 15 (2018) 145-157.

[37] N. Wang, H. Wan, J. Duan, X. Wang, L. Tao, J. Zhang, H. Wang, A Review of Zinc-based Battery from Alkaline to Acid, *Mater. Today Adv.* 11 (2021) 100149.

[38] V. P. H. Huy, L. Trung Hieu, J. Hur, Zn Metal Anodes for Zn-Ion Batteries in Mild Aqueous Electrolytes: Challenges and Strategies, *Nanomaterials* 11 (2021) 2746.

[39] J. Wang, Y. Yang, Y. Zhang, Y. Li, R. Sun, Z. Wang, H. Wang, Strategies towards the Challenges of Zinc Metal Anode in Rechargeable Aqueous Zinc Ion Batteries, *Energy Storage Mater.* 35 (2021) 19-46.

[40] Q.-N. Zhu, Z.-Y. Wang, J.-W. Wang, X.-Y. Liu, D. Yang, L.-W. Cheng, M.-Y. Tang, Y. Qin, H. Wang, Challenges and Strategies for Ultrafast Aqueous Zinc-ion Batteries, *Rare Met.* 40 (2021) 309-328.

[41] M. Song, H. Tan, D. Chao, H. J. Fan, Recent Advances in Zn-Ion Batteries, *Adv. Funct. Mater.* 28 (2018) 1802564.

[42] G. Fang, J. Zhou, A. Pan, S. Liang, Recent Advances in Aqueous Zinc-Ion Batteries, *ACS Energy Lett.* 3 (2018) 2480-2501.

[43] C. Xia, J. Guo, P. Li, X. Zhang, H. N. Alshareef, Highly Stable Aqueous Zinc-ion Storage Using a Layered Calcium Vanadium Oxide Bronze Cathode, *Angew. Chem. Int. Ed.* 57 (2018) 3943-3948.

[44] A. Konarov, N. Voronina, J. H. Jo, Z. Bakenov, Y.-K. Sun, S.-T. Myung, Present and Future Perspective on Electrode Materials for Rechargeable Zinc-ion Batteries, *ACS Energy Lett.* 3 (2018) 2620-2640.

[45] F. Wang, O. Borodin, T. Gao, X. Fan, W. Sun, F. Han, A. Faraone, J. A. Dura, K. Xu, C. Wang, Highly Reversible Zinc Metal Anode for Aqueous Batteries, *Nature Mater.* 17 (2018) 543-549.

[46] Y. Li, H. Dai, Recent Advances in Zinc–air Batteries, *Chem. Soc. Rev.* 43 (2014) 5257-5275.

[47] H. Kim, G. Jeong, Y.-U. Kim, J.-H. Kim, C.-M. Parke, H.-J. Sohn, Metallic anodes for next generation secondary batteries, *Chem. Soc. Rev.* 42 (2013) 9011-9034.

[48] J. F. Parker, C. N. Chervin, I. R. Pala, M. Machler, M. F. Burz, J. W. Long, D. R. Rolison, Rechargeable Nickel–3D Zinc Batteries: An Energy-dense, Safer Alternative to Lithium-ion, *Science* 356 (2017) 415-418.

[49] J. Yi, H. Xhou, A Unique Hybrid Quasi-Solid-State Electrolyte for Li–O_2 Batteries with Improved Cycle Life and Safety, *ChemSusChem* 9 (2016) 2391-2396.
[50] J. Yi P. Liang, Z. Liu, K. Wu, Y. Liu, Y. Wang, Y. Xia, J. Zhang, Challenges, Mitigation Strategies and Perspectives in Development of Zinc-electrode Materials and Fabrication for Rechargeable Zinc–air Batteries, *Energy Environ. Sci.* 11 (2018) 3075.
[51] London Metal Exchange, LME Zn, https://www.lme.com/en/Metals/Non-ferrous/LME-Zinc#Price+graphs (Accessed on February 2nd, 2022).
[52] London Metal Exchange, LME Cobalt, https://www.lme.com/Metals/EV/LME-Cobalt#Price+graphs, (Accessed on February 2nd, 2022).
[53] London Metal Exchange, LME Molybdenum, https://www.lme.com/en/Metals/EV/LME-Molybdenum-Platts#Price+graph, (Accessed on February 2nd, 2022).
[54] I. N. Network, Zn Market Outlook 2022, *Dig Media Inc.* (2022).
[55] Zinc8 Energy Solutions Inc., Zinc-Air Regenerative Fuel Cell System - Zinc8 Energy Solutions, https://www.zinc8energy.com/technology, (Accessed on February 5th, 2022).
[56] T. Mitsumori, H. Iwasaki, Secondary Battery Systems : Quantitative Technology Scenarios, and Science and Technology Roadmap based on Elemental Technology Structure Strategy for Technology Development, Proposal Paper for Policy Making and Governmental Action toward Low Carbon Societies, *Center for Low Carbon Society Strategy, Japan Science and Technology Agency* (2014).
[57] M. Yonezawa, N. Taniguchi, Secondary Battery System (Vol. 9): Cost Evaluation of a Lithium-ion Battery Using Next-Generation Electrode Active Material Proposal Paper for Policy Making and Governmental Action toward Low Carbon Societies, *Center for Low Carbon Society Strategy, Japan Science and Technology Agency* (2021).
[58] M. Yonezawa, K. Saegusa, Secondary Battery Systems (vol. 4): Structure Analysis and Cost Evaluation of a Redox Flow Battery System Strategy for Technology Development, Proposal Paper for Policy Making and Governmental Action toward Low Carbon Societies, *Center for Low Carbon Society Strategy, Japan Science and Technology Agency* (2017).
[59] M. Yonezawa, K. Saegusa, Secondary Battery Systems (vol. 7): Evaluation of the

Economics of Power Storage Systems; Efficiency, Costs and Future Challenges, Proposal Paper for Policy Making and Governmental Action toward Low Carbon Societies, *Center for Low Carbon Society Strategy, Japan Science and Technology Agency* (2020).

[60] N. Wang, H. Wan, J. Duan, X. Wang, L. Tao, J. Zhang, H. Wang, A Review of Zinc-based Battery from Alkaline to Acid, *Mater. Today Adv.* 11 (2021) 100149.

[61] S. Higashi, S. W. Lee, J. S. Lee, K. Takeuchi, Y. Cui, Avoiding Short Circuits from Zinc Metal Dendrites in Anode by Backside-plating Configuration, *Nat. Commun.* 7 (2016) 11801.

[62] FUJIFILM Wako Pure Chemical Corporation, Cobalt(2,3) Oxide, https://labchem-wako.fujifilm.com/jp/product/detail/W01W0103-0879.html, (Accessed on 25th April, 2022).

[63] FUJIFILM Wako Pure Chemical Corporation, Cobalt(II) sulfate heptahydrate, 98+%, https://labchem-wako.fujifilm.com/jp/product/detail/W01SRM93-2749.html, (Accessed on 25th April, 2022).

[64] FUJIFILM Wako Pure Chemical Corporation, Cobalt(II) hydroxide, 97%, https://labchem-wako.fujifilm.com/jp/product/detail/W01AFAB22045.html, (Accessed on 25th April, 2022).

[65] FUJIFILM Wako Pure Chemical Corporation, Lithium Carbonate, https://labchem-wako.fujifilm.com/jp/product/detail/W01W0112-0113.html, (Accessed on 25th April, 2022).

[66] FUJIFILM Wako Pure Chemical Corporation, Lithium Hydroxide Monohydrate, https://labchem-wako.fujifilm.com/jp/product/detail/W01W0112-0121.html, (Accessed on 25th April, 2022).

[67] FUJIFILM Wako Pure Chemical Corporation, Cobalt(II) carbonate, 99% (metals basis), Co 45% min, https://labchem-wako.fujifilm.com/jp/product/detail/W01ALF011343.html, (Accessed on 25th April, 2022).

[68] FUJIFILM Wako Pure Chemical Corporation, Ethylene Carbonate, https://labchem-wako.fujifilm.com/jp/product/detail/W01W0105-0849.html, (Accessed on 25th April, 2022).

[69] FUJIFILM Wako Pure Chemical Corporation, Lithium Hexafluorophosphate, https://labchem-wako.fujifilm.com/jp/product/detail/W01W0112-0592.html, (Accessed on 25th April, 2022).

[70] FUJIFILM Wako Pure Chemical Corporation, Graphite, Powder, https://labchem-wako.fujifilm.com/jp/product/detail/W01W0107-0384.html, (Accessed on 25th April, 2022).

[71] FUJIFILM Wako Pure Chemical Corporation, Zinc, https://labchem-wako.fujifilm.com/jp/product/detail/W01W0126-0009.html, (Accessed on 25th April, 2022).

[72] FUJIFILM Wako Pure Chemical Corporation, Potassium Hydroxide, https://labchem-wako.fujifilm.com/jp/product/detail/W01W0116-2181.html, (Accessed on 25th April, 2022).

[73] FUJIFILM Wako Pure Chemical Corporation, Nickel(II) Hydroxide, https://labchem-wako.fujifilm.com/jp/product/detail/W01W0114-0557.html, (Accessed on 25th April, 2022).

[74] C. Xu, B. Li, H. Du, F. Kang, Energetic Zinc Ion Chemistry: The Rechargeable Zinc Ion Battery, *Angew. Chem. Int. Ed.* 51 (2012) 933-935.

[75] T. Yamamoto, T. Shoji, Rechargeable Zn|$ZnSO_4$|MnO_2-type Cells, *Inorganica Chim. Acta* 117 (1986) L27-L28.

[76] L. Ma, S. Chen, H. Li, Z. Ruan, Z. Tang, Z. Liu, Z. Wang, Y. Huang, Z. Pei, J. A. Zapiena, Initiating a Mild Aqueous Electrolyte Co_3O_4/Zn Battery with 2.2 V-high Voltage and 5000-cycle Lifespan by a Co(III) Rich-electrode, *Energy Environ. Sci.* 11 (2018) 2521-2530.

[77] C. Zhong, B. Liu, J. Ding, X. Liu, Y. Zhong, Y. Li, C. Sun, X. Han, Y. Deng, N. Zhao, W. Hu, Decoupling Electrolytes towards Stable and High-energy Rechargeable Aqueous Zinc–manganese Dioxide Batteries, *Nat. Energy* 5 (2020) 440-449.

[78] Z. Wang, H. Li, Z. Tang, Z. Liu, Z. Ruan, L. Ma, Q. Yang, D. Wang, C. Zhi, Hydrogel Electrolytes for Flexible Aqueous Energy Storage Devices, *Adv. Funct. Mater.* 28 (2018) 1804560.

[79] Z. Mao, S. Srinivasan, A. J. Appleby, Effect of PbO on Zinc Electrodeposition from Zincate Solutions, *J. Appl. Electrochem.*, 22 (1992) 693-698.

[80] T. Otani, Y. Tetsuya, K. Masahiro, M. Yanagisawa, Y. Fukunaka, T. Homma, Effect of Li^+ Addition on Growth Behavior of ZnO during Anodic Dissolution of Zn Negative Electrode, *Electrochim. Acta* 305 (2019) 90-100.

[81] V. Yurkiv, T. Foroozan, A. Ramasubramanian, M. Ragone, S. Sharifi-Asl, R. Paoli, R. Shahbazian-Yassar, F. Mashayek, The Mechanism of Zn Diffusion Through ZnO in Secondary Battery: A Combined Theoretical and Experimental Study, *J. Phys. Chem. C* 124 (2020) 15730-15738.

[82] A. R. Despic, J. Diggle, J. O'M. Bockris, Mechanism of the Formation of Zinc Dendrites, *J. Electrchem. Soc.* 115 (1968) 507-508.

[83] T. Otani, M. Nagata, Y. Fukunaka, T. Homma, Morphological Evolution of Mossy Structures during the Electrodeposition of Zinc from an Alkaline Zincate Solution, *Electrcochim. Acta* 206 (2016) 366-373.

[84] T. Otani, Y. Fukunaka, T. Homma, Effect of Lead and Tin Additives on Surface Morphology Evolution of Electrodeposited Zinc, *Electrochim. Acta*, 242 (2017) 364-372.

[85] S. Zhi, G. Wanga, Z. Zeng, L. Zhu, Z. Liu, D. Zhang, K. Xu, Q. Xue, 3D Mossy Structures of Zinc Filaments: A Facile Strategy for Superamphiphobic Surface Design, *J. Collloid Interface Sci.*, 526 (2018) 106-113.

[86] M. Huang, M. Li, C. Niu, Q. Li, L. Mai, Recent Advances in Rational Electrode Designs for High-Performance Alkaline Rechargeable Batteries, *Adv. Funct. Mater.* 29, (2019) 1807847.

[87] F. R. McLarnon, E. J. Cairns, The Secondary Alkaline Zinc Electrode, *J. Electrochem. Soc.*, 138 (1991) 645-664.

[88] J. Pan, Y. Y. Xu, H. Yang, Z. Dong, H. Liu, B. Y. Xia, Advanced Architectures and Relatives of Air Electrodes in Zn–Air Batteries, *Adv. Sci.* 5 (2018) 1700691.

[89] J.-S. Lee, S. T. Kim, R. Cao, N.-S. Choi, M. Liu, K. T. Lee, Metal–Air Batteries with High Energy Density: Li–Air versus Zn–Air, *Adv. Energy Mater.* 1 (2011) 34-50.

[90] J. Fu, Z. P. Cano, M. G. Park, A. Yu, M. Fowler, Electrically Rechargeable Zinc–Air Batteries: Progress, Challenges, and Perspectives, *Adv. Mater.*, 29 (2017) 1604685.

[91] M. Xu, D. Ivey, Z. Xie, W. Qu, Rechargeable Zn-air Batteries: Progress in Electrolyte Development and Cell Configuration Advancement, *J. Power Sources* 283

(2015) 358-371.

[92] R. Y. Wang, D. W. Kirk, G. X. Zhang, Effects of Deposition Conditions on the Morphology of Zinc Deposits from Alkaline Zincate Solutions, *J. Eelctrochem. Soc.* 153 (2006) C357-C364.

[93] T. Mitsuhashi, Y. Ito, Y. Takeuchi, S. Harada, T. Ujihara, Non-uniform Electrodeposition of Zinc on the (0001) Plane, *Thin Solid Films* 590 (2015) 207-213.

[94] S. A. Morin, M. J. Bierman, J. Tong, S. Jin, Mechanism and Kinetics of Spontaneous Nanotube Growth Drivenby Screw Dislocations, Science 328 (2010) 476-480.

[95] K. Kamei, H. Yumoto, Electrodeposition of Zn-Ni Alloy Whisker, *J. Japan Inst. Metals* 57 (1993) 1227-1234.

[96] B. E. Conway, J. O'M Bockris, On the Calculation of Potential Energy Profile Diagrams for Processes in Electrolytic Metal Deposition, *Electrochim. Acta* 3 (1961) 340-366.

[97] R. M. Stephens, R. C. Alkire, Simulation of Kinetically Limited Nucleation and Growth at Monatomic Step Edges, *J. Electrochem. Soc.* 154 (2007) D418-D426.

[98] G. Ehrlich, F. G. Hudda, Atomic View of Surface Self-Diffusion: Tungsten on Tungsten, *J. Chem. Phys.* 44 (1966) 1039-1049.

[99] R. L. Schwoebel, E. J. Shipsey, Step Motion on Crystal Surfaces, *J. Appl. Phys.* 37 (1966) 3682-3686.

[100] C. W. Lee, K. Sathiyanarayanan, S. W. Eoma, H. S. Kima, M. S. Yun, Novel Electrochemical Behavior of Zinc Anodes in Zinc/air Batteries in the Presence of Additives, *J. Power Sources* 159 (2006) 1474-1477.

[101] L. Morón, A. Méndez, F. Castañeda, J. Flores, L. Ortiz-Frade, Y. Meas, G. Trej, Electrodeposition and Corrosion Behavior of Zn Coatings Formed using as Brighteners Arene Additives of Different Structure, *Surf. Coat. Technol.* 205 (2011) 4985-4992.

[102] M. F. De Carvalho, I. A. Carlos, Zinc Electrodeposition from Alkaline Solution Containing Trisodiumnitrilotriacetic Nitrilotriacetic Added, *Electrochim. Acta* 113 (2013) 229-239.

[103] S. Khorsand, K. Raeissi, M. A. Golozar, Effect of Oxalate Anions on Zinc Electrodeposition from an Acidic Sulphate Bath, *J. Electrochem. Soc.* 158 (2011) D377-

D383.

[104] M. Pereira, L. Barbosa, C. Souza, A. De Moraes, I. Carlos, The Influence of Sorbitol on Zinc Film Deposition, Zinc Dissolution Process and Morphology of Deposits Obtained from Alkaline Bath, *J. Appl. Electrochem.* 26 (2006) 727-732.

[105] L. Chladil, O. Čech, J. Smejkala, P. Vanýseka, Study of Zinc Deposited in the Presence of Organic Additives for Zinc-based Secondary Batteries, *J. Energy Storage* 21 (2019) 295-300.

[106] S. J. Banik, R. Akolkar, Suppressing Dendritic Growth during Alkaline Zinc Electrodeposition using Polyethylenimine Additive, *Electrochim. Acta* 179 (2015) 475-481.

[107] A. Sumboja, P. L. Sambegoro, A Stability Improvement of Rechargeable Zn-air Batteries by Introducing Thiourea and Polyethylenimine as Electrolyte Additives, *5th International Conference on Electric Vehicular Technology (ICEVT)* (2018) 128-131.

[108] M.-H. Lin, C.-J. Huang, P.-H. Cheng, J.-H. Cheng, C.-C. Wang, Revealing the Effect of Polyethylenimine on Zinc Metal Anodes in Alkaline Electrolyte Solution for Zinc–air Batteries: Mechanism Studies of Dendrite Suppression and Corrosion Inhibition, *J. Mater. Chem. A* 8 (2020) 20637-20649.

[109] M. Yan, C. Xu, Y. Sun, H. Pan, H. Li, Manipulating Zn Anode Reactions through Salt Anion Involving Hydrogen Bonding Network in Aqueous Electrolytes with PEO Additive, *Nano Energy* 82 (2021) 105739.

[110] C. Mele, B. Bozzini, Spectroelectrochemical Investigation of the Anodic and Cathodic Behaviour of Zinc in 5.3 M KOH, *J. Appl. Electrochem.* 45 (2015) 43-50.

[111] M. Shimizu, K. Hirahara, S. Arai, Morphology Control of Zinc Electrodeposition by Surfactant Addition for Alkaline-based Rechargeable Batteries, *Phys. Chem. Chem. Phys.* 21 (2019) 7045-7052.

[112] G. F. Tiétcha, L. L. E. Mears, D. Dworschak, M. Roth, I. Klüppel, M. Valtiner, Adsorption and Diffusion Moderated by Polycationic Polymers during Electrodeposition of Zinc, *ACS Appl. Mater. Interfaces* 12 (2020) 29928-29936.

[113] M. Xu, D. Ivey, W. Qu, Z. Xie, Study of the Mechanism for Electrodeposition of Dendrite-free Zinc in an Alkaline Electrolyte Modified with 1-ethyl-3-methylimidazolium Dicyanamide, *J. Power Sources* 274 (2015) 1249-1253.

[114] Z. Liu, T. Cui, G. Pulletikurthi, A. Lahiri, T. Carstens, M. Olschewski, F. Endres, Dendrite-Free Nanocrystalline Zinc Electrodeposition from an Ionic Liquid Containing Nickel Triflate for Rechargeable Zn-Based Batteries, *Angew. Chem. Int. Ed.* 55 (2016) 2889-2893.

[115] K. Miyazaki, A. Nakata, Y.-S. Lee, T. Fukutsuka, T. Abe, "nfluence of Surfactants as Additives to Electrolyte Solutions on Zinc Electrodeposition and Potential Oscillation Behavior, *J. Appl. Electrochem.* 46 (2016) 1067-1073.

[116] K. Nayana, T. Venkatesha, Synergistic Effects of Additives on Morphology, Texture and Discharge Mechanism of Zinc during Electrodeposition, *J. Electroanal. Chem.* 663 (2011) 98-107.

[117] J. Zhu, Y. Zhou, C. Gao, Influence of Surfactants on Electrochemical Behavior of Zinc Electrodes in Alkaline Solution, *J. Power Sources* 72 (1998) 231-235.

[118] A. Bayaguud, X. Luo, Y. Fu, C. Zhu, Cationic Surfactant-Type Electrolyte Additive Enables Three-Dimensional Dendrite-Free Zinc Anode for Stable Zinc-Ion Batteries, *ACS Energy Lett.* 5 (2020) 3012-3020.

[119] M. Kim, D. Yun, J. Jeon, Effect of a Bromine Complex Agent on Electrochemical Performances of Zinc Electrodeposition and Electrodissolution in Zinc–bromide Flow Battery, *J. Power Sources* 438 (2019) 227020.

[120] K. Fukumoto, S. Oue, T. Niwa, Y. Kikuchi, S. Akamatsu, H. Nakano, Effect of Organic Additives on Electrodeposition Behavior of Zn from Zincate Solution Containing Potassium Hydroxide and Its Micro Structure, *Mater. Trans.* 62 (2021) 807-814.

[121] P. Thakur, K. Alam, A. Roy, C. Downing, V. Nicolosi, P. Sen, T. N. Narayanan, Extending the Cyclability of Alkaline Zinc−Air Batteries: Synergistic Roles of Li^+ and K^+ Ions in Electrodics, *ACS Appl. Mater. Interfaces* 13 (2021) 33112-33122.

[122] X. Guo, Z. Zhang, J. Li, N. Luo, G.-L. Chai, T. S. Miller, F. Lai, P. Shearing, D. J. L. Brett, D. Han, Z. Weng, G. He, I. P. Parkin, Alleviation of Dendrite Formation on Zinc Alleviation of Dendrite Formation on Zinc Anodes via Electrolyte Additives, *ACS Energy Lett.* 6 (2021) 395-403.

[123] T. Otani, T. Yasuda, M. Kunimoto, M. Yanagisawa, Y. Fukunaka, T. Homma, Effect of Li^+ Addition on Growth Behavior of ZnO during Anodic Dissolution of Zn

Negative Electrode, *Electrochim. Acta* 305 (2019) 90-100.

[124] M. Nakamura, Y. Nakajima, N. Hoshi, H. Tajiri, O. Sakata, Effect of Non-Specifically Adsorbed Ions on the Surface Oxidation of Pt(111), *ChemPhysChem* 14 (2013) 2426-2431.

[125] M. Ohba, T. Scarazzato, D. Espinosa, Z. Panossian, Study of Metal Electrodeposition by Means of Simulated and Experimental Polarization Curves: Zinc Deposition on Steel Electrodes, *Electrochim. Acta* 309 (2019) 86-103.

[126] B. Kubo, S. Oue, T. Futaba, A. Kobayashi, Y. Goto, H. Nakano, Effect of Surface Textures of Iron Substrate on the Crystal Orientation Relationship between Electrodeposited Zinc and Iron, *ISIJ Int.* 59 (2019) 144-151.

[127] T. Otani, T. Okuma, T. Homma, Effect of Indiumand Tin Additives on the Surface Morphology of Zinc Negative Electrodes for Zn-Ni Flow-assisted Batteries, *J. Electroanal. Chem.* 878 (2020) 114583.

[128] J. McBreen, M. Chu, G. Adzic, Substrate Effects on Zinc Deposition from Zincate Solutions, *J.Electrochem. Soc.* 128, (1981) 2287-2292.

[129] H.-I. Kim, H.-C. Shin, SnO Additive for Dendritic Growth Suppression of Electrolytic Zinc, *J. Alloys Compd.* 645 (2015) 7-10.

[130] F. Mansfeld, S. Gilman, The Effect of Tin and Tetraethylammonium Ions on the Characteristics of Zinc Deposition on a Zinc Single Crystal in Aqueous KOH, *J. Electrochem. Soc.* 117 (1970) 1154-1155.

[131] J. McBreen, E. Gannon, Bismuth Oxide as an Additive in Pasted Zinc Electrodes, *J. Power Sources* 15 (1985) 169-177.

[132] M. Schmid, M. Willert-Porada, Zinc Particles Coated with Bismuth Oxide Based Glasses as Anode Material for Zinc Air Batteries with Improved Electrical Rechargeability, *Electrochim. Acta* 260 (2018) 246-253.

[133] J. W. Gallaway, A. M. Gaikwad, B. Hertzberg, C. K. Erdonmez, Y.-C. K. Chen-Wiegart, L. A. Sviridov, K. Evans-Lutterodt, J. Wang, S. Banerjee, D. A. Steingartb, An In Situ Synchrotron Study of Zinc Anode Planarization by a Bismuth Additive, *J. Electrochem. Soc.* 161 (2014) A275-A284.

[134] F. Mansfeld, S. Gilman, The Effect of Lead Ions on the Dissolution and Deposition Characteristics of a Zinc Single Crystal in 6N KOH, *J. Electrochem. Soc.*

117 (1970) 588-592.

[135] Y.-H. Wen, J. Cheng, L. Zhang, X. Yana, Y.-S. Yanga, The Inhibition of the Spongy Electrocrystallization of Zinc from Doped Flowing Alkaline Zincate Solutions, *J. Power Sources* 193 (2009) 890-894.

[136] J. Bressan, R. Wiart, Use of Impedance Measurements for the Control of the Dendritic Growth of Zinc Electrodeposits, *J. Appl. Electrochem.* 7 (1977) 505-510.

[137] P. Giannozzi, S. Baroni, N. Bonini, M. Calandra, R. Car, C. Cavazzoni, D. Ceresoli, G. Chiarotti, M. Cococcioni, I. Dabo et al., QUANTUM ESPRESSO: a Modular and Open-source Software Project for Quantum Simulations of Materials, *J. Phys. Condens. Matter* 21 (2009) 395502.

[138] P. Giannozzi, O. Andreussi, T. Brumme, O. Bunau, M. Nardelli, M. Calandra, R. Car, C. Cavazzoni, D. Ceresoli, M. Cococcioni et al., Advanced Capabilities for Materials Modelling with Quantum ESPRESSO, *J. Phys. Condens. Matter* 29 (2017) 465901.

[139] G. Kresse, J. Hafner, Ab Initio Molecular Dynamics for Liquid Metals, *Phys. Rev. B* 47 (1993) 558-561.

[140] G. Kresse, J. Hafner, Ab Initio Molecular-dynamics Simulation of the Liquid-metal — Amorphous-semiconductor Transition in Germanium, *Phys. Rev. B* 49 (1994) 14251-14269.

[141] G. Kresse, Dissociation and Sticking of H_2 on the Ni(111), (100), and (110) Substrate, *Phys. Rev. B* 62 (2000) 8295-8305.

[142] J. M. Soler, E. Artacho, J. D. Gale, A. García, J. Junquera, P. Ordejón, D. Sánchez-Portal, The SIESTA Method for Ab Initio Order-N Materials Simulation, *J. Phys. Condens. Matter* 14 (2002) 2745-2779.

[143] D. S. Sholl, J. A. Steckel, Density Functional Theory A Practical Introduction translated into Japanese by T. Sasaki and S. Suehara, *Yoshikawa Shoten* (2014).

[144] M. Kunimoto, K. Seki, H. Nakai, T. Homma, Theoretical Analysis of Adsorption Structure of Hydrated Hypophosphite Ion on Pd(111) Surface, *Electrochemstry* 80 (2012) 222-225.

[145] Y. Onabuta, M. Kunimoto, H. Nakai, T. Homma, First-principle Study of the Oxidation Mechanism of Formaldehyde and Hypophosphite for Copper and Nickel

Electroless Deposition Process, *Electrochim. Acta* 307 (2019) 536-542.

[146] K. Masahiro, D. Bothe, R. Tamura, T. Oyanagi, Y. Fukunaka, H. Nakai, T. Homma, Spectroscopic and Computational Analyses of Liquid−Liquid Interfacial Reaction Mechanism of Boric Acid Esterification with 2,2,4-Trimethyl-1,3-pentanediol in Boron Extraction Processes, *J. Phys. Chem. C* 122 (2018) 10423-10429.

[147] E. Cancés, B. Mennucci, J. Tomasi, A New Integral Equation Formalism for the Polarizable Continuum Model: Theoretical Background and Applications to Isotropic and Anisotropic Dielectrics, *J. Chem. Phys.* 107 (1997) 3032-3041.

[148] S. Nishihara, M. Otani, Hybrid Solvation Models for Bulk, Interface, and Membrane: Reference Interaction Site Methods Coupled with Density Functional Theory, *Phys. Rev. B* 96 (2017) 115429.

[149] J. Haruyama, T. Ikeshoji, M. Otani, Electrode Potential from Density Functional Theory Calculations Combined with Implicit Solvation Theory, *Phys. Rev. Mater.* 2 (2018) 095801.

[150] J. Haruyama, T. Ikeshoji, M. Otani, Analysis of Lithium Insertion/Desorption Reaction at Interfaces between Graphite Electrodes and Electrolyte Solution Using Density Functional + Implicit Solvation Theory, *J. Phys. Chem. C* 122 (2018) 9804-9810.

[151] K. Wang, P. Pei, Z. Ma, H. Chen, H. Xu, D. Chen, X. Wang, Dendrite Growth in the Recharging Process of Zinc–air Batteries, *J. Mater. Chem. A* 3 (2015) 22648-22655.

[152] V. Yurkiv, T. Foroozan, A. Ramasubramanian, M. Ragone, R. Shahbazian-Yassar, F. Mashayek, Understanding Zn Electrodeposits Morphology in Secondary Batteries Using Phase-Field Model, *J. Electrochem. Soc.* 167 (2020) 060503.

[153] P. Xiao, G. Henkelman, Kinetic Monte Carlo Study of Li Intercalation in $LiFePO_4$, *ACS Nano* 12 (2018) 844-851.

[154] R. M. Stephens, M. Willis, R. C. Alkire, Additive-Assisted Nucleation and Growth by Electrodeposition II. Mathematical Model and Comparison with Experimental Data, *J. Electrochem. Soc.* 156 (2009) D385-D394.

[155] X. Li, T. O. Drews, E. Rusli, F. Xue, Y. He, R. Braatz, R. Alkire, Effect of Additives on Shape Evolution during Electrodeposition I. Multiscale Simulation with Dynamically Coupled Kinetic Monte Carlo and Moving-Boundry Finite-Volume Codes,

J. Electrochem. Soc. 154 (2007) D230-D240.

[156] E. Rusli, F. Xue, T. O. Drews, P. M. Vereecken, P. Andricacos, H. Deligianni, R. D. Braatz, R. C. Alkire, Effect of Additives on Shape Evolution during Electrodeposition II. Parameter Estimation from Roughness Evolution Experiments, *J. Electrochem. Soc.* 154 (2007) D584-D597.

[157] A. Aryanfar, D. Brooks, B. V. Merinov, W. A. Goddard III, A. J. Colussi, M. R. Hoffmann, Dynamics of Lithium Dendrite Growth and Inhibition: Pulse Charging Experiments and Monte Carlo Calculations, *J. Phys. Chem. Lett.* 5 (2014) 1721-1726.

[158] D. A. McQuarrie, Mathematical Mehods for Scientists and Engineers translated into Japanese by M. Irie and M. Irie, *Kodansha Ltd.* (2009).

Chapter 2:

Multiscale Simulation by DFT and KMC Simulations of the Initial Stage of Zn Shape Evolution during Electrodeposition

2.1. Introduction

As shown in Chapter 1, understanding the growth mechanism of the layer-by-layer structures, which is considered as the phenomena before the protrusion appears, is required as the first step of the analysis. This is because understanding such deposition behavior can be a step toward further analysis for the irregular shape evolution. However, it is difficult to observe and analyze the behavior at the atomic level during the initial stages of electrodeposition. In general, electrodeposition involves the reduction of precursors, surface diffusion of metal adatoms, and incorporation of adatoms into the deposit. Adatom incorporation via surface diffusion can be a significant factor, especially at low current densities, as these atomic-level steps determine crystal growth behavior and morphological changes in electrodeposition [1,2]. To understand the irregular deposition mechanism consisting of these steps, electrodeposition should be analyzed at the atomic scale as mentioned in Chapter 1. Such an analysis will allow us to discuss the origin of the shape evolution mechanism from an atomistic perspective. This atomistic perspective will be advanced in combination with the conventional understanding of the electrodeposition process. Theoretical calculations are a powerful tool to demonstrate the qualitative analysis of such phenomena at the atomic scale.

Density functional theory (DFT) has been used in many atomic-scale analyses of chemical processes, such as solid-liquid interface processes [3,4]. Adatom surface diffusion and metal atom adsorption have also been analyzed with DFT [5,6]. Although these studies provide mechanistic understanding of each process with respect to electronic state, DFT calculations cannot analyze stochastic phenomena such as shape evolution over much larger areas. Kinetic Monte Carlo (KMC) simulations are stochastic simulations that extend the scale of analysis from the atomic level to the mesoscale and model precipitation and nucleation [7,8]. Since DFT models phenomena on the picometer scale and KMC on the nanometer scale, the combination of these methods is expected to expand the scale of analysis. In addition, DFT provides information on the electronic state of surface species such as adsobates and surface atoms. Therefore, the multiscale simulation that utilizes DFT and KMC simulaitons may be able to explain the shape

change of Zn based on its electronic state.

In this chapter, it is focused on to understand the initial deposition mechanism of Zn which shows the layer-by-layer strucures. For this analysis, a multiscale simulation approach consisting of DFT to analyze atomic-scale phenomena and KMC simulations was used to analyze mesoscale phenomena. As mentioned above, at low current densities, the surface diffusion can be a dominant factor for the shape evolution because the supply of the precursor is slow rate, which is a reaction limited condition. In addition, the surface can be pure Zn because the reduction of the Zn precursor in the alkaline condition shows a relatively high value of the exchange current density [9,10]. Hence, the activation energy of surface diffusion calculated by DFT were used in the KMC simulations to understand how such DFT parameters affect shape evolution. DFT calculations at the solid-liquid interface were performed using the effective screening medium (ESM) combined with reference interaction site model (RISM) [11,12]. Activation energies for surface diffusion of Zn adatom are calculated using several models of the Zn facets. Thus, atomic-scale DFT calculations provide the activation energy of Zn adatom surface diffusion with respect to the surface atomic configuration during Zn electrodeposition, and mesoscale KMC simulations reveal the shape evolution of the initial stage of Zn electrodeposition based on the activation energy calculated by DFT. In summary, a multiscale simulation model using DFT and KMC was constructed under the following assumptions: (i) low current density, (ii) reaction limited condition, and (iii) sufficient time for the surface diffusion of adsorbed atoms. This simulation enables to analyze electrodeposition phenomena on the pico- to nanometer-scale, which has been difficult with conventional electrochemical measurements, and is expected to elucidate the mechanism of shape evolution. The consistent analytical results obtained in this chapter can contribute to obtaining desirable electrodeposits with a more appropriate experimental setup from a theoretically rational viewpoint.

2.2. Methods

2.2.1. DFT calculations for the surface diffusion of the Zn adatom on the Zn surface

Quantum ESPRESSO code were used for all DFT calculations [13,14]. The RISM component for the ESM-RISM calculations describing the solid-liquid interface with the slab models was implemented by Nishihara [15]. The Kohn-Sham equations were solved using a plane-wave basis within the ultrasoft pseudopotential framework [16-18], which was expanded to a cutoff energy of 40 Ry. The cutoff energy for the augmented charge was set at 320 Ry, and the exchange correlation energies were calculated using the Perdew-Burke-Ernzerhof form of the generalized gradient approximation [19]. Geometrical optimizations to obtain the potential curves of the surface diffusion were performed with convergence thresholds of 10^{-4} Ry and 2.0×10^{-3} Ry/Bohr for energy and forces, respectively. A unit cell was sampled with Monkhorst-Pack k-point grids ($1 \times 1 \times 1$) to establish the first Brillouin zone [20].

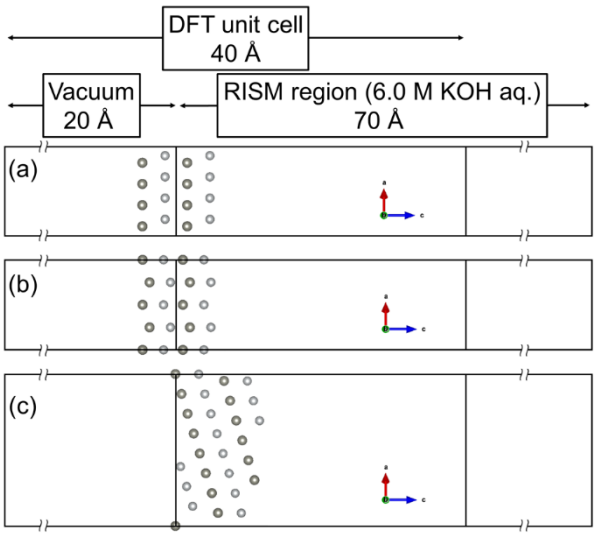

Figure 2.1. Supercells of the ESM-RISM calculations: (a) Zn(0001), (b) Zn(0−110), and (c) Zn(0001) step-terrace models. All dots represent the Zn atoms. Zn adatom is added on each facet. The adatom adsorbs on the right hand side of the slab.

The slab models of the Zn(0001) and Zn(0−110) surfaces and a step-terrace model of the Zn(0001) surface were shown in Figure 2.1. These models were prepared by cutting the hexagonal close-packed (hcp) structure of Zn. The lattice constants of the hcp-Zn were set at a = 2.665 Å and c = 4.947 Å (experimental values). In order to compare the surface diffusion behavior with respect to the electronic state correpsoding to the periodic table, four-layer slab of the Cu(111) surface and a step-terrace model of the Cu(111) surface were also prepared by cutting the face-centered cubic (fcc) structure. The lattice constant of Cu was set at 3.615 Å (experimental value). The potential curves of the adatom surface diffusion on each surface were calculate using these slab models. The bottom two layers of each model were fixed in all calculations.

The DFT unit cell and RISM component exhibited c-axis lengths of 40 and 50 Å, respectively. The zero point of the z-axis is indicated in the vertical second black line of the four in Figure 2.1. The right hand side square region surrounded by the black lines indicates the vacuum region with 20 Å to settle the electrostatic force of the bottom of the slab models. The middle and left hand side square region surrounded by the black lines indicates the RISM region. The RISM method, which is the implicit theory treating the electrolyte species without the concrete model of molecules such as water, KOH, and LiOH, yields the distribution of the atoms composing the molcules in the electrolyte [21]. The solvent system in the RISM component was set at 6.0 mol/L KOH solution. This electrolyte condition is derived from previous studies [22,23], which is a typical alkaline condition for alkaleine Zn electrodeposition processes. The ESM-RISM methods can describe the distribution of the electrolyte species at the solid-liquid interface except for the specific adsorption anion [21]. The temperature was set at 300 K. The Laue-RISM calculations were performed with the Kovalenko-Hirata closure model [24] and introduced by Nishihara et al. [15] to reproduce the electrochemical interface with a mixed boundary condition where an open boundary condition was implemented on the right and left sides of the slab models as shown in Figure 2.1. The cutoff energy for the distribution functions of the RISM components was set at 144 Ry, and the convergence criteria of the correlation functions in the one dimensional - RISM and three dimensional - RISM equations were set at 10^{-8} and 10^{-5} Ry, respectively. The classical force field parameter of water was selected as the simple point charge model [25], and the optimized

potentials for liquid simulation were used for the parameters of K^+ and OH^- [26,27]. Lennard-Jones (LJ) parameters for Zn atoms were set as ε = 0.7898 kcal mol^{-1}, σ = 3.471 Å. The LJ parameters of Zn are calculted by the interaction energy between Zn and Xe (Table 2.1) [21]. For the calculations of the LJ parameters, Gaussian 09 was used with the basis set of DGDZVP and the exchange-correlation functional of WB97XD. The LJ parameters of Zn is not fully discussed yet [28]. The ESM-RISM caluculations with the LJ parameters of the universal force field (ε = 0.124 kcal mol^{-1}, σ = 2.763 Å [29]) was not converged.

Table 2.1. Calculated Lennard-Jones (LJ) parameters for LJ parameters of Zn.
LJ potential between Xe and Xe, Zn and Xe was calculated as follows: LJ potential: $u(r) = 4\varepsilon\left\{\left(\frac{\sigma}{r}\right)^{12} - \left(\frac{\sigma}{r}\right)^{6}\right\}$, $\sigma = \frac{r}{\sqrt[6]{2}}$ (where $u(r)$ is minimum). The LJ parameters are determined with the standard combining rules: $\sigma_{Xe-Zn} = \frac{\sigma_{Xe}+\sigma_{Zn}}{2}$, $\varepsilon_{Xe-Zn} = \sqrt{\varepsilon_{Xe}\varepsilon_{Zn}}$.
DGDZVP and WB97XD incorporated in Gaussian09 was used as the basis set and exchange-correlation functional, respectively.

σ_{Xe} / Å	$\sigma_{Xe\text{-}Zn}$ / Å	ε_{Xe} / kcal mol^{-1}	$\varepsilon_{Xe\text{-}Zn}$ / kcal mol^{-1}
4.162	3.816	0.5228	0.6426

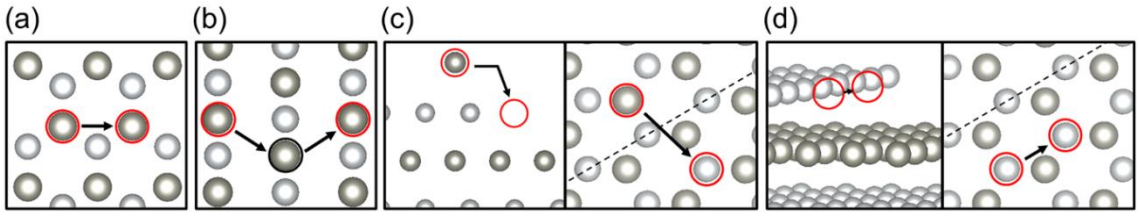

Figure 2.2. Surface diffusion pathways on the Zn(0001) and (0−110) surfaces: (a) top view of the (0001) surface, (b) the top view of the (0−110) surface, (c) side and top views of the interlayer diffusion on the (0001) surface, and (d) side and top views of the edge diffusion on the (0001) surface. Red circles show the start point and the end point of the diffusion. All balls exhibit the Zn atoms. Black arrows denote the pathways of the diffusions. In the top views of (c) and (d), dashed lines show the step boundary of the top layer.

Table 2.2. Relative energy of the Zn adatom adsorption at each site. The total energy of the adsorption at bridge site is zero. K-points was set as 2 × 2 × 1.

Bridge / kJ mol^{-1}	Hollow-hcp / kJ mol^{-1}	Hollow-fcc / kJ mol^{-1}	Top / kJ mol^{-1}
0.0	−1.85	+1.65	+3.93

The activation barriers of the Zn adatom surface diffusion were calculated for the assumed diffusion pathways on the representative facets shown in Figure 2.2. The (0001) surface is the most dense and stable facet of the hcp structure. The optimization results of the adsorption of the Zn adatom is shown in Table 2.2. The Zn adatom adsorbs on the hollow hcp site on the (0001) surface. Hence, the pathway of the surface diffusion is assumed from a hollow hcp site to another hollow hcp site as shown in the red circles in Figure 2.2(a). A (0−110) surface is used as the representative facet of a [0001] direction. Figure 2.2(b) shows the diffusion pathway on the (0−110) surface. As for the (0−110) surface, the red circles indicate the initial and final states, and the black circle indicates the transition state of the pathway. The pathway that the Zn adatom is step downward called “interlayer diffusion” hereafter is shown in Figure 2.2(c). Among the surface diffusion pathways, the interlayer diffusion with the activation energy commonly known as the Ehrlich-Schwoebel (ES) barrier [30,31] may play an important role in crystal growth because the ES barrier is the dominant factor for the adatom diffusion rate of migrating downward from the deposited atomic layer of the (0001) facets to the lower layer. The adatom migrates from the hollow hcp site of the upper terrace to the hollow hcp site of the bottom step, which is the nearest lower-layer site to the higher layer. This pathway can be observed during the deposition of the new layer (the upper layer) on the (0001) surface in electrodeposition. Figure 2.2(d) shows the edge diffusion at the step, which exhibits a unique behavior. The adatom migrates along the edge of the upper layer attaching with the step. The pathway is shown in Figure 2.2(d) as red circles. These four types of the surface diffusion on the metal surfaces were analyzed. In order to obtain the potential curves of these four pathways, the geometries of the migrating adatoms located at several sites along the diffusion pathway were optimized. The position of the adatom was fixed during the optimization. As for the (0−110) surface, the potential curve was calculated by fixing the surface with the relaxation of z-axis of the Zn adatom to investigate the characteristics of the (0−110) surface without any distortion. Since the

nudged elastic band calculation for the trasnsition state calculations is not implemented for the ESM-RISM calculations, the adatom is required to be fix at least one axis. The relative energies at each site along the diffusion pathways of the surface diffusion are calculated using the following equation:

$$E_{\mathrm{re}} = E_{\mathrm{each\_position}} - E_0 \quad (2.1)$$

where $E_{\mathrm{each\_position}}$ denotes the total energy of the adsorption structure of the Zn adatom at each position during the surface diffusion and E_0 denotes the total energy of the adsorption structure of the Zn adatom at the initial point prior to surface diffusion. The activation barrier was defined here as the highest relative energy in each potential curve.

2.2.2. KMC simulations of the shape evolution with the activation energy calculated by DFT

The rejection-free KMC code that follows the Bortz-Kalos-Lebowitz algorithm [32] was constructed to conduct a time-dependent simulation during the initial stage of the Zn electrodeposition. For the simulation of the electrodeposition, the deposition and the surface diffusion should be included as the possible events of the electrodeposition. Based on the conditions that appears the layer-by-layer structures as mentioned above, following assumptions are introduced: (i) low current density, (ii) reaction limited condition, and (iii) sufficient time for the surface diffusion of adsorbed atoms. During the Zn electrodeposition at the low current densiy, the surface diffusion is a dominant factor for the shape evolution due to the high exchange current density of the reduction of Zincate ion, $Zn(OH)_4^{2-}$ [9,10]. Hence, the surface diffusion is regarded as the main factor for the Zn shape evolution at the low current density of Zn electrodeposition. Within the assumed events, an event at a number of the KMC step, k, was selected from all possible events with a probability R_k/R_{tot}, where R_k and R_{tot} denote the rate of event and the total rate of all possible events, respectively. As mentioned above, surface diffusion and deposition are included as the possible events for the KMC simulations. $R_{\mathrm{tot},k}$ is calculated as follows:

$$R_{\mathrm{tot},k} = R_{\mathrm{sur},k} + R_{\mathrm{dep}} \quad (2.2)$$

where $R_{sur,k}$, and R_{dep} are the surface diffusion rate in the *kth* KMC step and the deposition rate, respectively. The time increment of each KMC step is given by $\ln(u)/R_{tot,k}$. u denotes a uniform random number where u $\in$ [0,1).

Four types of surface diffusion were defined as a typical surface diffusion as same as the DFT calculation: i) surface diffusion on the pure (0001) surface, ii) flat surface diffusion on the pure (0−110) surface, iii) interlayer diffusion, and iv) edge diffusion. Their rates were determined for each direction in which the adatoms migrated. The adatoms diffuse within the lattice points aligning as the hcp structure in this KMC simulation because previous studies indicated that the layer-by-layer sturctures depositing before appearing the protrusion as the initial structure of the irregular shape evolution consists of the (0001) facets of the hcp-Zn [22,23,33]. In addition, although the existence of the screw dislocations can be considered from previous study related to the ZnO growth [34], it is not assumed in this simulation. In order to analyze the initial deposition of the layer-by-layer structures, hcp-Zn lattice can be suitable at the atomic scale. Hence, the deposition and surface diffusions on the (0001) surface is assumed. The simulation box are shown in the Figure 2.3 and 2.4, which are ordered as hcp Zn structures with lattice constants of a = 2.665 Å and c = 4.779 Å. The lattice constant of c was determined by the distance of the Zn layers of the slab model by DFT to model the surface relaxation at the solid-liquid interface. The lattice constant of a was the same as DFT since it is not affected by the surface relaxation. In addition, the activation energy of four surface diffusions on the substrate was set as the same on the deposited Zn layers during the deposition because the substrate and the deposited atom species are both Zn in this KMC simulation, which indicates that the interaction between the deposited atom on the substrate and that on the deposited layers are identical. Figure 2.5 shows the difference in the shape with the size of the x and y axes. The results are similar to each other. With respect to the calculation cost, 50 × 50 lattice points model is adopted. The periodic boundary condition which is periodically aligned condition that the atom going to the walls will appear the walls at the opposite sides, is not set in this simulation box.

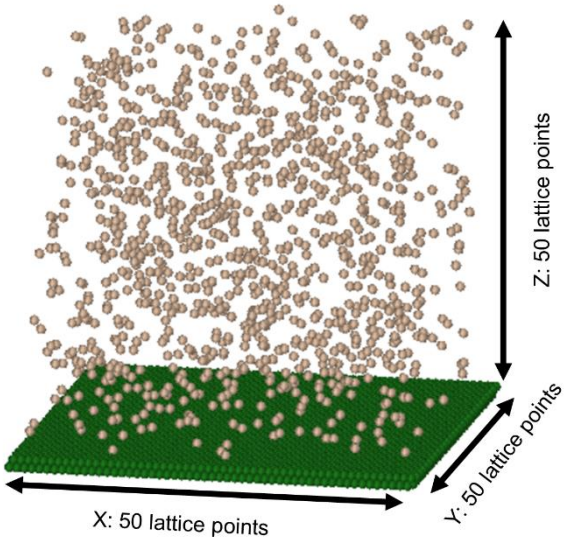

Figure 2.3. Cell box of the KMC program. Green layer shows the substrate of Zn(0001). Particles above the substrate show the Zn species in the solvent.

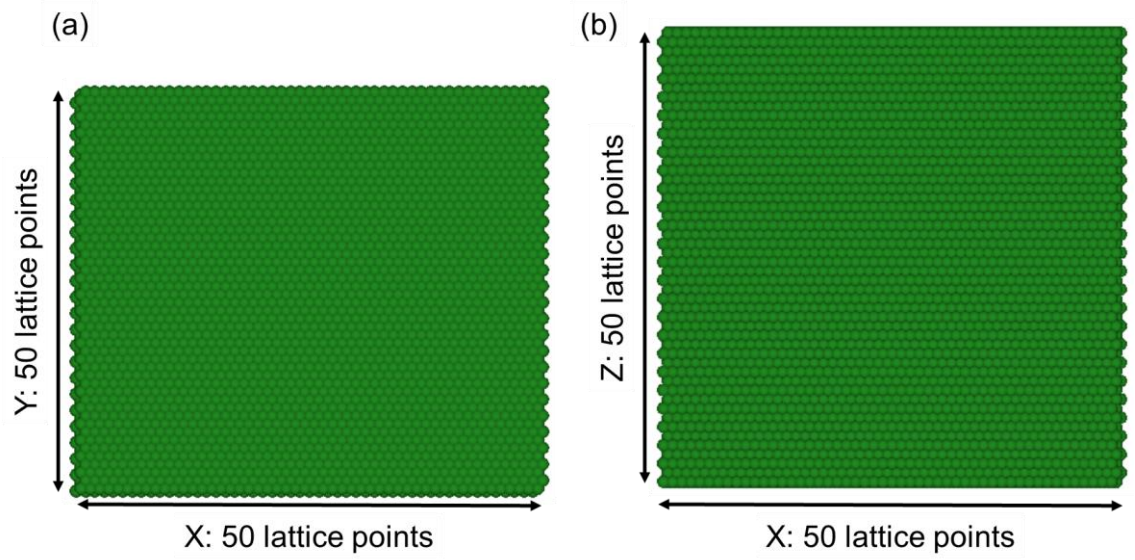

Figure 2.4. All lattice points of the simulation box corresponding to the hexagonal close-packed (hcp) structure. The lattice points are shown in green balls. (a) Top view of the box. The lattice constant of a = 2.665 Å is used in the simulation. (b) Side view of the box. The lattice constant of c = 4.779 Å is used in the simulation. Note that the length between the lattice points in the box are normalized for visualization.

The number of directions that Zn adatoms migrate was assigned with the number of nearest neighboring sites: six directions for the flat surface diffusion on the (0001)

surface, six for the (0−110) surface, and nine for the interlayer diffusion at the (0001) surface. The edge diffusion direction was included in six of the diffusions on the (0001) surface. Therefore, the number of nearest neighboring sites was 12, and there were nine possible sites of interlayer diffusion. The surface diffusion rate in the *kth* KMC step is described by the summation of the surface diffusion rates as follows:

$$R_{\mathrm{sur},k} = \sum_{i\in 21}\sum_{j\in N} D_0 \exp\left(-\frac{E_{\mathrm{a}_{i,j}}}{\mathrm{R}T}\right) \quad (2.3)$$

where i, j, and N are the direction number (the total number is twenty-one), the adatom number, and the total number of adatoms, respectively. D_0 is a pre-exponential factor, 10^{13} s^{-1} [35-37], $E_{ai,j}$ is the activation energy for each direction of surface diffusion, and R and T are the gas constant (8.31 J K^{-1} mol^{-1}) and temperature (298 K), respectively. Because the atom on the surface interacts with the other atoms on the surface such as the atoms consisting the surface and the deposited atoms [38], the activation energy, $E_{ai,j,}$ for i) on the (0001) surface and ii) on the (0−110) surface are functions of the bond number, n,

$$E_{\mathrm{a}_{i,j}} = \frac{E_{\mathrm{DFT}} \times l}{n} \quad (2.4)$$

where E_{DFT} is the activation energy calculated by DFT, l is the surrounded atom number, and n is 3 on the (0001) surface and 4 on the (0−110) surface, respectively, because the adatom is bonding with the three atoms of the (0001) surface and the four atoms of the (0−110) surface on each pure surface. Using this equation, the interactions of the surrounding adatoms is include in the activation energy approximately [38]. For instance, if the adatom is surrounded by a few atoms and interacted with them, the activation energy to break the bond with the adatoms will be too high to diffuse. In addition, if the nearest neighboring site was occupied or the adatom was present at the kink site, the surface diffusion rates of the adatom to these directions were assumed to be 0. The activation energy calculated by the equation (2.4) were utilized to estimate the surface diffusion rates in each direction except for the interlayer diffusion and the edge diffusion. The activation energy of the interlayer and edge diffusions were set as the values as calculated by DFT. The deposition reaction in this system is the reduction of $Zn(OH)_4^{2-}$. Previous study suggested that the OH species can smoothly detached from

the surface or the electron transfer step proceeds rapidly [9,39,40]. Hence, the pure Zn surface was assumed in this KMC simulation. In an electrochemical system, the deposition rate is controlled by changing the current density. Assuming a diffusion-limited condition, the deposition rate is described as a function of the current density as shown in an equation (2.5) [38]:

$$R_{\mathrm{dep}} = \frac{IS\mathrm{N_A}}{n\mathrm{F}} \quad (2.5)$$

where I, S, $\mathrm{N_A}$ n, and F are the current density (A cm^{-2}), the substrate area (Å^2 = 10^{-16} cm^2), the Avogadro constant (6.02×10^{23} mol^{-1}, the electron number participating in the reduction of $Zn(OH)_4^{2-}$, $Zn(OH)_4^{2-} + 2e^- \rightarrow Zn + 4OH^-$, and the Faraday constant (9.6485×10^4 C mol^{-1}). Once the deposition was chosen as an occurring event by a random number and the atom in the solution contacted with three atoms on the surface, deposition occurred and the atom in the solution appears as the adatom on the surface. Diffusion within the solution occurred $R_{\mathrm{bulk}}/R_{\mathrm{tot}}$ times at every KMC step. Because the diffusion within the solution is related to the diffusion coefficient of $Zn(OH)_4^{2-}$, R_{bulk} is calculated as follows:

$$R_{\mathrm{bulk}} = \frac{D_{\mathrm{Zn(OH)_4^{2-}}}}{AC} \quad (2.6)$$

where A and C are the lattice constants of the a- and c-axes, respectively, and $D_{\mathrm{Zn(OH)42-}}$ is the diffusion coefficient of $Zn(OH)_4^{2-}$, 2.0×10^{-6} cm^2 s^{-1}, that is estimated from the experiments [41]. The processes of the KMC simulation are described in the flowchart in Figure 2.6. Additionally, the adsorption behavior of the Zn precursor caused by the applied potential is not include in this KCM algorithm since it is considered that the effect of the applied potential can be negligible in the range of the small overpotential at the flat (0001) surface before the generation of the mossy structures, which appear at the small overpotential and initiate on the flat (0001) surface where the current density is not concentrated.

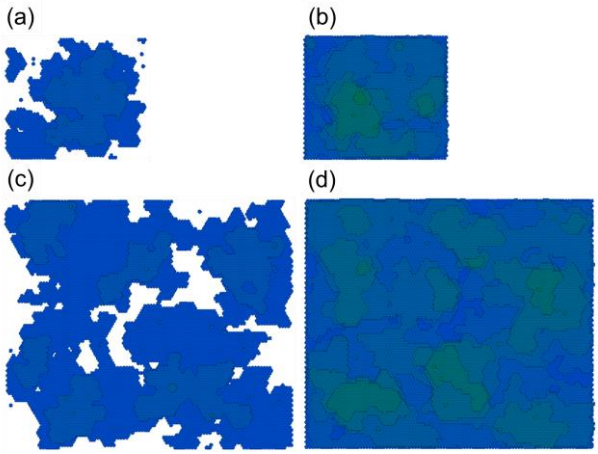

Figure 2.5. Test calculations for checking the effect of the cell size.
The size of the bottom is 50 × 50 lattice points: (a) 2,500 and (b) 7,500 atoms deposits.
The size is 100 × 100 lattice points: (c) 10,000 and 30,000 atoms deposits

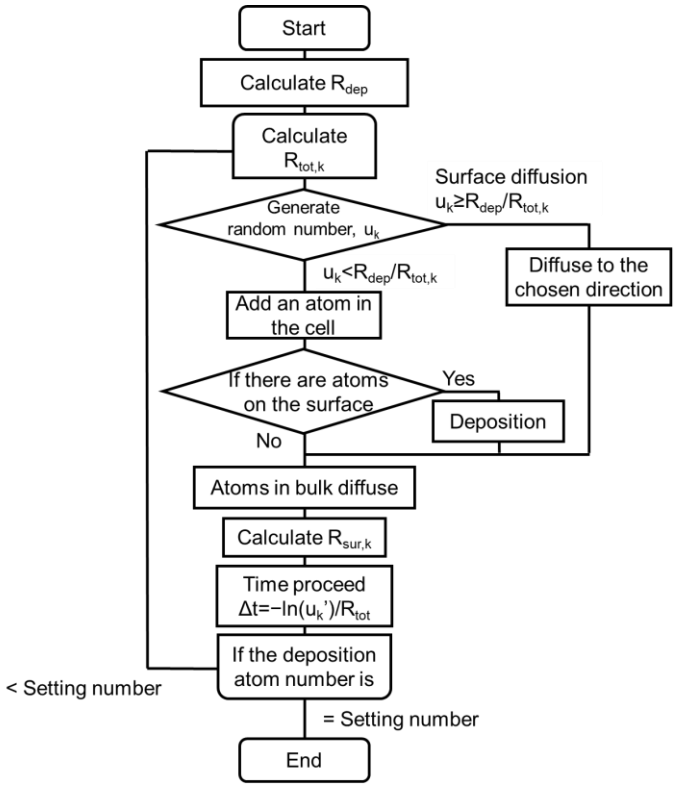

Figure 2.6. Flow chart of the KMC program.

2.3. Results and Discussion

2.3.1. Surface diffusion behavior of the Zn adatom on the Zn different facets

In the region of the small overpotential during the Zn electrodeposition, the surface diffusion is a dominant factor for the shape evolution due to the high exchange current density. This means that there is enough time for the Zn adatom to diffuse on the surface. In this section, the surface diffusion behavior of the Zn adatom is analyzed by DFT to obtain the activation energy of the diffusion. Figure 2.7 shows the potential curve of the surface diffusion of the Zn adatom on the (0001) surface. The activation energy of the pathway ($E_{a(0001)}$) is +14.1 kJ mol^{-1}, which is observed in the middle of the diffusion pathway. Because the shape of the diffusion surface is symmetrical, the potential curve is nearly symmetrical.

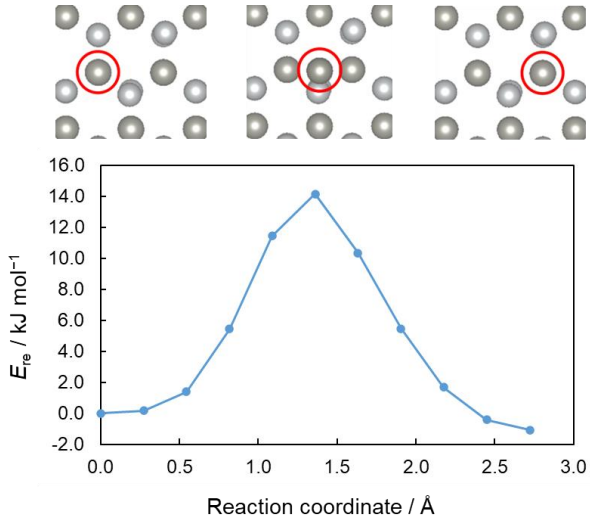

Figure 2.7. Potential curve of the Zn adatom surface diffusion on the Zn(0001) surface at the solid-liquid interface with 6.0 M KOH as an additive. Upper figures show the initial state, transition state, and final state from left to right. Red circle in each figure shows the position of the Zn adatom.

Figure 2.8 shows the potential curve of the diffusion of the Zn adatom on the (0−110) surface. The behavior is almost the same as the case on the (0001) surface, but the activation barrier of the surface diffusion on the (0−110) surface ($E_{a(0-110)}$) is +46.7 kJ mol^{-1}, which is higher than $E_{a(0001)}$. This may be due to the fact that the interaction between the surface and the Zn adatom is weaker on the (0001) surface than on the (0−110) surface due to the unique electronic state of Zn that is fully occupied 4s and 3d orbitals, which will be discussed in detail in Chapter 3. In addition to the characterisrics of the (0001) surface, the characteristics of the (0−110) surface can be also important because the barrier on the (0−110) surface is still higher than that on the (0001) surface. The coordination number difference is two on the (0−110) surface, which is calculated by the subtraction of two of the transition state from four of the initial state, whereas that is 1 on the (0001) surface. The structure of the transition state is shown in Figure 2.9.

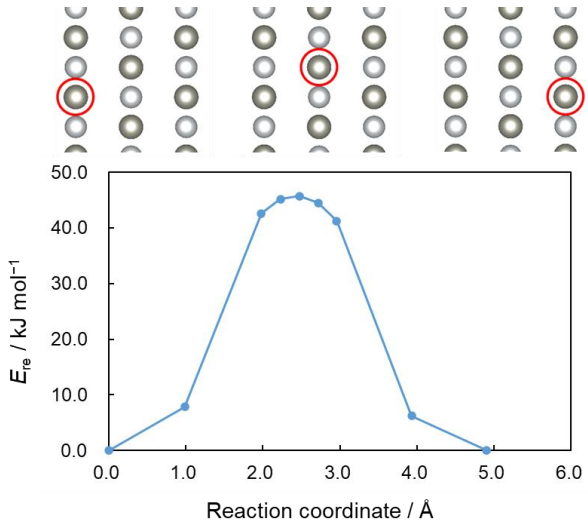

Figure 2.8. Potential curve of the Zn adatom surface diffusion on the Zn(0−110) surface at the solid-liquid interface with 6.0 M KOH as an additive. Upper figures show the initial state, transition state, and final state from left to right. Red circle in each figure shows the position of the Zn adatom.

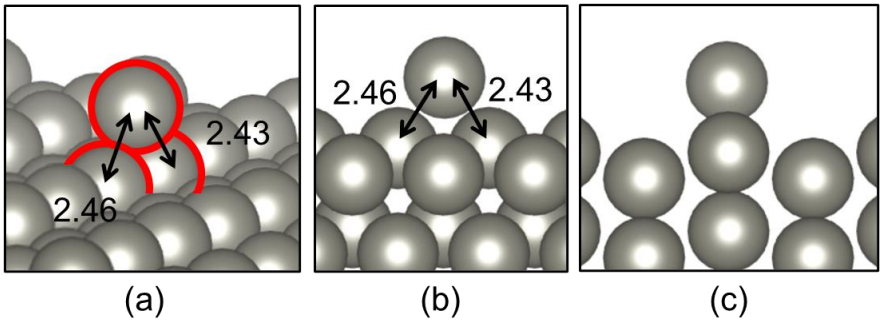

Figure 2.9. Structure of the transition state on the Zn(0−110) surface: (a) oblique view, (b) side view from the [0001] direction, and (c) side view along the [0001] direction. Red circle in (a) shows the Zn adatom for the clarity. Bond length are shown in unit of Å.

The structure of the (0−110) surface shows an uneven structure. Therefore, when an adsorbed atom jumps out of the concave area, not only the adsorbed atom but also the atoms on the surface are expected to be destabilized. This may have resulted in a larger difference in activation energy than expected from the difference in coordination number when compared to the (0001) surface. In addition, the surface energy of the (0−110) surface is higher than that of the (0001) surface [42], and the surface itself is unstable, suggesting that the instability of the atoms on the surface may contribute to the activation energy.

In addition, previous study examined the activation energy of the surface diffusion on W, Rh, and Ni obtained by the field ion microscope. Table 2.3 summarized the activation energies on the representative planes for each metal. Although the element is different, the order of the activation energy is in consistent with these results and the experimental values.

Table 2.3. Activation energy of the metals from the experiments. (Unit: kJ mol^{-1}) Coordinate number on surfaces indicates the number of the attached surface atoms with the adatom on a typical adsorption site. The number on the step edge structures such as (311), (331), and (321) is not defined here due to its several possibility.

	(111)	(110)	(100)	(311)	(331)	(211)	(321)	References
Coordinate number on surfaces	Fcc: 3 Bcc: 3	Fcc: 4 Bcc: 4	Fcc: 4			Bcc: 4		
Rh	15.1	58.2	84.5	51.9	61.9	-	-	[43]
W	171.5	83.7	-	-	-	51.5	78.7	[44]
Ni	31.8	30.9	60.8	28.9	43.4	-	-	[45]

Figure 2.10 shows the potential curve of the interlayer diffusion. In the interlayer, the pathway is started from the hollow hcp site of the upper layer and end at the nearest hollow hcp site of the lower layer to the edge. The hollow hcp sites in the lower layer are stable because the adatoms can interact with Zn atoms of the step-edge structure in addition to Zn atoms consisting the flat (0001) plane. Thus, the relative energy of the final state is lower than the initial state. The activation barrier for the interlayer diffusion is the ES barrier observed at the corners of the upper layer edges. This activation barrier (E_{itl}) is +29.1 kJ mol^{-1}, which is between the $E_{a(0001)}$ and $E_{a(0-110)}$, because it is considered that the edge region that the adatom migrates across reflects the physical characteristics of the (0−110) surface. Figure 2.11 shows the potential curve of edge diffusion, and the activation energy (E_{edge}) is +15.5 kJ mol^{-1}, which is similar to the activation energy on the (0001) surface. This similarity is due to the way that the edge diffusion works: it attaches the edge but remains on the (0001) surface, and the (0001) surface shows the dominant property for the surface diffusion. This also explains why the activation energy of these two diffusions is lower than that of the other diffusion.

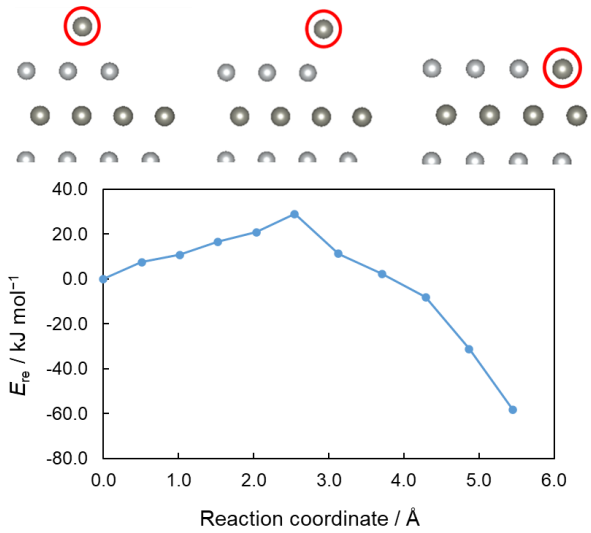

Figure 2.10. Potential curve of the Zn adatom interlayer diffusion on the Zn(0001) surface at the solid-liquid interface with 6.0 M KOH as an additive. Upper figures show the initial state, transition state, and final state from left to right. Red circle in each figure shows the position of the Zn adatom.

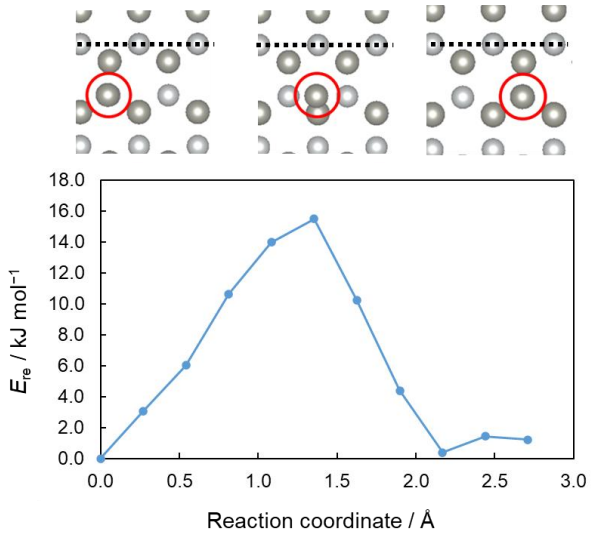

Figure 2.11. Potential curve of the Zn adatom edge diffusion on the Zn(0001) surface at the solid-liquid interface with 6.0 M KOH as an additive. Upper figures show the initial state, transition state, and final state from left to right. Black-dotted lines in the atomic figure show the end line of the terrace of the upper layer. Red circle in each figure shows the position of the Zn adatom.

The calculated activation energies for the surface diffusion in the (0001) plane are slightly lower than those estimated in the rigid sphere approximation for typical transition metals such as Cu and Ag [46,47]. This reveals several important properties of Zn: the isolated atoms of Zn occupy the s orbitals, while those of Cu, Ag and several other transition metals lack electrons in their outermost orbitals. This difference in the electronic state of the isolated atoms, even in systems where they exist as adatoms or surface constituent atoms, may lead to different interactions between adatom and surface atoms, resulting in their characteristic surface diffusivity. In particular, the adatoms may reflect the characteristics of isolated atoms, and their behavior with respect to the classical electron configuration can be discussed. To account for the differences in the electronic state of each atom, the surface diffusivity of Cu adatoms on the Cu surface was simulated in the same way: the Cu(111) surface is the densest plane in the fcc structure, which can be regarded as the equivalent plane to the Zn(0001) plane. The activation barrier of the surface diffusion of the Cu adatom on the Cu(111) surface is +31.0 kJ mol^{-1}, whose potential curve is shown in Figure 2.12(a). Hence, the flat surface diffusion on the Cu(111) surface is slower than that on Zn, indicating that Cu adatoms aggregate slowly on the (111) surface. The activation energy of the interlayer diffusion of Cu is +64.1 kJ mol^{-1} shown in Figure 2.12(b), and therefore both activation energies are higher than those of Zn. These differences may be attributed to differences in the electronic state of each element.[51] The electronic configuration of Zn is $3d^{10}4s^2$, which is fully occupied, whereas that of Cu is $3d^{10}4s^1$. In other words, the Zn surface weakly interacts with Zn adatoms, while the 4s orbital vacancies on the Cu surface may interact with Cu adatoms. This peculiar behavior of Zn surface diffusion may be important for irregular shape evolution, including irregular shape evolutions such as the mossy structures. These activation energies obtained by DFT were used to analyze the surface diffusion behavior of deposited adatoms during Zn electrodeposition for the KMC simulations.

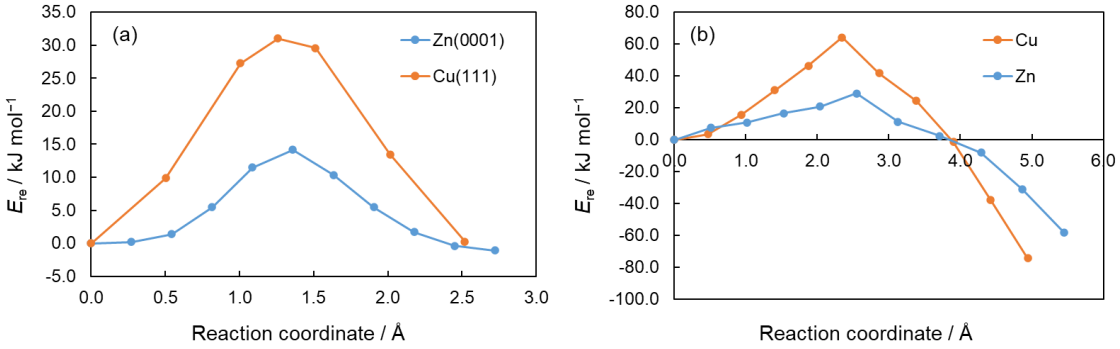

Figure 2.12. Comparison of the potential curves of Zn and Cu: (a) on Zn(0001) and on Cu(111), (b) interlayer diffusion. The orange line is the potential curve of the Cu cases. The Cu adatom diffused on Cu(111) from the hollow fcc site to the nearest neighbor hollow fcc site. In the interlayer diffusion, the Cu adatom diffused from the hollow fcc site on the upper layer to the nearest neighbor hollow fcc site on the lower layer. The blue lines in (a) and (b) show the same potential curve as the blue lines in Figure 2.7 and 2.10, respectively.

The solvent effect is involved in the adsorption of the Zn adatom and these diffusion mechanisms, and our RISM calculations clearly reveal its effect on adsorption and surface diffusion. The adsorption of the Zn adatom on the (0001) surface is calculated under the condition of 0.0 M or 6.0 M KOH solution. The adsorption energy (ΔE_{ad}) of the deposited Zn atom at the solid-gas and solid-liquid interfaces is shown in Table 2.2, which is calculated by the subtraction of the adsorption structure and the isolated system. The solvent effect should have a significant influence on the thermodynamics of adsorption, with Zn adsorption more favorable in the presence of water and KOH. This may be due to electrostatic interactions due to the strong electrolyte. It is assumed that a higher concentration of KOH than 6.0 M results in stronger adsorption. Table 2.3 shows the surface diffusion barriers in the absence of the modeled solvent. Compared to the activation energy of the surface diffusion in the presence of solvent, it can be seen that in the presence of solvent on the Zn surface, all activation energies except edge diffusion increase drastically. Thus, in this case, the effect of solvation is interfering with surface diffusion. This may be related to the interaction between the surface and solvent. When water molecules interact strongly with a surface, their removal is difficult. Under such conditions, water molecules on the surface interfere with the diffusion pathway of solvated Zn adatoms. In interlayer diffusion, the activation enegy is almost doubled by the solvation effect because the regions at the edges of the step where give the activation energy interact more strongly with water molecules, making displacement with the

moving Zn adatoms difficult.

Table 2.4. Adsorption energy of the deposited Zn atom on the (0001) surface ($\Delta E_{ad} = E_{adsorption\text{-}system} - E_{slab} - E_{isolated\text{-}Znatom}$). (Unit: kJ mol^{-1})

Gas	0.0 M KOH	6.0 M KOH
−118.5	−192.4	−294.5

Table 2.5. Activation energy at the solid-gas interface. (Unit: kJ mol^{-1})

	$E_{a(0001)}$	$E_{a(0-110)}$	E_{itl}	E_{edge}
Gas	+11.3	+34.7	+14.2	+22.6

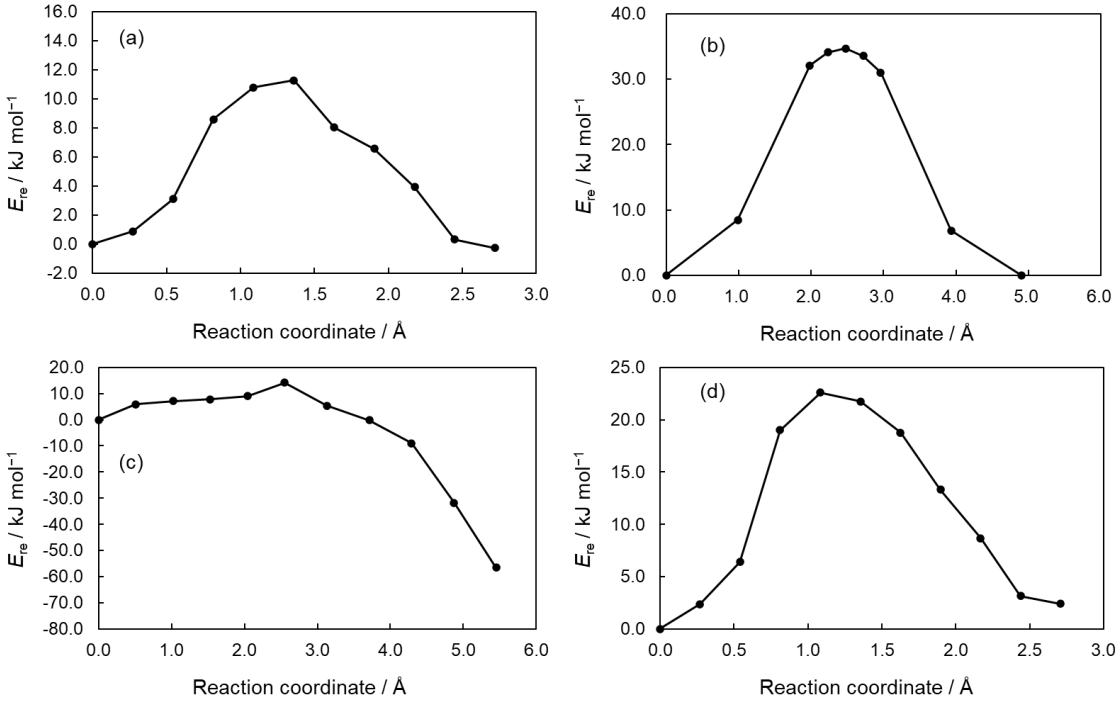

Figure 2.13. Potential curve of the Zn adatom surface diffusion at the solid-gas interface: (a) on the Zn(0001) surface at the solid-gas interface, (b) on the Zn(0−110) surface at the solid-gas interface, (c) interlayer diffusion on the Zn(0001) surface, and (d) edge diffusion on the Zn(0001) surface.

2.3.2. Nanoscale shape evolution of Zn at the initial stage of the irregular shape evolution

The KMC simulations of the Zn electrodeposition at the initial stage were performed to identify the cause of the layer-by-layer structures as the initial structures of the irregular shape evolution as part of the mesoscale analysis in this section. In this KMC simulation, following assumptions are included:

(i) The Zn precursor in the solution attaches from the random direction
(ii) The current density is enough low for adatoms to diffuse on the surface
(iii) The electron transfer is enough fast not to produce any adsorbates
(iv) The surface that deposition occurs is oriented to the pure (0001) facets
(v) The surface diffusion rate is defined by the activation energy
(vi) The activation energy is adjusted with respect to the number of the surrounding atoms

As for (i), the Zn precursor comes to the bulk solution and moves randomly to attach the surface. Since the mossy structures appear at the low current density, the supply of the precursor can be sufficient to attach the surface from every direction. As for (ii), the reaction limited condition which the layer-by-layer structures appear in experiments is assumed. This means that there is enough time for the Zn adatom to diffuse on the surface. The assumption (iii) is proposed by the previous study [9] that the exchange current density of the zincate ion is so high that this rest potential will differ only slightly (less than 1 mV) from the equilibrium zinc [48]. In addition, the phase diagram indicates the favorable state of this condition is pure Zn. Hence, the hydrogen adsorption and the residue of OH species or oxides on the Zn surface can be negligible [39,40]. As for (iv), since the mossy structures is considered to deposit on the (0001) surface [22,23,33], the substrate is assumed as the (0001) facets. In addition, the previous study indicates that the surface is fully reduced in the sufficiently negative potential [9,39,40]. The assumptions (v) and (vi) follows the previous study [38].

The scale of the DFT calculations as a multiscale analysis can be expanded Because our KMC model is constructed corresponding to our DFT model. By using the KMC simulations with DFT-calculated parameters, the crystal growth with respect to the

adatom behavior is analyzed. Table 2.4 shows $E_{a(0001)}$, $E_{a(0-110)}$, E_{itl}, and E_{edge}.

Table 2.4. Activation energy used in the KMC simulations to examine structural dependency on activation energies (Unit: kJ mol^{-1}).

	$E_{a(0001)}$	$E_{a(0-110)}$	E_{itl}	E_{edge}	Assumed conditions
(a)	+9.0	+76.7	+29.1	+15.5	Low $E_{a(0001)}$
(b)	+30.0	+76.7	+29.1	+15.5	High $E_{a(0001)}$
(c)	+14.1	+45.7	+29.1	+29.1	Low $E_{a(0-110)}$
(d)	+14.1	+76.7	+29.1	+20.0	High $E_{a(0-110)}$
(e)	+14.1	+76.7	+25.0	+15.5	Low E_{int}
(f)	+14.1	+76.7	+35.0	+15.5	High E_{int}
(g)	+14.1	+76.7	+29.1	+10.0	Low E_{edge}
(h)	+14.1	+76.7	+29.1	+20.0	High E_{edge}

First, in order to show the influence of each parameter, structural differences are observed when the activation energy is altered. Each activation energy was varied with lower and higher values than that of DFT to examine the dependency on each parameter. Figure 2.14 shows the typical structures when the effect caused by each parameter is clearly exhibited. $E_{a(0001)}$ is varied from +14.1 kJ mol^{-1} to +9.0 or +30.0 kJ mol^{-1}. $E_{a(0-110)}$ was set as +46.6 kJ kJ mol^{-1} and +76.6 kJ mol^{-1}. E_{itl} and E_{edge} are varied from +29.1 kJ mol^{-1} and +15.5 kJ mol^{-1} to +25.0 or +35.0 kJ mol^{-1} and to +10.0 or +20.0 kJ mol^{-1}, respectively. These are listed in rows (b)–(i) in Table 2.4. The influences of the diffusion rate on the (0001) surface, the (0−110) surface, interlayer, and edge diffusions are shown in Figures 2.13(a)–(b), (c)–(d), (e)–(f), and (g)–(i), respectively.

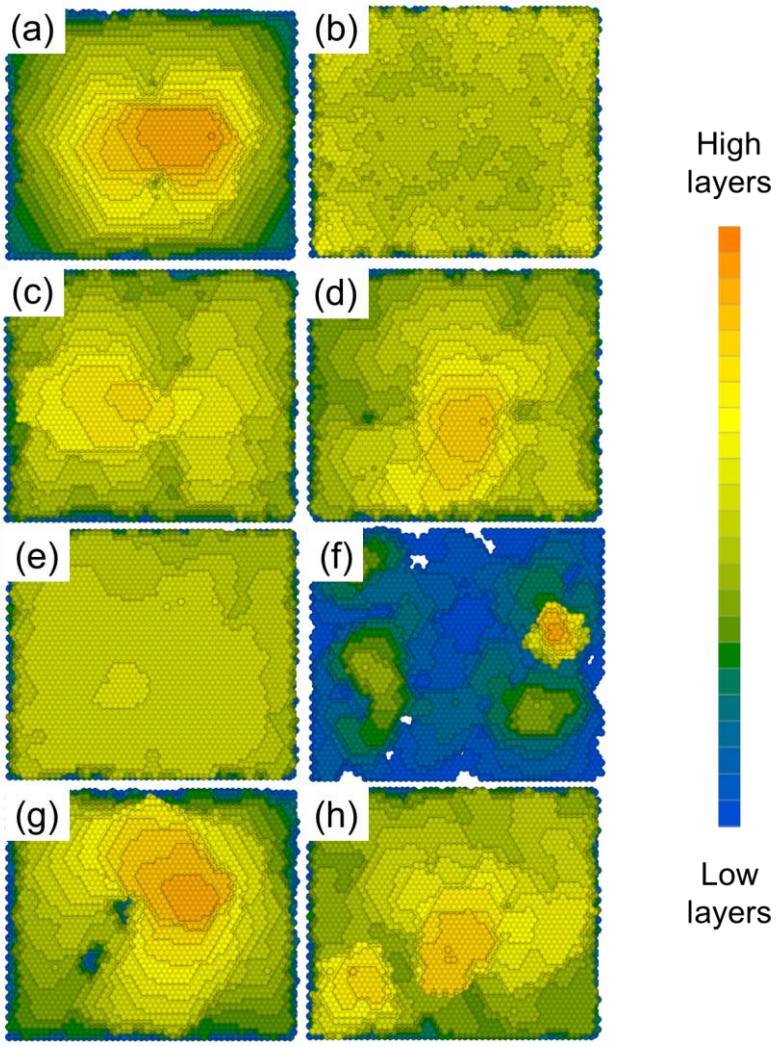

Figure 2.14. Snapshots of the Zn deposition on the Zn(0001) substrate with changing parameters. (a)-(c), (e), (f) are the deposition structures at 30,000 deposited atoms. (d) is the structure at 10,000 deposited atoms. The activation barriers for individual simulations were (a) $E_{a(0001)}$ = +9.0 kJ mol^{-1} (corresponding to row (a) in Table 2.4), (b) $E_{a(0001)}$ = +30.0 kJ mol^{-1} (corresponding to row (b) in Table 2.4), (c) $E_{a(0–110)}$ = +45.7 kJ mol^{-1} (corresponding to row (c) in Table 2.4), (i) $E_{a(0–110)}$ = +76.7 kJ mol^{-1} (corresponding to row (d) in Table 2.4), (e) E_{itl} = +25.0 kJ mol^{-1} (corresponding to row (e) in Table 2.4), (f) E_{itl} = +35.0 kJ mol^{-1} (corresponding to row (f) in Table 2.4), (g) E_{edge} = +10.0 kJ mol^{-1} (corresponding to row (g) in Table 2.4), (h) E_{edge} = +20.0 kJ mol^{-1} (corresponding to row (h) in Table 2.4).

As shown in Figures 2.14(a) and (b), the simulation of the more rapid diffusion on the (0001) surface results in a clearly hexagonal structure. Conversely, on the (0001) plane, small random deposits are formed because the adatoms cannot aggregate due to slow diffusion. Figures 2.14(c) and (d) shows the effect of $E_{a(0-110)}$. There are little change with these values. $E_{a(0-110)}$ indicates the diffusion rates of adatoms on the side walls of the well-developed deposits. Deposition at the initial stage does not yield high deposits with large side walls. Hence, the drastic change was not observed. With different E_{itl} parameters that is the ES barrier, as shown in Figures 2.14(e) and (f), the size of the island varies. The low E_{itl} leads to a larger island structure and smoother growth on the (0001) surface, whereas a high E_{itl} causes a larger number of steps even at 10,000 deposited atoms. Furthermore, the diameter of the island at high E_{itl} is smaller than that at low E_{itl}. Therefore, adatoms with high interlayer diffusivity are more likely to step down and form islands of large area. This trend is also consistent with previous studies that have found findings on 3D mound formation [7]. This result indicates that the ES barrier is a key parameter for the formation of layer-by-layer structures. Although the activation energies of the interlayer diffusion were altered from +25.0 kJ mol^{-1} to +35.0 kJ mol^{-1}, the values of the ES barrier generating the layer-by-layer structures should be different with respect to the values of the activation energies of the other surface diffusions. Figures 2.14(g) and (h) suggest that edge diffusion may be the dominant factor in determining the 2D shape of the island. Rapid diffusion in this step traps adatoms at stable sites and produces distinct hexagonal deposits. On the other hand, even with slow edge diffusion, layer-by-layer structure is observed, but the 2D structure of the islands shows an ambiguous shape.

These trends provide the characteristics of each parameter. By using the activation energies obtained by DFT, the specific behavior of the Zn shape evolution is observed. Figure 2.15 shows snapshots of the KMC simulation using the parameters listed in row (c) of Table 2.4. At 1000 deposited atoms, which shows a few atomic layer depositions on the Zn(0001) surface within 10^{-6} s, a hexagonal 2D nucleation is observed. As deposition proceeds, the deposits forms layer-by-layer shape evolution, unlike formation of randomly distributed small dots. At 10,000 deposited atoms, which corresponds to a nano-sized, hexagonal grain, an island starts to appear. Observation of hexagonal island growth on the Zn(0001) surface shows that the area of the top layer becomes smaller with

30,000 to 40,000 deposited atoms. This structure deposits within about 10^{-4} s. The width of these layer-by-layer structures is about 10 nm. The relationship between each diffusion rate is important in this behavior, in which the interlayer diffusion rate is relatively small. This rate indicates that the adatoms generally do not step down to the lower layers, resulting in a mountainous shape.

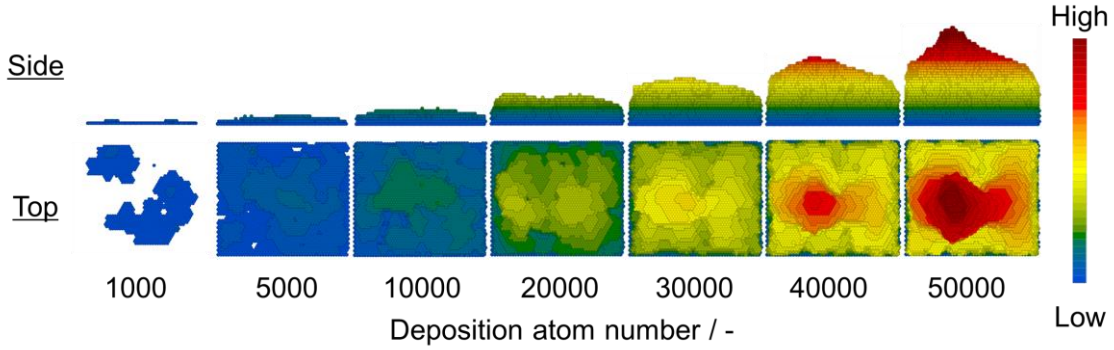

Figure 2.15. Snapshots of the Zn deposition on the Zn(0001) substrate. Surface diffusion rates were derived from DFT in the conditions of solid-liquid interface.

The comparison of Figures 2.14 and 2.15 yields insight into the specific behavior of Zn compared to that of Cu, with the difference in s-orbitals and Cu not forming mossy structures. Since Cu shows the similar electronic state with Zn, the difference of the shape evolution can be discussed with respect to the electronic state. Based on the activation barrier (+31.0 kJ mol^{-1}, Figure 2.12), the flat surface diffusion on the Cu(111) surface somehow corresponds to the case shown in Figure 2.14(b). Although this simulation assumes the hcp structure and is not directly applicable to Cu, it is possible to give an insight qualitatively for the activation energy difference of Zn from the Cu(111) surface. It is expected that small random deposits are more likely to occur on the Cu surface than in a layer-by-layer structure. Furthermore, with respect to the activation energy of the interlayer diffusion between Zn and Cu, island growth of Zn deposits should exhibit a larger diameter than that of Cu deposits. Therefore, Zn metal forms 2D layer-by-layer structures more readily than Cu. This 2D layer-by-layer structure should result in the formation of prominent and irregular deposits of Zn.

These multi-scale simulations revealed the behavior of the Zn shape evolution during the initial stage of Zn electrodeposition. Initially, a 2D nucleation structure

appeared on the (0001) surface. As deposition proceeded, a hexagonal layer-by-layer structure was formed. Although such 2D nucleation behavior was suggested at the micrometer scale in previous studies, this multiscale analysis made it possible to observe the layer-by-layer structure even at the nanoscale and to examine its relationship to the crystal growth and behavior of Zn adatoms. These 2D growth originated from the modest rates of flat surface diffusion on the (0001) surface. Gradually, the hexagonal structure grows slowly and shrunk the top layer of the layer-by-layer structures because the interlayer diffusion of Zn is relatively slow, resulting in a mountain-like structure within 10 nm. These multiscale simulations suggest that the activation energy, which reflects the electronic state of Zn, is a dominant factor for the shape evolution, causing submicrometer layer-by-layer structures, which can be seen under the mossy structures. The relatively low activation energy of the surface diffusion on the Zn(0001) surface was due to its weak bond with the surface, owing to the electronic state of Zn $3d^{10}4s^2$. These DFT and KMC results discussed the mechanism of the sub-micrometer structure evolution from the viewpoint of the influence of the electronic state of Zn. For detailed analysis of the electronic state, the density of state of Zn surfaces will be analyzed in Chapter 3.

As mentioned above, the experimental results of Zn alkaline electrodeposition suggest that these layer-by-layer structures consists of the (0001) planes [22,23,33]. This is consistent with the layer-by-layer structures of the (0001) planes obtained in the simulations. The results indicated that the atomic-level mechanism proposed in these multiscale simulations is qualitatively consistent with the experimentally observed behavior. Thus, the multiscale simulation supports the experimental hypothesis.

The initial structure of the KMC substrate may also affect the simulated deposition structures. Since previous studies have shown that mossy structures originate from the (0001) surface, a model with a perfectly flat surface (0001) is assumed in this study [22,23,33] as mentioned above. Rough substrate surfaces with atomically stepped or mounded structures are more likely to form layer-by-layer structures than atomically flat surfaces. Furthermore, as structures consisting of several adatoms on the surface aggregate, the area of the flat (0001) surface is considered to become smaller and the space for flat surface diffusion of Zn adatoms becomes narrower. Therefore, though this atomically rough surface may not be observed as often in Zn electrodeposition, the

structure may be different from that of this study.

2.3.3. Hypothesis of the further growth mechanism of Zn from the viewpoint of the simulation of the initial stage

The deposition behavior of the layer-by-layer structures as the initial deposition was able to reproduce it and its mechanism was analyzed. Although the layer-by-layer structures within the 10 nm × 10 nm area was confirmed in this KMC simulation, it is difficult to reproduce the protrusion with this simulation because the area of deposition is approximately 10 μm × 10 μm. This is because it is necessary to construct a large-area simulation that fully incorporates the behavior of defects and solvent species. Therefore, here hypotheses about the growth mechanism from the prtrusion to the elongation of the mossy structure after the lalyer-by-layer structures, and how to verify the hypothesis are discussed.

As mentioned, mossy structures show nanofilamentuos strucures. The previous studies have investigated the mechanism of such deposits that have high aspect ratio. In vapor-phase growth, the vapor-liquid-solid mechanism is known [49]. This method is based on a mechanism in which droplets of deposited alloys appear on the substrate surface, and deposits appear at the bottom of the droplets through the interior of the droplets. This is often seen as a fabrication method for whiskers and nanowires. Several mechanisms of the deposition is explained in this connection: a mechanism in which a bubble exists at the tip and growth of the main deposits proceeds [50], the other mechanism in which In nuclei are fabricated on the substrate and Ge nanowires are formed through the nuclei of In by electrodeposition [51], and a hypothesized mechanism in which a cloud of hydroxide is formed at the tip of Zn-Ni when Zn-Ni alloy becomes a whisker in electrodeposition [52]. Another possible mechanism is growth by screw dislocations, which is often observed in ZnO, a system similar to Zn [34].

Considering the above previous studies, the presence of hydroxides in this system, and the deposition of the layer-by-layer structures, the aggregation of hydroxide species and screw dislocation are considered as the active sites. To verify the presence or absence of screw dislocations, transmission electron microscopy is useful to check for the

presence of screw dislocations around the mid-axis as shown in the previous study [34]. On the other hand, the former is difficult to verify. Species that may be present on the surface can be OH^- and adsorbed species of ZnOH, which are assumed to escape from the surface sufficiently rapidly in this simulation. Modelling the surface in the presence of such adsorbed species and analyzing the reaction mechanism using first-principles calculations may be the first step toward understanding. Based on the results obtained in this study, it is assumed that the (0001) surface and step-terrace in the layer-by-layer structures will be exposed to the interface. Hence, it is important to model these surfaces, and it is necessary to verify the reactivity of each surface with such adsorbates. In addition, the growth of the layer-by-layer structures suggest that if the activation energy of surface diffusion can partially change on the certain point, the aspect ratio of the layer-by-layer structures may be different from that of the deposited layer-by-layer structures earlier during the electrodeposition. If it elongates, this may result in a protrusion. In the case of its elongation, a concentration of current around this structure may result in deposition and elongation only in that area.

From the above points, it is hypothesized that the mossy structure appears when there are many reactants and some active sites appear on the layer-by-layer structures. Disrupting the ratio of these phenomena is expected to lead to the suppression of the mossy structures. One method is to increase the reactivity by increasing the number of active sites. By increasing the number of the active sites, the precursor is not consumed in one part of the surface but in larger area that exists many active sites. Hence, it is expected that the deposit will not grow in one part of the active site, as assumed in the case of the mossy structure. In addition, the mechanism based on the behavior of the surface diffusion of adatoms can be proposed to change the morphology at the initial stage according to the simulation results. The substrate surface is coated in advance with a film that allows Zn to permeate to adjust an environment where surface diffusion of adsorbed Zn atoms is difficult to occur freely. This may be possible to change the layer-by-layer structures.

Conclusions

In this chapter, the multiscale simulation analyzed the irregular shape evolution during the initial stage of Zn electrodeposition, explaining the atomic-level phenomena using DFT calculations and the mesoscale phenomena using KMC simulations. The multiscale simulations proposed the mechanism of shape evolution: the 2D nucleation and island growth is observed on the (0001) surface and forms mountain-like structures, with shrunk upper layers. This leads to the formation of the layer-by-layer strctures as the initial structure of the irregular shape evolution. In addition, the analysis revealed that the evolution of the layer-by-layer structures is due to the specific surface diffusion behavior of Zn. In particular, DFT calculations reveal that rapid surface diffusion and slow interlayer diffusion of Zn adatoms on the (0001) plane are important for Zn shape evolution. It can be concluded that the behavior of Zn adatoms during electrodeposition must be controlled in order to control Zn shape evolution. The surface diffusion rate is derived from the electronic state of Zn and the solvation structure on the Zn surface, indicating that the electronic state and solvation structure of the surface where the Zn adatoms are located may affect the surface diffusion behavior. These results, which are difficult to obtain using only conventional experimental methods for electrodeposition processes, provide valuable insight into the development of electrodeposition conditions to suppress irregular shape evolution. This analysis will be useful for understanding the electrodeposition process from an atomic point of view.

References

[1] W. Mehl, J. O'M Bockris, Mechanism of Electrolytic Silver Deposition and Dissolution, *J. Chem. Phys.* 27 (1957) 818.

[2] W. Mehl, J. O'M Bockris, On the Mechanism of Electrolytic Deposition and Dissolution of Silver, *Can. J. Chem.* 37 (1959) 190-204.

[3] Y. Onabuta, M. Kunimoto, H. Nakai, T. Homma, First-Principle Study of the Oxidation Mechanism of Formaldehyde and Hypophosphite for Copper and Nickel Electroless Deposition Process, *Electrochim. Acta* 307 (2019) 536-542.

[4] M. Kunimoto, K. Endo, H. Nakai, T. Homma, Acceleration Effect of Thiourea on the Oxidation Reaction of Hypophosphite Ion on Ni Surface, *Electrochim. Acta* 100 (2013) 311-316.

[5] K. Iokibe, K. Azumi, H. Tachikawa, Surface Diffusion of a Zn Adatom on a Zn(001) Surface: A DFT Study, *J. Phys. Chem. C* 111 (2007) 13510-13516.

[6] X. Hao, R. Zhang, L. Ling, B. Wang, Insight into the Diffusion Mechanism of Cu Cluster over Cu(111) Surface: Effect of Syngas and H_2S Atmosphere on Cu Diffusion, *Chem. Phys.* 522 (2019) 24-31.

[7] J. W. Evans, P. A. Thiel, M. C. Bartelt, Morphological Evolution During Epitaxial Thin Film Growth: Formation of 2D Island and 3D Mounds, *Sur. Sci. Rep.* 61 (2006) 1-128.

[8] X. Li, O. T. Drews, E. Rusli, F. Xue, Y. He, R. Braatz, R. Alkire, Effect of Additives on Shape Evolution During Electrodeposition I. Multiscale Simulation with Dynamically Coupled Kinetic Monte Carlo and Moving-Boundary Finite-Volume Codes, *J. Electrochem. Soc.* 154 (2007) D230-D240.

[9] J. O'M Bockris, Z. Nagy, A. Damjanovic, On the Deposition and Dissolution of Zinc in Alkaline Solutions, *J. Electrochem. Soc.* 119 (1972) 285-295.

[10] J. Bressan, R. Wiart, Inhibited Zinc Electrodeposition: Electrode Kinetics and Deposit Morphology, *J. Appl. Electrochem.* 9 (1979) 43-53.

[11] M. Otani, O. Sugino, First-Principles Calculations of Charged Surfaces and Interfaces: A Plane-Wave Nonrepeated Slab Approach, *Phys. Rev. B* 73 (2006) 115407.

[12] F. Hirata, P. J. Rossky, An Extended RISM Equation for Molecular Polar Fluids, *Chem. Phys. Lett.* 83 (1981) 329-334.

[13] P. Giannozzi, S. Baroni, N. Bonini, M. Calandra, R. Car, C. Cavazzoni, D. Ceresoli, G. L. Chiarotti, M. Cococcioni, I. Dabo et al., QUANTUM ESPRESSO: a Modular and Open-Source Software Project for Quantum Simulations of Materials, *J. Phys.: Condens. Mater.* 21 (2009) 395502.

[14] P. Giannozzi, O. Andreussi, T. Brumme, O. Bunau, M. B. Nardelli, M. Calandra, R. Car, C. Cavazzoni, D. Ceresoli, M. Cococcioni et al., Advanced Capabilities for Materials Modeling with QUANTUM ESPRESSO, *J. Phys.: Condens. Matter* 29 (2017) 465901.

[15] S. Nishihara, M. Otani, Hybrid Solvation Models for Bulk, Interface, and Membrane: Reference Interaction Site Methods Coupled with Density Functional Theory, *Phys. Rev. B* 96 (2017) 115429.

[16] W. Kohn, L. J. Sham, Self-Consistent Equations Including Exchange and Correlation Effects, *Phys. Rev.* 140 (1965) A1133-A1138.

[17] D. Vanderbilt, Soft Self-Consistent Pseudopotentials in a Generalized Eigenvalue Formalism, *Phys. Rev. B* 41 (1990) 7892-7895.

[18] A. M. Rappe, K. M. Rabe, E. Kaxiras, J. D. Joannopoulos, Optimized Pseudopotentials, *Phys. Rev. B* 41 (1990) 1227-1230.

[19] J. P. Perdew, K. Burke, M. Ernzerhof, Generalized Gradient Approximation Made Simple, *Phys. Rev. Lett.* 77 (1996) 3865-3868.

[20] H. J. Monkhorst, J. D. Pack, Special Points for Brillouin-Zone Integrations, *Phys. Rev. B* 13 (1976) 5188-5192.

[21] J. Haruyama, T. Ikeshoji, M. Otani, Electrode potential from density functional theory calculations combined with implicit solvation theory, *Phys. Rev. Mater.* 2 (2018) 095801.

[22] T. Otani, M. Nagata, Y. Fukunaka, T. Homma, Morphological Evolution of Mossy Structures during the Electrodeposition of Zinc from an Alkaline Zincate Solution, *Electrochim. Acta* 206 (2016) 366-373.

[23] T. Otani, Y. Fukunaka, T. Homma, Effect of Lead and Tin Additives on Surface Morphology Evolution of Electrodeposited Zinc, *Electrochim. Acta* 242 (2017) 364-372.

[24] K. Kovalenko, F. Hirata, Self-Consistent Description of a Metal-Water Interface by the Kohn-Sham Density Functional Theory and the Three-Dimensional Reference Interaction Site Model, *J. Chem. Phys.* 110 (1999) 10095-10112.

[25] H. J. C. Berendsen, J. P. M. Postma, W. F. von Gunstaren, J. Hermans, Interaction Models for Water in Relation to Protein Hydration, *In Intermolecular Forces, B. Pullman, Ed., Dordrecht Reidel Publishing company, Holland* (1981) pp 331-342.

[26] W. L. Jorgensen, J. Tirado-Rives, The OPLS Potential Functions for Proteins. Energy Minimizations for Crystals of Cyclic Peptides and Crambin, *J. Am. Chem. Soc.* 110 (1988) 1657-1666.

[27] W. L. Jorgensen, D. S. Maxwell, J. Tirado-Rives, Development and Testing of the OPLS All-Atom Force Field on Conformational Energetics and Properties of Organic Liquids, *J. Am. Chem. Soc.* 118 (1996) 11225-11236.

[28] L. Hu, U. Ryde, Comparison of Methods to Obtain Force-Field Parameters for Metal Sites, *J. Chem. Theory Comput.* 7 (2011) 2452-2463.

[29] A. K. Rappé, C. J. Caseqit, K. S. Colwell, W. A. Goddard III, W. M. Skiff, UFF, a Full Periodic Table Force Field for Molecular Mechanics and Molecular Dynamics Simulations, *J. Am. Chem. Soc.* 114 (1992) 10024-10035.

[30] G. Ehrlich, F. G. Hudda, Atomic View of Surface Self-Diffusion: Tungsten on Tungsten, *J. Chem. Phys.* 44 (1966) 1039-1049.

[31] R. L. Schwoebel, E. J. Shipsey, Step motion on Crystal Surfaces, *J. Appl. Phys.* 37 (1966) 3682-3686.

[32] A. B. Bortz, M. H. Kalos, J. L. Lebowitz, A New Algorithm for Monte Carlo Simulations of Ising Spin Systems, *J. Comput. Phys.* 17 (1975) 10-18.

[33] T. Mitsuhashi, Y. Ito, Y. Takeuchi, S. Harada, T. Ujihara, Non-Uniform Electrodeposition of Zinc on the (0001) Plane, *Thin Solid Films* 590 (2015) 207-213.

[34] S. A. Morin, M. J. Bierman, J. Tong, S. Jin, Mechanism and Kinetics of Spontaneous Nanotube Growth Drivenby Screw Dislocations, *Science* 328 (2010) 476-480.

[35] P. Xiao, G. Henkelman, Kinetic Monte Carlo Study of Li Intercalation in $LiFePO_4$, *ACS Nano* 12 (2018) 844-851.

[36] G. H. Vineyard, Frequency Factors and Isotope Effects in Solid State Rate Processes, *J. Phys. Chem. Solids* 3 (1957) 121-127.

[37] A. C. Levi, M. Kotla, Theory and Simulation of Crystal Growth, *Condens. Matter* 9 (1997) 299-344.

[38] R. M. Stephens, R. C. Alkire, Simulation of Kinetically Limited Nucleation and

Growth at Monatomic Step Edges, *J. Electrochem. Soc.* 154 (2007) D418-D426.

[39] C. Cachet, B. Soïdani, R. Wiart, The Behavior of Zinc Electrode in Alkaline Electrolytes I. A Kinetic Analysis of Cathodic Deposition, *J. Electrochem. Soc.* 138 (1991) 678-687.

[40] Y.-C. Chiu, M. A. Genshaw, A Study of Anion Adsorption on Platinum by Ellipsometry, *J. Pjys. Chem.* 73 (1969) 3571-3577.

[41] E. Deiss, F. Holzer, O. Haas, Modeling of an Electrically Rechargeable Alkaline Zn-Air Battery, *Electrochim. Acta* 47 (2002) 3995-4010.

[42] L. Kabalan, I. Kowalec, C. R. A. Catlow, A. J. Logsdail, A computational study of the properties of low- and high-index Pd, Cu and Zn surfaces, *PCCP* 23 (2021) 14649

[43] G. Ayrault, G. Ehrlich, Surface Self-diffision on an Fcc Crystal: An Atomic View, *J. Phys. Chem.* 60 (1974) 281-294.

[44] W. R. Graham, G. Ehrlich, Surface Self-diffusion of Single Atoms, *Thin Solid Films*, 25 (1975) 85-96.

[45] R. T. Tung, W. R. Graham, Single Atom Self-diffusion on Nickel Surfaces, *Surf. Sci.* 97 (1980) 73-87.

[46] B. E. Conway, J. O'M. Bockris, On the Calculation of Potential Energy Profile Diagrams for Processes in Electrolytic Metal Deposition, *Electrochim. Acta* 3 (1961) 340-366.

[47] B. E. Conway, J. O'M. Bockris, The Mechanism of Electrolytic Metal Deposition, *Proc. Roy. Soc.* A248 (1958) 394-403.

[48] J. O'M. Bockris, Modern Aspects of Electrochemistry, *No. 1, chap. 4, J. O'M. Bockris, B. E. Conway, Editors, Butterworths, London* (1954).

[49] H. Anzai, T. Takahashi, M. Suzuki, M. Kanai, G. Zhang, T. Hosomi, T. Seki, K. Nagashima, N. Shibata, T. Yanagida, Unusual Oxygen Partial Pressure Dependence of Electrical Transport of Single-Crystalline Metal Oxide Nanowires Grown by the Vapor−Liquid−Solid Process, *Nano Lett.* 19 (2019) 1675-1681.

[50] T. Yashima, M. Tani, R. Kurita, Filamentous Crystal Growth in Organic Liquids and Selection of Crystal Morphology, *Sci. Rep.* 12 (2022) 9946.

[51] N. K. Mahenderkar, Y.-C. Liu, J. A. Koza, J. A. Switzer, Electrodeposited Germanium Nanowires, *ACS Nano* 8 (2014) 9525-9530.

[52] K. Kamei, H. Yumoto, Electrodeposition of Zn-Ni Alloy Whisker, *J. Japan Inst.*

Metals 57 (1993) 1227-1234.

Chapter 3:

Surface Electronic State of Zn during Surface Diffusion

3.1. Introduction

In Chapter 2, the mechanism of the Zn shape evolution with respect to the atomic viewpoint was elucidated. The multiscale simulation comprising density functional theory (DFT) and kinetic Monte Carlo (KMC) simulations proposed the mechanism of the layer-by-layer structure of the Zn deposits in the nanometer scale. DFT analyzed the surface diffusion of Zn adatoms on the Zn facets, suggesting that the Zn adatoms diffuse more rapidly on the flat (0001) surface than the interlayer diffusion that is the diffusion downward from the upper layer to the lower layer of the (0001) surface. This specific behavior of the Zn adatom on the surface is a dominant factor for the Zn shape evolution according to the KMC simulations using the activation energy calculated by DFT. In order to avoid the layer-by-layer structures, the control of the surface diffusion rates may be significant. For this control, further understanding of the origin of the surface diffusion behavior will be inevitable. The atomic behavior of elements may be attributed to the electronic state of the adsorbates and the surface. Since the balance of the surface diffusion rates can be intrinsic to elements [1,2], the electronic state of each element may play an important role. Hence, analysis of the electronic state of the Zn adatom and the surface will be helpful. In particular, the low activation energy of the surface diffusion can be caused by the weak interaction of the adatoms and surfaces, which may be related to the electronic state of the element. Zn has an electronic configuration of $3d^{10}4s^2$. This fully occupied state may exhibit the specific behavior of the Zn adatom on the surface.

Hence, this chapter focused on the change of the electronic state during the surface diffusion of the Zn adatom by the analysis of the local density of state (LDOS) using the DFT calculation. Before the analysis of the electronic state, the surface diffusion behavior in the condition with the applied potential is analyzed at the solid-liquid interface. ESM-RISM calculation can treat the electrochemical interface by adjusting the applied potential with respect to considered reference electrodes. This method includes information of the electronic state under the applied potential condition, which is usually difficult to analyze. Even though the surface diffusion is not a charge transfer process, the local electrolyte distribution may be changed by the applied potential, which shows a

possibility to change the behavior. After the analysis of the effect of the applied potential, the intrinsic behavior of Zn is analyzed by LDOS. To rationalize the characteristics of Zn with respect to the viewpoint of the period table, LDOS of the Cu surface is compared because Cu is next to Zn in the periodic table with $3d^{10}4s^{1}$ and shows no mossy structures in experiments [3,4]. Elucidating the importance of the electronic state for the balance of the surface diffusion rates will provide valuable insight for understanding the electrodeposition with respect to the atomistic viewpoint.

3.2. Methods

Basically, the conditions of the DFT calculation in this chapter are same as the Chapter 2. Quantum ESPRESSO package was used for all DFT calculations of the structural optimization and LDOS projection [7,8]. The Brillouin zone was sampled by Monkhorst-Pack k-points grid [9] with 1 × 1 × 1 for the structural optimizations and 10 × 10 × 1 for the LDOS calculations. The LDOS was calculated by the projection of the wave function onto orthogonalized atomic wavefunctions. For the analysis of the electronic state of the surface, the summation of the LDOS of the atoms of the surface that interacts with the adatom was calculated. The LDOSs of the isolated atom and slab were calculated by putting the atom sufficiently above the surface so as not to interact with each other.

Effective screening medium (ESM) with reference interaction site model (RISM) was utilized to reproduce the electrochemical interface including the applied potential [10]. The electrolyte condition was set as 6.0 M KOH solution to maintain the alkaline conditions as same as the previous chapter and experiments [3,4,11]. The other conditions are also same as the previous sections.

The structures of the surface models are the same as the previous chapter. The (0001) surface and the step-edge model of the Zn slab and the Cu(111) slab were utilized for the LDOS calculations. Super cell of the hexagonal close packed (hcp) - Zn(0001) surface was constructed as 4 × 4 × 4 slab models with 64 atoms. A supercell of the face-centered

cubic (fcc) - Cu(111) surface was also constructed as the same slab model for the comparison of Zn. In addition, a step-terrace structure model was constructed where Ehrlich-Schwoebel (ES) barrier [12,13] can be observed.

In order to consider the effect of the applied potential for the surface diffusion, the constant-N method was used. The electron number of the system was changed and the grand potential, Ω, which is defined in previous study [10], was calculated to compare the system that has the different number of electrons as follows.

$$\Omega = A - \mu_e(N_e - N_e^0) \tag{3.1}$$

$$A = E_{DFT} + \Delta A_{\mathrm{RISM}} \tag{3.2}$$

$$\mu_e = \varepsilon_{\mathrm{f}} - \Phi_{\mathrm{S}} \tag{3.3}$$

$$\Omega_{\mathrm{re}} = \Omega_{N_e} - \Omega_{N_e^0 \text{ at initial state}} \tag{3.4}$$

where N_e is the number of electrons in a charged cell and N_e^0 is the number of electrons in a charge neutral cell. The electrochemical potential of the calculated system, μ_e, is the difference between the Fermi energy, ε_{f}, and the electrostatic potential in the solution, Φ_{S}. Φ_{S} is the potential at z = 30 Å of this simulation cell. Ω_{re} is the relative grand potential referenced to the grand potential of the initial state of the surface diffusion with the charge neutral cell, $\Omega_{N_e^0 \text{ at initial state}}$. The reference electrode was defined as Hg/HgO as same as the previous experiments [3,4]. The method of setting the criterion of the reference electrode follows the way developed in the previous study. For setting $\mu_e^{\mathrm{Hg/HgO}}\mathrm{vs.}\Phi_{\mathrm{S}}$, the free energy of the system of Hg/HgO was calculated as follows. $\mu_e^{\mathrm{Hg/HgO}}\mathrm{vs.}\Phi_{\mathrm{S}}$ was calculated as −5.46 eV. The applied potential of the system referenced to Hg/HgO was defined as the equation (3.7).

$$\mathrm{Hg} + 2\mathrm{OH}^- \rightleftharpoons \mathrm{HgO} + \mathrm{H_2O} + 2\mathrm{e}^- \tag{3.5}$$

$$\begin{aligned}\mu_e^{\mathrm{Hg/HgO}}\mathrm{vs.}\,\Phi_{\mathrm{S}} = {} & [A(\mathrm{Hg\ in\ 6.0\ M\ KOH\ aq.}) + E_{\mathrm{ZP}}(\mathrm{Hg}) \\ & + 2A(\mathrm{OH^-\ in\ 6.0\ M\ KOH\ aq.}) \\ & + 2E_{\mathrm{ZP}}(\mathrm{OH^-})] \\ & - [A(\mathrm{HgO\ in\ 6.0\ M\ KOH\ aq.}) + E_{\mathrm{ZP}}(\mathrm{HgO}) \\ & + A(H_2\mathrm{O\ in\ 6.0\ M\ KOH\ aq.}) + E_{\mathrm{ZP}}(\mathrm{H_2O})]\end{aligned} \tag{3.6}$$

$$E \text{ vs. (Hg/HgO)} = \mu_e - \mu_e^{\text{Hg/HgO}} \text{vs. } \Phi_S \qquad (3.7)$$

Table 3.1. Results for the calculation of $\mu_e^{\text{Hg/HgO}}$vs.Φ_S

	HgO	H_2O	Hg	OH^-
A / Ry	−131.631	−34.2483	−99.9495	−33.3606
E_{zp} / kcal mol^{-1}	0.74682	13.41186	0.0	5.40571

※Calcualtion condition of E_{zp} (in gas phase)
Package: Gaussian09, Basis set: 6-311+G(3df,2pd) for O and H, LANL2DZ for Hg,
Exchange-correlation functional: B3LYP

3.3. Results and Discussion

3.3.1. Effect of applied potential and orbital interaction of the Zn adatom and Zn(0001) surface

The applied potential was considered by changing the electron number of the system. By changing the electron number of the system, the Fermi energy of calculated systems can be varied. Since the electrochemical potential is defined as the difference between the potential in the solution and the Fermi energy, the applied potential referenced to Hg/HgO can be obtained. Figure 3.1 shows the relative grand potential profiles for the initial and transition states with respect to the charge and applied potential referenced to Hg/HgO. The point that the relative grand potential is 0 indicates that the initial state of the surface diffusion on the (0001) or interlayer diffusion in the charge neutral cells.

In Figure 3.1(a), the change in the ground potential as the charge is varied shows that the curves for the initial and transition states behave in almost the same manner. The same behavior can also be observed here corresponding to the applied potential as shown in Figure 3.1(b). At the charge-neutral case, an applied potential of −1.21 V was obtained. The equilibrium potential of the reduction of the zincate ion is −1.1873 V vs. Hg/HgO, which is approximately estimated by −1.285 V vs. SHE and +0.0977 V vs. SHE without the deviation of pH. Hence, it is considered that the potential of the point of zero charge can be matched with the equilibrium potential of the reduction of the zincate ion.

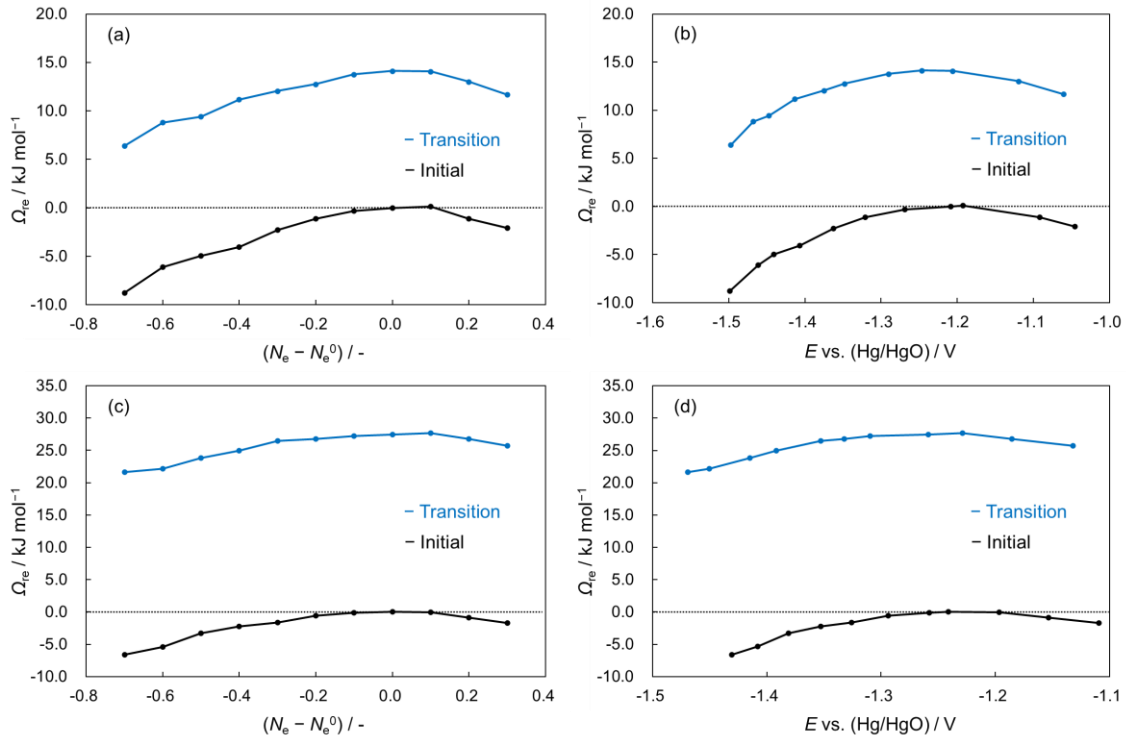

Figure 3.1. Grand potential change with respect to the change of (a) the electron number and (b) the applied potential vs. Hg/HgO for the initial and transition states of the surface diffusion on the Zn(0001) surface. Those of the interlayer diffusion are (c) and (d), respectively.

Table 3.2. Activation energy on (0001) at −1.21 V and −1.41 V vs. Hg/HgO and of the interlayer diffusion at . (Unit: kJ mol^{-1})

$E_{a(0001)}$ at −1.21 V	$E_{a(0001)}$ at −1.41 V	E_{itl} at −1.26 V	E_{itl} at −1.41 V
+14.1	+15.2	+27.6	+29.2

Both potential values of the initial and transition states at this charge-neutral cell are almost same. At this point, the activation energy was +14.1 kJ mol^{-1}. In contrast, the activation energy at around −1.41 V, where the mossy structures are deposited, is found to be +15.2 kJ mol^{-1}. This suggests a slight increase in the activation energy with respect to the negative shift of the applied potential. In Figures 3.1(c) and 3.1(d), the results of the same calculations for the interlayer diffusion are shown. The activation energy with changing the applied potential was calculated to be +27.6 kJ mol^{-1} at −1.26 V. In contrast, at −1.41 V, the activation energy was +29.2 kJ mol^{-1}. As same as the case on the Zn(0001)

surface, the activation energy increases slightly for the negative shift of the applied potential. Although the activation energy changes slightly when the potential is taken into account, this suggests that the specific behavior of Zn adatoms of the rapid surface diffusion on the (0001) surface and slow interlayer diffusion hardly change significantly. The change in activation energy due to potential effect is considered to be small in the condition of the low applied potential which the surface diffusion is a determining factor for the shape evolution of Zn deposits.

Since the specific surface diffusion behavior of Zn is not drastically changed by the applied potential, the surface diffusion behavior is intrinsic to the characteristics of Zn itself. Hence, the electronic state of the Zn adatom and surface was analyzed by the LDOS calculations to understand the interaction between the adatom and surface. The LDOS of the adsorption structure of the Zn adatom on the Zn(0001) surface was calculated shown in Figure 3.2. Figure 3.2(b) shows the LDOS of the adatom and the nearest atoms of the surface to the adatom. The LDOS of the adatom show a steep peak around −6.5 eV and a small peak around −7.0 eV. As for the peak of the surface atoms locating nearest to the adatom, a prominent peak from −8.0 eV to −6.0 eV was observed, overlapping a peak of the adatom. In order to investigate the electronic state change by the orbital interaction, LDOS was also calculated for each isolated state as shown in Figure 3.2(c) and (d). The LDOS of the isolated Zn atom exhibit the peaks at −5.7 eV, −1.8 eV, and +3.7 eV. These peaks clearly reflect the electron configuration of Zn, which is $3d^{10}4s^2$ and $4p^0$. On the other hand, the LDOS of the Zn(0001) surface appears to be similar to that of the surface with the Zn adatom. The LDOS of the surface with the adatom is slightly closer to the split peaks of the adatom. This suggests that the Zn adatoms interacts slightly with the Zn(0001) surface.

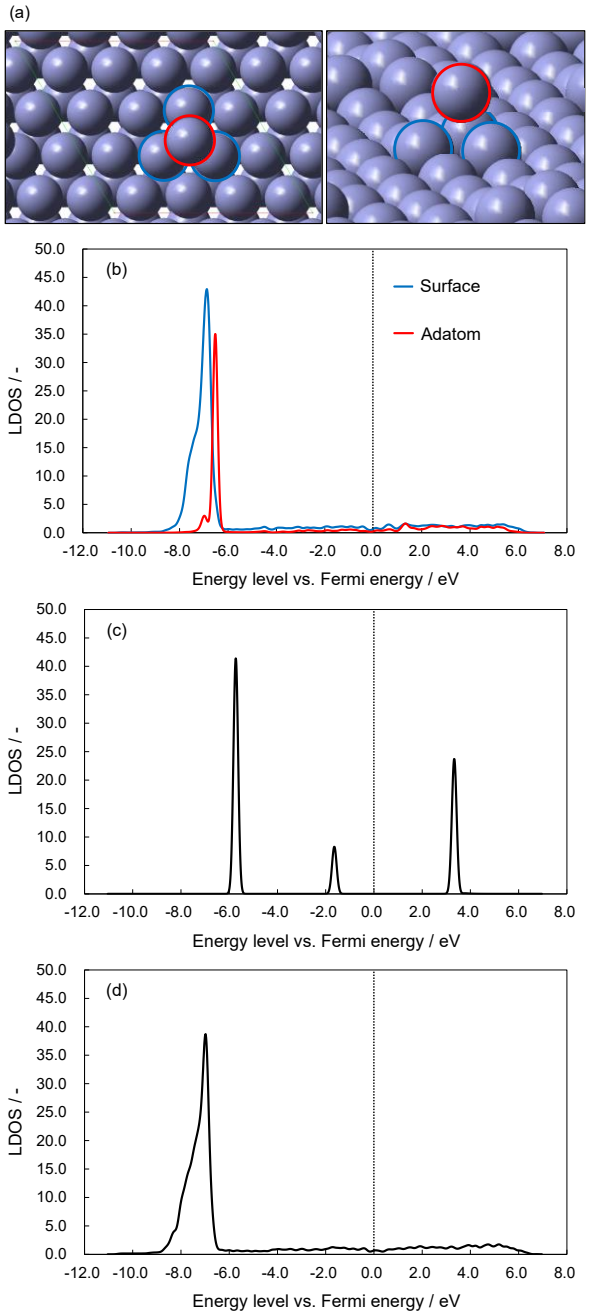

Figure 3.2. LDOS of the adsorption of the Zn atom: (a) top view and side view of the adsorption structure of the Zn atom on the (0001) surface (the Zn adatom in the next cell is omitted for visualization in the side view.), LDOS of (b) the Zn adatom and the three nearest neighbor atoms of the surface, (c) the isolated Zn atom, and (d) the isolated (0001) surface. Red and blue circles in (a) corresponds to the red and blue lines in (b), respectively. Red and green thin lines in (a) show the supercell of the model. Black dotted straight lines show 0 eV vs. Fermi energy of each structure.

The LDOSs of the adsorption of the Zn adatom on the Zn(0001) surface for 3d, 4s, and 4p are shown in Figure 3.3 to understand the orbital interaction in detail. The prominent peaks are attributed to the 3d orbitals, as indicated by the LDOS of the isolated Zn atoms. The 3d orbitals do not extend above −6.0 eV and remain in a narrow range of energy levels. On the other hand, the 4s orbitals are less abundant than the 3d orbitals but are widely distributed. The 4s orbital of the isolated Zn atom is locally distributed around −1.8 eV, as shown in Figure 3.2(c), suggesting that the 4s orbital is strongly interacting with the surface. In the case of Zn atoms, the originally empty 4p orbitals are also widely distributed below the Fermi level. This suggests that the 4p orbitals are involved in the interaction of Zn, which is generally considered to be composed of fully occupied orbitals. These results indicate that in the adsorption of Zn atoms, the 3d orbital, which could be the most dominant in the interaction, is weak, and the 4s and 4p orbitals are interacting with the surface.

The interaction of Zn adatoms with surfaces is discussed in comparison with the case of Cu, which shows the deposition without the mossy structures. As mentioned in Chapter 2, the activation energies of the surface diffusion of the Cu adatom on the Cu surface are higher than that of Zn. The activation energies are +31.0 kJ mol^{-1} on the (111) surface and +64.1 kJ mol^{-1} for the interlayer diffusion. In addition to the activation energy, the difference in the binding energy between Zn and Cu is calculated on each surface. Table 3.3 shows the binding energy of Zn atom on the Zn(0001) surface and Cu atom on the Cu(111) surface. The biding energy of the Zn case is less negative than that of the Cu case. This suggests that Zn bonds with the surface weaker than Cu. These differences in energies should be caused by the difference in the electronic state. Hence, the electronic state of the Cu is also analyzed for the comparison with Zn.

Table 3.3. Binding energy on each case. (unit: kJ mol^{-1})
Binding energy, $E_{bind} = E_{adsorption\text{-}system} - E_{isolatedZn+surface}$, is calculated in the gas phase. k-points grid is set as 2 × 2 × 1.

Zn on Zn(0001)	Cu on Cu (111)
−44.6	−310.3

The LDOS of the Cu adatom adsorbed on the Cu(111) surface shows that the 3d orbitals are distributed in the range of −4.0 to −1.0 eV, which is different from Zn. Peak splitting of these 3d orbitals is observed at −3.6 and −1.8 eV. This splitting originates from the bonding and antibonding orbitals between the adatom and surface. In particular, compared to the isolated system as shown in Figure 3.4, the adatom orbitals may be pulled to lower energies due to the interaction with the Cu(111) surface. As for the 4s and 4p orbitals, it was found that the orbitals extend throughout the level and interact with each other, similar to Zn. This result suggests that the interaction of the 3d orbitals is modified by the 4s orbitals; when the 4s orbitals are fully occupied, the interaction of the 3d orbital is weakened, which is corresponding to Table 3.3.

This difference in electronic state causes a difference in the surface diffusion behavior of the two elements. The results in the previous chapter suggest that the surface diffusion of Zn adatoms on the Zn(0001) surface is small, about half the activation energy of Cu adatoms on the Cu(111) surface, suggesting that Zn adatoms diffuse rapidly on the Zn(0001) surface as mentioned in the previous chapter. The 3d orbitals of Zn adatoms interact weakly with the surface, suggesting that Zn adatoms are not strongly retained on the surface. On the other hand, the Cu adatom has a different orbital shape than the Zn adatom, and thus a different interaction mechanism. The 3d orbitals of the Cu adatom and Cu(111) surface can strongly interact with each other. Therefore, Zn adatoms on a Zn(0001) surface can diffuse rapidly, whereas Cu adatoms on the Cu(111) surface diffuse slowly. These results suggest that different interactions, especially in the 3d orbitals, are responsible for the rapid surface diffusion on the Zn(0001) surface, which is caused by the difference of the existence of the vacancy of the 4s orbitals.

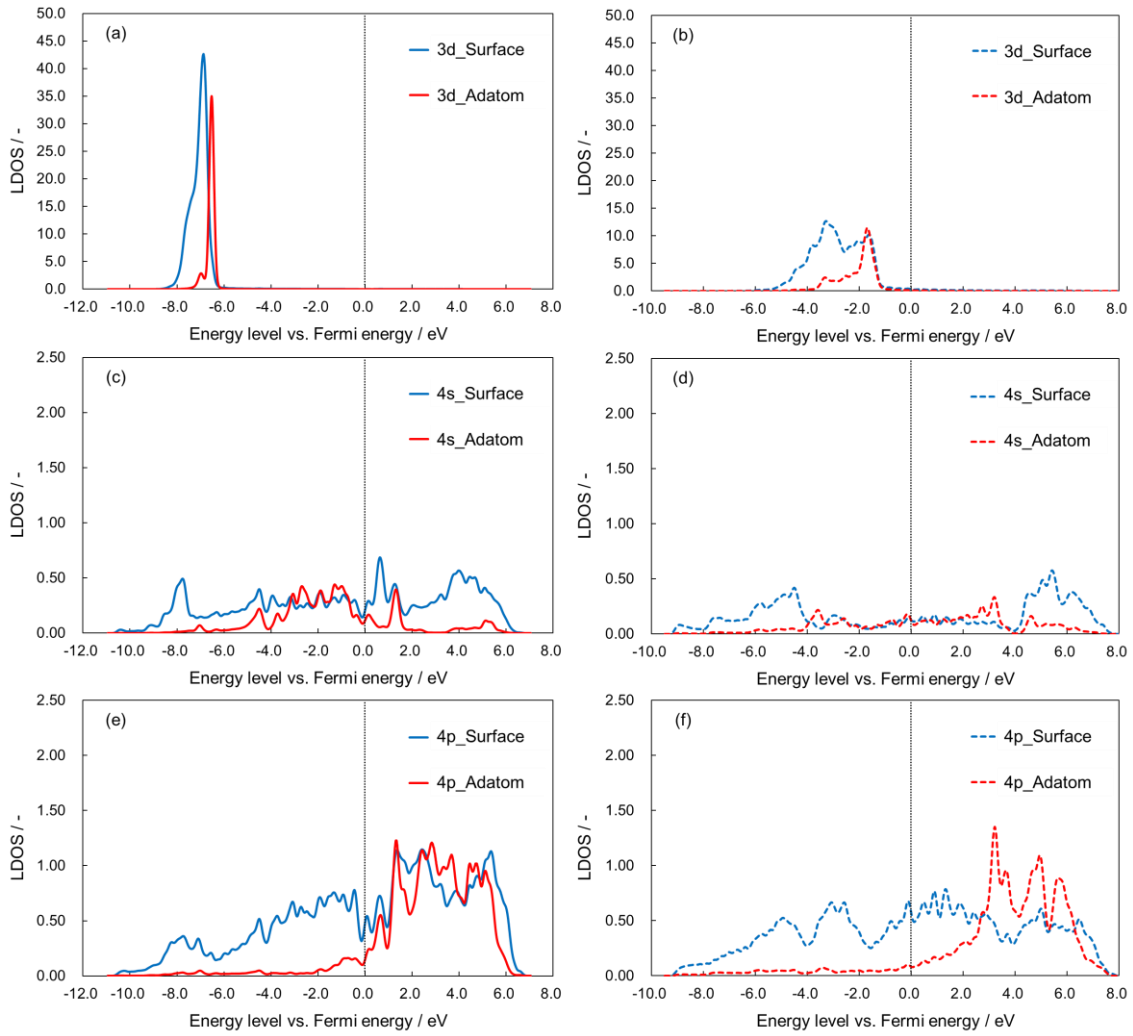

Figure 3.3. LDOS of the Zn adsorption structure on the (0001) surface: (a) 3d orbital, (c) 4s orbital, and (e) 4p orbital. LDOS of the Cu adsorption structure on the (111) surface: (b) 3d orbital, (d) 4s orbital, and (f) 4p orbital. Red and blue lines show the LDOS of the adatom and three nearest neighbor atoms, respectively. Black dotted lines show 0 eV vs. Fermi energy.

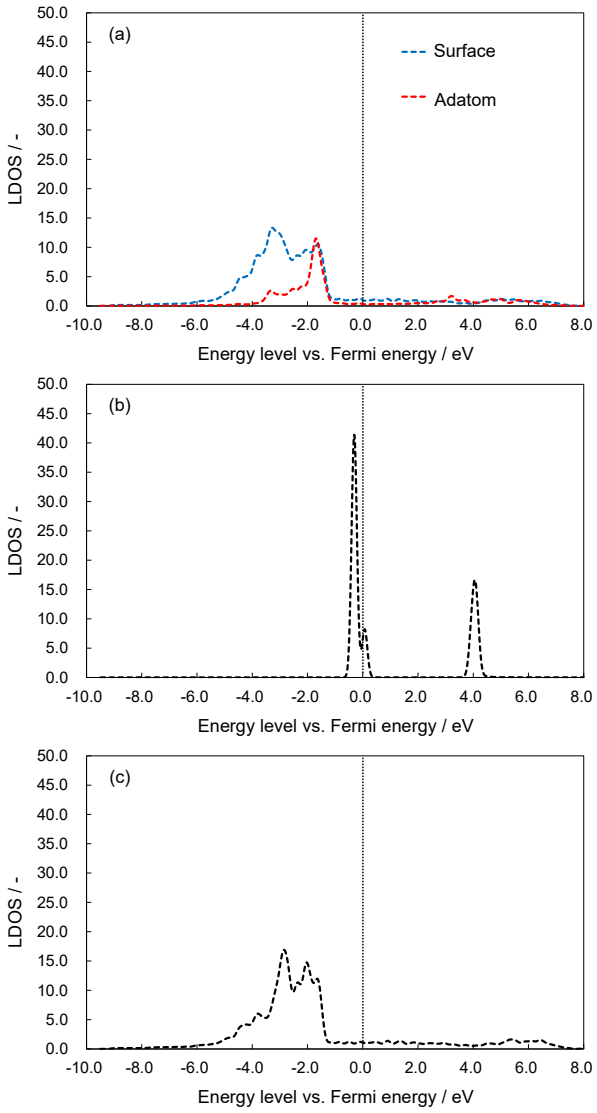

Figure 3.4. LDOS of (a) the Cu adatom and the three nearest neighbor atoms of the surface, (c) the isolated Cu atom, and (d) the isolated Cu(111) surface. Red and blue dotted lines show the LDOS of the adatom and three nearest neighbor atoms in (a). Black dotted straight lines show 0 eV vs. Fermi energy of each structure.

Table 3.4. Fermi energy on each case. (unit: eV)

Zn on Zn(0001)	Cu on Cu (111)
−4.432	−4.544

Table 3.5. Fermi energy on isolated atom and surface (unit: eV)

Zn	Cu
−4.489	−4.685

3.3.2. Orbital interaction of Zn adatom and surface during the interlayer diffusion

For the shape evolution of Zn, the rapid surface diffusion and the slow interlayer diffusion is a significant factor. In the case of interlayer diffusion of Zn, which shows the specific activation energy called the Ehrlich-Schwoebel barrier, the interaction between the Zn adatom and the surface is also investigated in the same way because the rate balance of the flat (0001) diffusion and the interlayer diffusion is suggested as a key factor for the initiation of the layer-by-layer structures depositing under the mossy structures. The electronic states of the adatom and surface are examined in the transition state to analyze the change of the interaction during the downward diffusion from the terrace position to the step position shown in Figure 3.5. The large overlap between the adatom and surface can be observed around −6.2 eV. In addition, as for the adatom, the small peak at −7.0 eV disappeared, which was observed in the adsorption on the Zn(0001) surface. This indicates that the Zn atoms of the step structure strongly interacts with the adatom, and its electronic state is relatively similar to the adatom than the case on the (0001) surface. Peaks of the adatom and the surface near −2.2 eV and +3.1 eV can be derived from 4s and 4p orbitals. It is found that the electronic state of the adatom itself during the interlayer diffusion is inherited from the isolated Zn atom in contrast to the diffusion on the (0001) surface. This suggests that the stability of the adsorbed atoms themselves can be a dominant factor for the interlayer diffusion. The electronic configuration of Zn atoms is fully occupied, and thus exhibits a certain degree of stability.

These analyses suggest that the balance of the surface diffusion rate of the Zn adatom on the surface is due to the fully occupied electronic state of Zn, $3d^{10}4s^2$, which enables the rapid flat diffusion on the (0001) surface, and moderately slow interlayer diffusion. The former is attributed to the weak interaction of the 3d orbital between the adatom and surface. The latter is caused by the stability of the Zn adatom itself.

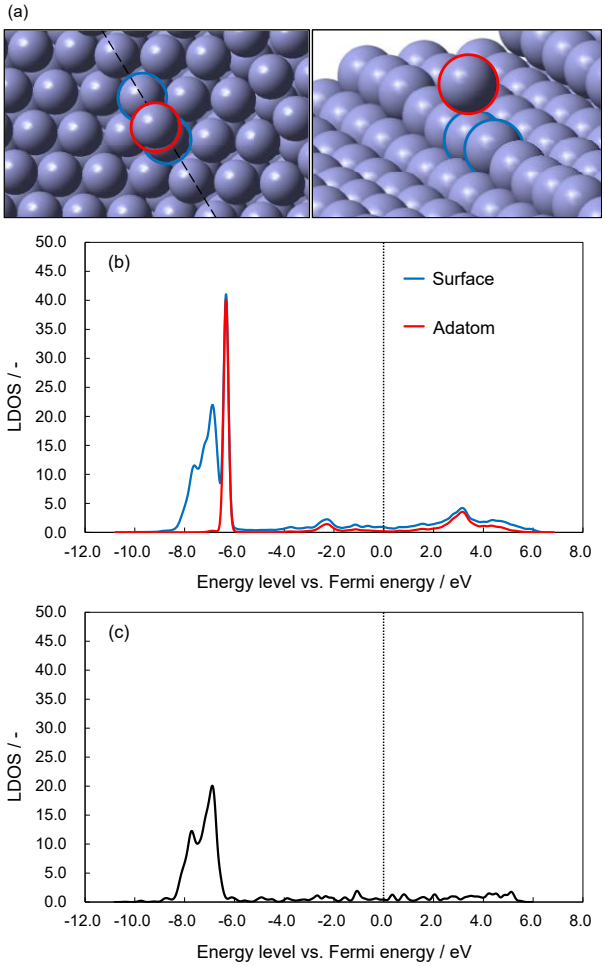

Figure 3.5. LDOS of the transition state structure of the Zn adatom interlayer diffusion at the step-terrace structure of the (0001) surface: (a) top view and side view of the structure of the Zn atom on the step-edge structure, (b) LDOS of the Zn adatom and the two nearest neighbor atoms of the surface, and (c) LDOS of the isolated step-edge structure. Red and blue circles in (a) corresponds to the red and blue lines in (b), respectively. Black long-dotted line in (a) shows the edge structure of the step-terrace model. Black dotted lines in LDOS show 0 eV vs. Fermi energy of each structure. Fermi energy is −4.273 eV.

Conclusions

This chapter focused on the electronic state of the Zn adatom and the surface to elucidate the dominant factor for the specific surface diffusion behavior of Zn during the electrodeposition. The surface diffusion rates of the rapid diffusion on the (0001) surface and the slow interlayer diffusion are derived from the fully occupied electronic configuration of Zn, $3d^{10}4s^2$. The weak interaction of Zn adatoms with the Zn(0001) surface is found to be the origin of the rapid surface diffusion on the Zn(0001) surface. The comparison of Zn and Cu indicates that this weak 3d orbital interaction is attributed to the complete occupation of the 4s orbital while that is not observed in the Cu case which has no vacancy of 4s orbitals. In addition, the moderately slow interlayer diffusion rate of Zn adatoms is also governed by the stable electronic configuration of Zn. The specific electronic configuration of Zn is responsible for the specific values of the surface diffusion rate. Analysis of these electronic configurations may provide insight into atomic-level considerations of electrodeposition and guide the development of a theory of the system. For further analysis of the electronic state of the surface, the other metals should be analyzed. The systematic understanding of the electronic state and the surface diffusion behavior will lead to further effective development of the electrodeposition processes.

References

[1] B. E. Conway, J. O'M Bockris, On the Calculation of Potential Energy Profile Diagrams for Processes in Electrolytic Metal Deposition. *Electrochim. Acta* 3 (1961) 340-366.

[2] B. E. Conway, J. O'M. Bockris, The Mechanism of Electrolytic Metal Deposition, *Proc. Roy. Soc.* A248 (1958) 394-403.

[3] T. Otani, M. Nagata, Y. Fukunaka, T. Homma, Morphological Evolution of Mossy Structures during the Electrodeposition of Zinc from an Alkaline Zincate Solution, *Electrochim. Acta* 206 (2016) 366-373.

[4] T. Otani, Y. Fukunaka, T. Homma, Effect of Lead and Tin Additives on Surface Morphology Evolution of Electrodeposited Zinc, *Electrochim. Acta* 242 (2017) 364-372.

[7] P. Giannozzi, S. Baroni, N. Bonini, M. Calandra, R. Car, C. Cavazzoni, D. Ceresoli, G. L. Chiarotti, M. Cococcioni, I. Dabo et al., QUANTUM ESPRESSO: a Modular and Open-Source Software Project for Quantum Simulations of Materials, *J. Phys.: Condens. Mater.* 21 (2009) 395502.

[8] P. Giannozzi, O. Andreussi, T. Brumme, O. Bunau, M. B. Nardelli, M. Calandra, R. Car, C. Cavazzoni, D. Ceresoli, M. Cococcioni et al., Advanced Capabilities for Materials Modeling with QUANTUM ESPRESSO, *J. Phys.: Condens. Matter* 29 (2017) 465901.

[9] H. J. Monkhorst, J. D. Pack, Special Points for Brillouin-Zone Integrations, *Phys. Rev. B* 13 (1976) 5188-5192.

[10] K. Kovalenko, F. Hirata, Self-Consistent Description of a Metal-Water Interface by the Kohn-Sham Density Functional Theory and the Three-Dimensional Reference Interaction Site Model, *J. Chem. Phys.* 110 (1999) 10095-10112.

[11] R. Y. Wang, D. W. Kirk, G. X. Zhang, Effects of Deposition Conditions on the Morphology of Zinc Deposits from Alkaline Zincate Solutions, *J. Electrochem. Soc.* 153 (2006) C357-C364.

[12] G. Ehrlich, F. G. Hudda, Atomic View of Surface Self-Diffusion: Tungsten on Tungsten, *J. Chem. Phys.* 44 (1966) 1039-1049.

[13] R. L. Schwoebel, E. J. Shipsey, Step motion on Crystal Surfaces, *J. Appl. Phys.* 37 (1966) 3682-3686.

Chapter 4:

Effect of Li^+ Addition during the Initial Stage of Zn Electrodeposition by Multiscale Simulation and Experiments

4.1. Introduction

Chapters 2 and 3 mainly focused on the analysis of Zn electrodeposition including the surface diffusion of Zn adatoms to understand the origin of the irregular shape evolution of Zn. For the irregular shape evolution of the mossy structures, the surface diffusion behavior is a dominant factor at the low current density. This phenomenon during the electrodeposition is affected by the presence of the electrolyte at the solid-liquid interface as shown in Chapter 2. The effect of the solvation structure can change the behavior of the surface diffusion. Furthermore, in order to suppress the irregular shape evolution, the electrolyte composition should be designed properly. Hence, this chapter focuses on the effect of the electrolyte condition for the surface diffusion at the solid-liquid interface.

The solvation condition near the surface is usually changed by additives that do not deposit on the surface during the electrodeposition. Many types of additives have been studied and each has been shown to affect the shape evolution of Zn [1,2]. In particular, cationic molecules and metal ions are effective suppressors for the irregular shape evolution [3-10]. For example, molecules with quaternary ammonium moieties adsorb on the protrusions that initiate the mossy structure [3]. It is suggested that the additives with pyridine moieties also exhibit a similar mechanism [4]. In addition to these cationic additives, the effects of alkali metal ions have also received attention [11-16]. Fukumoto et al. suggested that certain molecular additives exhibit a synergistic effect with Na^+, with stronger adsorption on the electrode in the presence of Na^+ [12]. Thakur et al. reported that the discharge capacity of Zn-air batteries is improved by Li^+ in the presence of K^+ [13]. Regarding the effect of Li+ addition, Guo et al. also reported that the battery with the LiCl additive in the electrolyte showed good stability in long-cycle tests [14]. The other previous study also claimed the effect of Li^+ addition [15]. Li^+, which exhibits the largest charge density among alkali cations, is thought to interact with surface species at the outermost layer of the Helmholtz plane [16] and has interesting differences from other types of additives that act as adsorbed species. Hence, further molecular level understanding of such effects of Li^+ is required for the further development of electrolyte

designs.

Such a solvation effect of the Li^+ addition will affect the surface diffusion behavior of Zn. As mentioned above, the comparison of activation energy differences between the solid-liquid and solid-gas interfaces in Chapter 2 suggests that surface diffusion rates are affected by the solvation of water molecules surrounding the surface. Solvent molecules interact with Zn adatoms and Zn surfaces, altering the behavior of Zn adatoms during the surface diffusion. Alkali metal cations such as Li^+ alter the distribution of solvent molecules near the interface and should have a non-negligible effect on Zn shape evolution at the initial stage of the deposition. In this chapter, It is analyzed the effect of alkali metal ion, Li^+, on the deposition shape of Zn, by using multiscale simulations comprising density functional theory (DFT) and kinetic Monte Carlo (KMC) simulations. The deposition behavior with the Li^+ condition is compared to the condition that only contains KOH in the solution. as a supporting electrolyte by using effective screening medium (ESM) combined with reference interaction site model (RISM) as same as the previous chapters. In addition, the conventional electrochemical measurements are performed especially for the initial stage of the Zn deposition to compare with the simulation, examining the effect of the Li^+ addition for the Zn shape evolution.

4.2. Methods

4.2.1. Multiscale simulation of the surface diffusion of the Zn adatom under the Li^+ condition

In this chapter, all the calculation conditions are the same as Chapter 2. All DFT calculations employed ESM-RISM [17,18] implemented in Quantum ESPRESSO code [19,20] to simulate the solid-liquid interface under the Li^+ condition. The optimized potentials for liquid-phase simulation [21,22] were taken for the parameters of Li^+, K^+, and OH^-. In the RISM region, 6.0 M LiOH is introduced when it is the Li^+ condition.

As same as Chapter 2, four specific surface diffusions were assumed to obtain the activation energy: the surface diffusion on the (0001) surface, the (0−110) surface, the interlayer diffusion, and the edge diffusion. The potential curves of the surface diffusion of the Zn adatom were acquired with these four models in the Li^+ condition. The relative energies, E_{re}, of each position were obtained by the same equation as shown in Chapter 2:

$$E_{\mathrm{re}} = E_{\mathrm{each\_position}} - E_0 \quad (4.1)$$

$E_{\mathrm{each\_position}}$ denotes the total electron energy at each position, while E_0 denotes the one at the initial position before the surface diffusion. The activation energy was determined as the highest relative energy in the surface diffusion pathway.

As for the KMC simulations, the same KMC code as Chapter 2 is used. The activation energy used in the KMC simulation is changed to the ones obtained by DFT in the Li^+ condition. By using these parameters, the surface diffusion behavior in the Li^+ condition is reflected.

4.2.2. Electrodeposition of Zn with the Li^+ addition

Zn electrodeposition on the negative electrode was performed with alkaline zincate

solution. For the analysis of the effect of the Li^+ addition, LiOH was added into the electrolyte as the additive with maintaining the OH^- concentration. Two types of solution were prepared: 1.0 mol dm^{-3} $LiOH{\cdot}H_2O$ (Kanto Chemical, Cica-reagent grade) + 5.0 mol dm^{-3} KOH (Kanto Chemical, Cica-reagent grade) + 0.5 mol dm^{-3} ZnO (Kanto Chemical, Cica-reagent grade), and 6.0 mol dm^{-3} KOH + 0.5 mol dm^{-3} ZnO. In the case of the Li^+ addition, LiOH into the KOH solution is dissolved firstly. ZnO is dissolved into the solution. All the solutions were deaerated by nitrogen bubble prior for 10 minutes before electrochemical measurements as same as previous studies [23,24].

The electrochemical measurements were performed with the three-electrodes system. Cu plate with chemical mechanical polishing was utilized as the working electrode. Surface area of the working electrode was set to 0.50 cm^2. Hg/HgO (Inter Chemie. Inc.) and Zn wire (Nilaco, 99.99%) were utilized as the reference electrode and the counter electrode. The pipe of the reference electrode was wrapped by the Zn wire. As the surface pretreatment, the Cu plate was immersed in 45.0 mL ultrapure water (18.2 MΩ cm) + 5.0 mL 96 wt% of sulfuric acid for 30 s and the Zn wire was immersed in 180 mL pure water + 20.0 mL 96 wt% of sulfuric acid for 10 s before the electrodes were rinsed by the pure water and dried in blowing N_2 air. The working electrode was faced upward to the reference electrode and placed horizontally at the bottom of the cell, in order to flow the natural convection uniformly during the electrochemical measurements.

An electrochemical measurement system (HZ-7000, Hokuto Denko) was utilized for all electrodeposition processes at room temperature (23°C). The galvanostatic deposition was conducted for passed charge, 0.5 C cm^{-2}, (at −1.0 mA cm^{-2} for 500 s) in order to analyze the initial structures of the Zn deposits. The deposition potential of Li^+ is considerably negative than that of Zn, and the activity of Li in the Zn-Li alloy is on the order of 10^{-10} at room temperature, which is sufficiently small compared to Zn, based on the alloy phase diagram and electrochemical measurements of the previous study [25]. The crystal structure of the deposit was analyzed by X-ray diffractometer (XRD, Rigaku, Rint-Ultima III) in the Materials Characterization Central Laboratory, Waseda University [26]. A scanning electron microscope (SEM, SU-8200) was used for the observation of the surface morphology of the electrodeposited Zn.

4.3. Results and Discussion

4.3.1. Difference of the surface diffusion behavior between Li^+ and K^+ conditions

The surface diffusion behavior of the Zn adatom under the condition with Li^+ is analyzed by putting 6.0 M LiOH in the RISM region and compared the results with the K^+ condition as shown in Chapter 2. In the ESM-RISM calculations, the distribution of the electrolyte species near the surface is obtained. The change of the distribution of the species during the surface diffusion is analyzed. Figure 4.1(a) shows the potential curve of the surface diffusion of the Zn adatom on the (0001) surface. The activation energy is +14.5 kJ mol^{-1}, which is similar to +14.1 kJ mol^{-1} in the K^+ condition. These results indicate that in the Li^+ condition, the Zn adatom diffuses on the (0001) surface as rapid as in the K^+ condition. Figure 4.1(b) shows the potential curve of the surface diffusion on the (0−110) surface. The activation energy on this surface is +41.3 kJ mol^{-1}, which is lower than +45.7 kJ mol^{-1} obtained in the K^+ condition as shown in Table 4.1. In Chapter 2, the activation energies on the (0−110) surface in vacuum and that in the K^+ condition were compared. It is suggested that the activation energy of the surface diffusion on the (0−110) surface was influenced by water molecules. The (0−110) surface strongly interacts with water molecules, which can interfere with the surface diffusion of Zn adatoms on the (0−110) surface. Therefore, the decrease in the activation energy due to the Li^+ addition should be attributed to the change in the interaction between the surface and water molecules due to Li^+. Figure 4.1(c) shows the potential curve for the interlayer diffusion at the step-edge structure. The activation energy of the interlayer diffusion is +23.1 kJ mol^{-1}, which is smaller than +29.1 kJ mol^{-1} in the K^+ condition. The effect of the Li^+ addition is exhibited in the interlayer diffusion as well as in the (0−110) surface. This decrease in activation energy means that interlayer diffusion is more rapid in the Li^+ condition than the K^+ condition. Figure 4.1(d) shows the potential curve of the edge diffusion, which shows the activation energy of +19.0 kJ mol^{-1}. In contrast to the other surface diffusion behaviors, the activation energy of the edge diffusion in the Li^+ condition is larger than in the K^+ condition. Chapter 2 indicated that adatoms are

stabilized at the edge by solvation because the solvation effect of water molecules reduces the activation energy of edge diffusion. This suggests that Li^+ weakens the stabilizing effect of the solvent species, resulting in a higher activation energy than in the absence of Li^+.

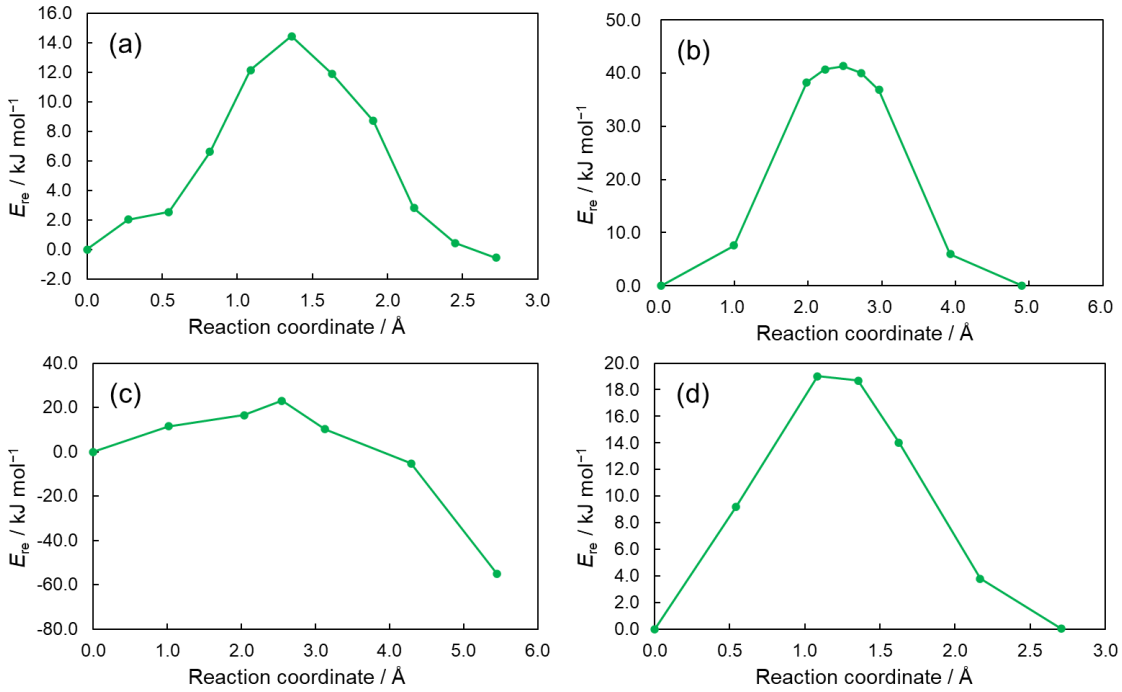

Figure 4.1. Potential curves of the Zn adatom surface diffusion at the solid-liquid interface with the 6.0 M LiOH solution: (a) on the (0001) surface, (b) on the (0−110) surface, (c) interlayer diffusion, and (d) edge diffusion.

The difference of the activation energy with the Li^+ and K^+ condition should be attributed to the structural change of the solvation at the solid-liquid interface because both cations cannot deposit on the surface due to its negative deposition potential. Hence, the distribution of the electrolyte species, which can be obtained by the ESM-RISM calculation, are analyzed. Figure 4.2(a) shows the distributions of the O atom of the water molecules near the (0001) surface. The distribution appears due to the electrostatic potential of the surface. All peaks of the O atom in the Li^+ condition are smaller than those in the K^+ condition, which indicates that the Li^+ addition decreases the density of water molecules. Figure 4.2(b) shows the distributions of Li^+ and K^+. The peaks of Li^+ are larger than those of K^+. The largest peak of Li^+ is observed around 7.1 Å whereas that

of K^+ can be seen around 6.1 Å. These differences in distribution can be attributed to charge density and ionic radius of Li^+ and K^+. A large charge density of Li^+ results in a strong interaction between Li^+ and water molecules. This leads to a rigid solvation sphere and large hydration cation radius of Li^+ [27,28]. Due to its largeness of the Stokes radius [29], these solvated species with large and rigid spheres approaches to the surface with space compared with the K^+ condition. The rigid interaction makes it difficult to change their orientation when they interact with the surface. Furthermore, since water molecules interact with Li^+, it can be expected that the number of water molecules that can move freely and interact with the surface decreases compared with the case of K^+, which is also proposed as the similar effect of the solvation for the diffusion of $Zn(OH)_4^{2-}$ [30]. Through this mechanism, the density of water molecules near the surface is thought to be reduced with the Li^+ addition than with K^+.

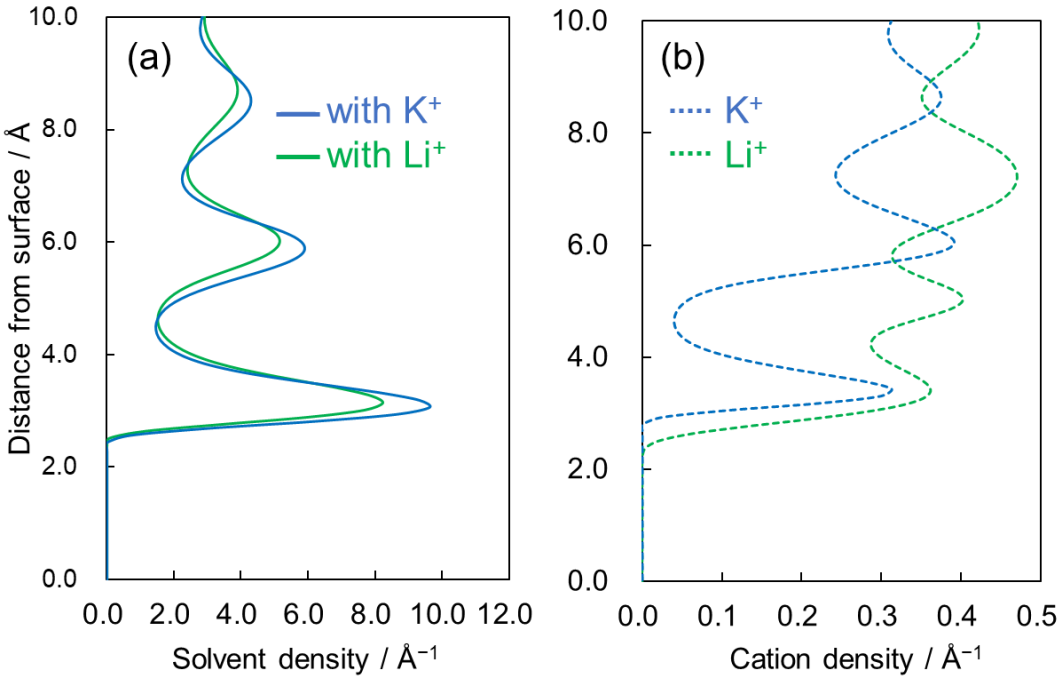

Figure 4.2. Distribution of the electrolyte species obtained by the RISM calculations: (a) O atom of H_2O in the K^+ condition with the dashed line and the Li^+ condition with the solid line, (b) K^+ and Li^+ in each solution with the blue and green lines, respectively. The horizontal axis means the distance from the average height of the Zn layer of the slab model attaching with the solvent. The lateral axis means the density of the species.

Based on the strong interaction between Li^+ and water molecules, the change of the activation energy with Li^+ at the solid-liquid interface can be discussed. Water molecules solvated with Li^+ have less ability to change their orientation due to the interaction with Li^+. Furthermore, the density of water molecules near the surface is also lower than that of K^+ because there are fewer free water molecules which shows no interaction with the cations. Therefore, on high-index surfaces such as the (0−110) plane and the step-terrace structure of the (0001) plane, where the solvation effect is more pronounced, the effect of solvation on surface diffusion is smaller and the activation energy of surface diffusion is reduced. The increase in activation energy due to solvation is also suggested in Chapter 2. In the comparison of the activation energy of surface diffusion at the solid-gas interface and the solid-liquid interface, larger values are obtained at the solid-liquid interface. This result with the Li^+ addition is considered to be consistent with the comparison.

On the other hand, the other previous study suggests that cationic species can have an effect outside the first solvation sphere [29]. This study states that the difference in the range reached by the outermost orbitals of the cationic species is important: for K^+, solvents up to nearly 9 Å are affected with their electron distribution. Although it is not clear from this previous study whether the interaction of K^+ and water molecules is rigid, if the electron distribution is changed by K^+, a different mechanism can be considered: in Li^+, water molecules with the same properties as in the bulk are present in the vicinity of the surface, whereas in K^+, “special” water molecules which shows the different features from the bulk water molecules with a changed electron distribution are present in the vicinity of the surface and adatom. This difference in electron distribution can be attributed to electrostatic interactions with surfaces and adatoms. In this case, rather than a reduction in solvation effect by Li^+, it may be thought of as an inhibition of surface diffusion by water molecules whose electron distribution altered by K^+. The simulation of this study does not incorporate such an effect. To investigate whether such an effect exists or not, it would be effective to perform a similar study using a*b initio* Molecular dynamics.

As mentioned above, the rapid surface diffusion on the (0001) surface and the moderately slow interlayer diffusion are the important factors for the shape evolution. In the Li^+ condition, the activation energy of the surface diffusion on the (0001) surface is

similar to that in the K^+ condition while that of the interlayer diffusion is smaller than that in the K^+ condition. This should cause the change of the shape evolution mechanism during the Zn electrodeposition. The shape evolution behavior of Zn in the Li^+ condition will be analyzed.

Table 4.1. Activation energy obtained from the DFT calculations

	$E_{a(0001)}$ / kJ mol^{-1}	$E_{a(0-110)}$ / kJ mol^{-1}	E_{itl}/ kJ mol^{-1}	E_{edge}/ kJ mol^{-1}
LiOH	+14.5	+41.3	+23.1	+19.0
KOH	+14.1	+45.7	+29.1	+15.5

Table 4.1 summarizes the activation energies obtained by the DFT calculations with Li^+ as the comparison with K^+. These values are used in the KMC simulation to investigate the effect of the change of the surface diffusion behavior by the Li^+ addition for the Zn shape evolution. Figure 4.3(a) shows the snapshots of the KMC simulation with the Li^+ addition. At the time of deposition of 1000 atoms, which corresponds to approximately 10^{-6} s after deposition started, the deposits are observed with an expanded 2D layer structure. As deposition proceeds, the layers expand in the 2D direction to become a complete (0001) layer. On the layer deposited after the first layer, another 2D nucleation and growth is observed. After 40,000 atoms have been deposited (corresponding to about 10^{-4} s of deposition duration), the layer-by-layer structures of the (0001) facets are observed. As shown in Figure 4.3(b), although the simulation results in the K^+ condition observed the layer-by-layer structures, the area of each layer, called terrace, is larger in the Li^+ condition. The layer-by-layer structures with large terraces eventually lead to a smooth surface. This suggests that the (0001) surface grows preferentially when the Zn is electrodeposited with the Li^+ addition. The larger area of the layer-by-layer structures should be due to the lower activation energy of interlayer diffusion because of the addition of Li^+. The interlayer diffusion rate is a significant factor to determine the 2D expansion of the layer-by-layer structures on the (0001) surface. The larger rate of interlayer diffusion causes the larger area of the layer-by-layer structure because the Zn adatoms deposited on the deposited Zn layer are more likely to diffuse to the lower layers. Therefore, the addition of Li^+ decreases the activation energy of interlayer diffusion and increases the area of the layer-by-layer structure.

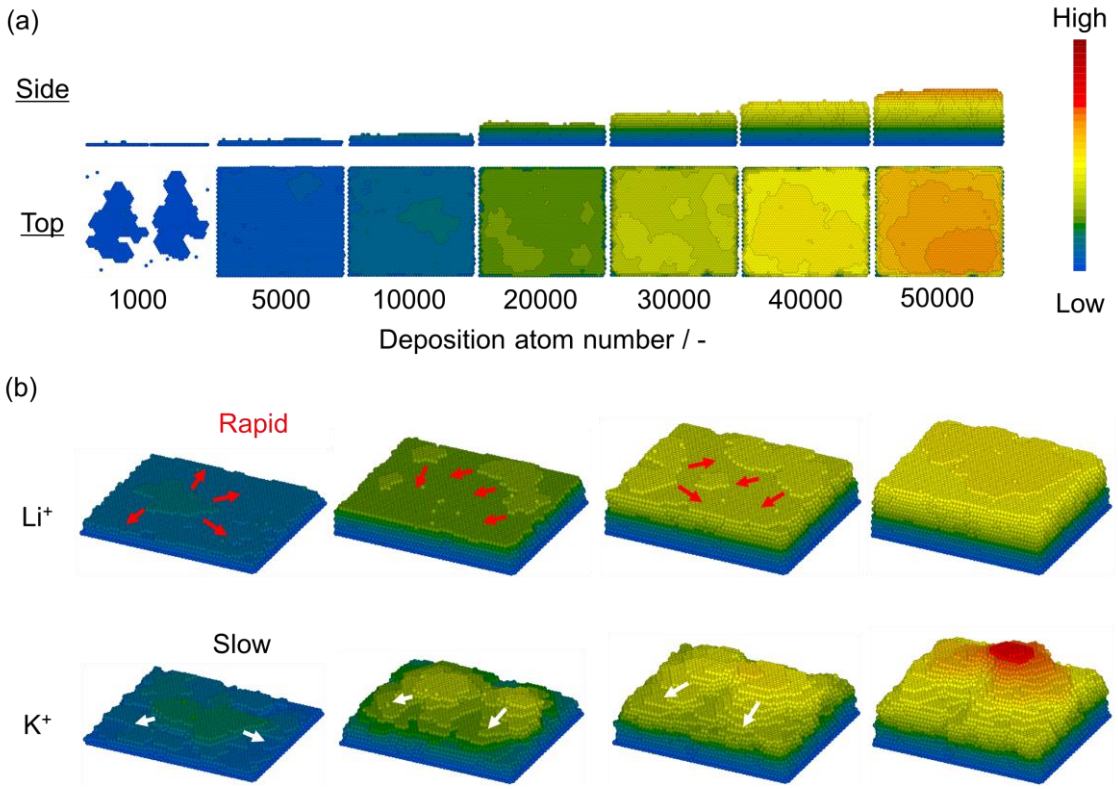

Figure 4.3. (a) Snapshots of the KMC simulations in 6.0 M LiOH condition. Surface diffusion rates were derived from DFT in the LiOH condition. (b) Comparison of simulation results with the Li^+ and K^+ conditions.

4.3.2. Zn shape evolution with Li^+ addition at the initial stage of the Zn electrodeposition

In order to investigate the Zn shape evolution behavior at the initial stage of the electrodeposition, which is significant for the initiation of the irregular shape evolution, the electrodeposited films of Zn were analyzed after the electrodeposition in short duration. The initial stage structures should be analyzed because the nanoscale layer-by-layer structures are corresponding to the initial structures of the Zn deposits. By checking the difference in the layer-by-layer structures when it is deposited with and without Li^+, the experimental results are compared with the results of the multiscale simulation. Hence,

the deposited Zn structures obtained after the short duration of the electrodeposition in the low current density condition are observed in this section. Figure 4.4(a) and (b) show the SEM images of the electrodeposited Zn at −1.0 mA cm^{-2} after passing 0.5 C cm^{-2} in the Li^+ and K^+ condition, respectively. This duration is corresponding to the initial stage of the electrodeposition. In the absence of Li^+, the layer-by-layer structures with the hexagonal corners are accumulated as observed before [23], whereas in the presence of Li^+, larger area of the layer-by-layer structures appear. Since these structures are obtained at the initial stage of the deposition, this can be connected to the results of the KMC simulations. The expanded layer-by-layer structures in the Li^+ condition are considered to be reproduced by the multiscale simulation. As for the case that further amount of Zn deposits, mossy structures appear basically even when further amount of the coulomb is electrodeposited for Zn with the Li^+ addition as shown in Figure 4.5, although the amount of the mossy structures may decrease slightly.

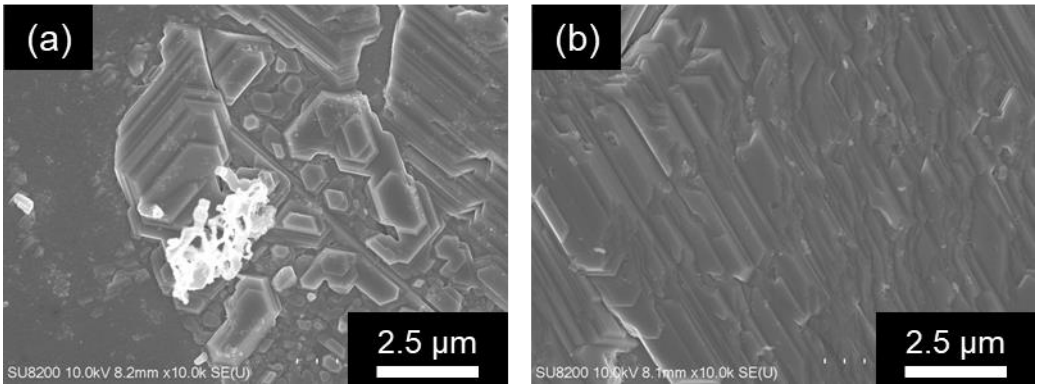

Figure 4.4. Morphological evolution of the electrodeposited Zn at 0.5 C cm^{-2}: (a) 6.0 M KOH, (b) 1.0 M LiOH + 5.0 M KOH.

For evaluation of the crystal orientation of the electrodeposited Zn, the XRD measurement was performed for the films after the electrodeposition for passed charge of 0.5 C cm^{-2}. Figure 4.6 shows the XRD patterns of Zn deposits with the Li^+ and K^+ conditions. The peak of the hcp-Zn (0001) was observed in both conditions. In particular, the peak of the Zn(0001) facets becomes larger in the case with Li^+, and the peaks of hcp-Zn (0−111) maintains almost the same intensity in both conditions. This suggests that the inside of the Zn deposits with the Li^+ addition is piled up as the (0001) plane.

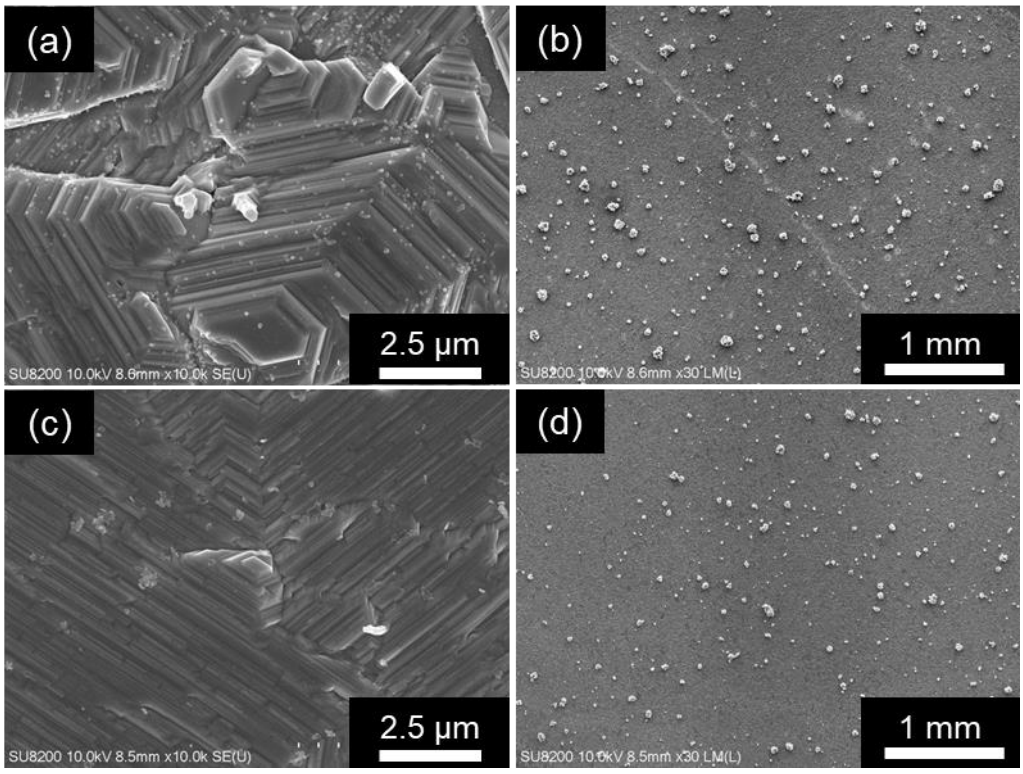

Figure 4.5. Morphological evolution of the electrodeposited Zn at 2.0 C cm^{-2}. SEM images of the position without evolution of mossy structures of (a) 6.0 M KOH, (c) 1.0 M LiOH + 5.0 M KOH. (b) and (d) are the magnified pictures of (a) and (c), respectively.

As for the concentration of LiOH, 6.0 M LiOH was set in the simulation to compare the results of 6.0 M KOH. On the other hand, the concentration in this experiment was set as 1.0 M LiOH + 5.0 M KOH to maintain the OH^- concentration and to dissolve LiOH as large as possible with maintaining the electrolyte stability. The pre-experiment to check the dependence of the concentration of Li^+ indicated that the Zn crystallinity was not drastically changed by the Li^+ concentration when it is 0.1 and 0.5 M of the Li^+ concentration. Hence, the concentration was set as 1.0 M to make the concentration as high as possible with keeping the concentration of OH^-. However, according to the solubility of LiOH, LiOH can be dissolved 5.1-5.2 M [31]. For further analysis of the dependence of the Li^+ concentration, the preparation way of the electrolyte should be improved. In the case that the concentration of Li^+ is different, the possibilities of its effect can be considered. For example, the interaction between the Zn precursor and Li^+ may be

changed when the concentrations of both are changed. systematic analysis of this system will expand the understanding of the working mechanism of the additives.

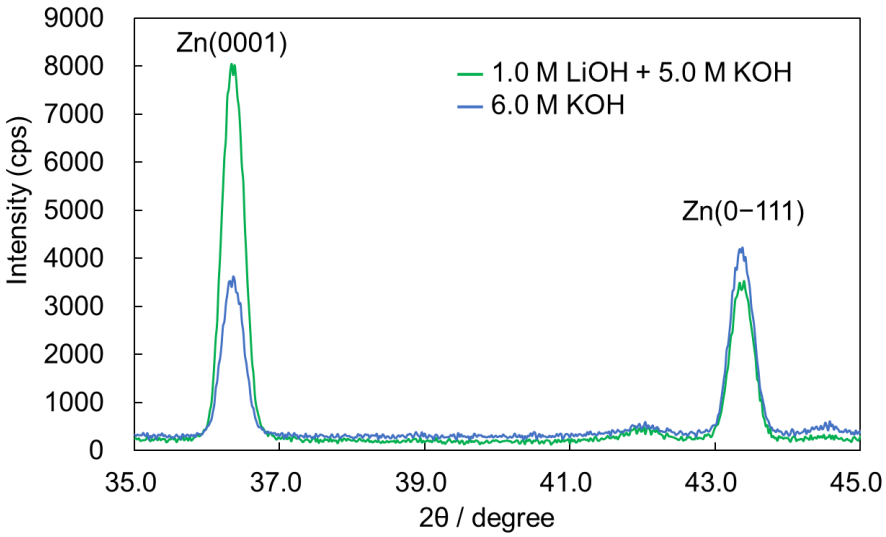

Figure 4.6. XRD patterns of the electrodeposited Zn at 0.5 C cm^{-2}. Blue and green lines indicate the patterns obtained from 6.0 M KOH solution and 1.0 M LiOH + 5.0 M KOH, respectively.

Figure 4.7 shows a chronopotentiogram during the galvanostatic electrodeposition of Zn in the Li^+ and K^+ addition. These profiles correspond to the condition of Figure 4.4(a) and (b). Although the overpotential profiles exhibit the similar trend, a slight increase in overpotential was observed in the K^+ condition while not in the Li^+ condition. It is still unclear that this difference in the potential profiles is due to the change of the deposition behavior. In order to connect the morphological change and the electrochemical analysis, the electrochemical impedance spectroscopy that can give the information of the change at the interface will provide valuable insight.

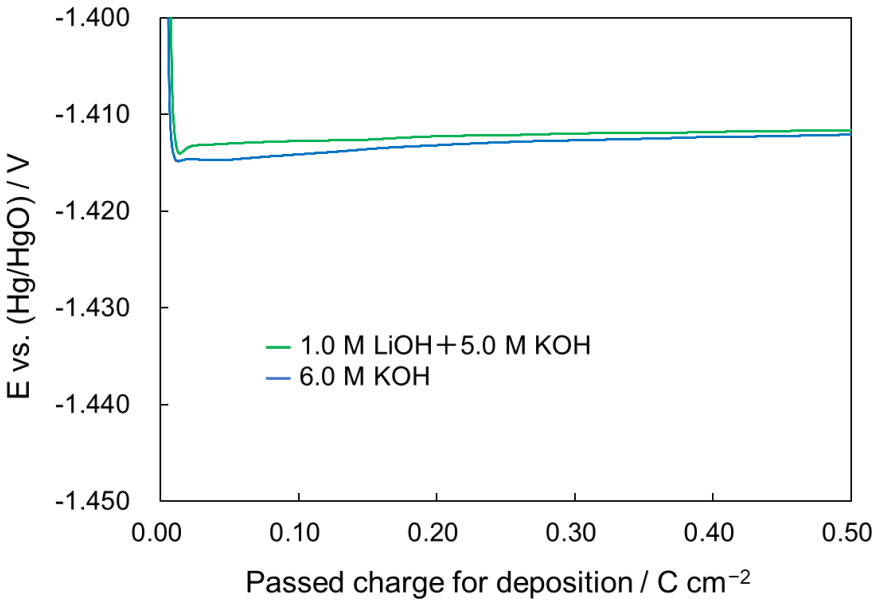

Figure 4.7. Chronopotentiograms measured during galvanostatic Zn electrodeposition in the condition of 6.0 M KOH (blue line) and 1.0 M LiOH + 5.0 M KOH (green line). Current density was −1.0 mA cm^{-2} and total passed charge was 0.5 C cm^{-2}.

Based on these simulation and experimental results, a mechanism of the Li^+ effect can be proposed in Zn electrodeposition based on the characteristics of Li^+. Since Li^+ strongly interacts with water molecules, the solvation of Li^+ is rigid and water molecules are less oriented in favor of interaction with the deposited adatoms and surfaces. This reduces the density of water molecules near the surface compared to the K^+ condition. Therefore, the solvation effect observed in the K^+ condition is mitigated near the more open facets in the Li^+ condition. This results in a difference in interlayer diffusion rates between K^+ and Li^+, with interlayer diffusion occurring more rapid with the addition of Li^+. This adatom behavior causes layer-by-layer structures to grow preferentially on the substrate. It is experimentally confirmed that the Li^+ condition produces Zn shape evolution with a different crystal structure and microstructure from that in the K^+ condition, and that the generation of mossy structures is somehow delayed by such a mechanism.

Conclusions

In this chapter, the effect of Li^+ addition on the shape evolution at the early stage of Zn electrodeposition was analyzed to investigate the effect of the additive that works near the surface. Due to the strong interaction of Li^+ with water molecules, water molecules hardly change their orientation to interact with surfaces and adatoms. This effect causes the decrease of the density of water molecules near the surface, and the mitigation of the solvation effect for the surface diffusion on open facets such as the interlayer diffusion. On the other hand, it was also suggested that more detailed understanding could be achieved by examining effects other than electrostatic interactions. In particular, the solvation effect of the interruption of the surface diffusion is reduced, and the diffusion becomes more rapid in the Li^+ condition in this simulation. The experiments also suggest that this rapid interlayer diffusion alters the growth of layer-by-layer structures in the early stage of electrodeposition. Compared to the K^+ condition, the layer-by-layer structure growth is expanded more in the Li^+ condition, confirming the correspondence between the experiment and simulation. The clarification of the mechanism of the effect from the liquid phase on the surface diffusion and on the deposition behavior is expected to make a progress for further understanding of the Zn electrodeposition mechanism. In particular, the mechanism of the influence of Li^+ on the phenomena at the surface obtained by the results of this chapter can lead to the design of new additives in the future, analyzing the effect of Li^+ as a typical example.

References

[1] L. Oniciu, L. Muresan, Some Fundamental Aspects of Levelling and Brightening in Metal Electrodeposition, *J. Appl. Electrochem.* 21 (1991) 565-574.

[2] C. W. Lee, K. Ssthiyanarayanan, S. W. Eom, H. S. Kim, M. S. Yun, Novel Electrochemical Behavior of Zinc Anodes in Zinc/air Batteries in the Presence of Additives, *J. Power Sources* 159 (2006) 1474-1477.

[3] M. Shimizu, K. Hirahara, S. Arai, Morphology Control of Zinc Electrodeposition by Surfactant Addition for Alkaline-based Rechargeable Batteries, *Phys. Chem. Chem. Phys.* 21 (2019) 7045-7052.

[4] M. Kim, D. Yun, J. Jeon, Effect of a Bromine Complex Agent on Electrochemical Performances of Zinc Electrodeposition and Electrodissolution in Zinc–bromide Flow Battery, *J. Power Sources* 438 (2019) 227020.

[5] K. Miyazaki, A. Nakata, Y.-S. Lee, T. Fukutsuka, T. Abe, "nfluence of Surfactants as Additives to Electrolyte Solutions on Zinc Electrodeposition and Potential Oscillation Behavior, *J. Appl. Electrochem.* 46 (2016) 1067-1073.

[6] K. Nayana, T. Venkatesha, Synergistic Effects of Additives on Morphology, Texture and Discharge Mechanism of Zinc during Electrodeposition, *J. Electroanal. Chem.* 663 (2011) 98-107.

[7] J. Zhu, Y. Zhou, C. Gao, Influence of Surfactants on Electrochemical Behavior of Zinc Electrodes in Alkaline Solution, *J. Power Sources* 72 (1998) 231-235.

[8] A. Bayaguud, X. Luo, Y. Fu, C. Zhu, Cationic Surfactant-Type Electrolyte Additive Enables Three-Dimensional Dendrite-Free Zinc Anode for Stable Zinc-Ion Batteries, *ACS Energy Lett.* 5 (2020) 3012-3020.

[9] M. Xu, D. Ivey, W. Qu, Z. Xie, Study of the Mechanism for Electrodeposition of Dendrite-free Zinc in an Alkaline Electrolyte Modified with 1-ethyl-3-methylimidazolium Dicyanamide, *J. Power Sources* 274 (2015) 1249-1253.

[10] Y. Li, P. Wu, W. Zhong, C. Xie, Y. Xie, Q. Zhang, D. Sun, Y. Tang, H. Wang, Progressive Nucleation Mechanism Enables Stable Zinc Stripping Plating Behavior, *Energy Environ. Sci.* 14 (2021) 5563-5571.

[11] R. Y. Wang, D. W. Kirk, G. X. Zhang, Effects of Deposition Conditions on the Morphology of Zinc Deposits from Alkaline Zincate Solutions, *J. Electrochem. Soc.* 153

(2006) C357-C364.

[12] K. Fukumoto, S. Oue, T. Niwa, Y. Kikuchi, S. Akamatsu, H. Nakano, Effect of Organic Additives on Electrodeposition Behavior of Zn from Zincate Solution Containing Potassium Hydroxide and Its Micro Structure, *Mater. Trans.* 62 (2021) 807-814.

[13] P. Thakur, K. Alam, A. Roy, C. Downing, V. Nicolosi, P. Sen, T. N. Narayanan, Extending the Cyclability of Alkaline Zinc−Air Batteries: Synergistic Roles of Li^+ and K^+ Ions in Electrodics, *ACS Appl. Mater. Interfaces* 13 (2021) 33112-33122.

[14] X. Guo, Z. Zhang, J. Li, N. Luo, G.-L. Chai, T. S. Miller, F. Lai, P. Shearing, D. J. L. Brett, D. Han, Z. Weng, G. He, I. P. Parkin, Alleviation of Dendrite Formation on Zinc Alleviation of Dendrite Formation on Zinc Anodes via Electrolyte Additives, *ACS Energy Lett.* 6 (2021) 395-403.

[15] T. Otani, T. Yasuda, M. Kunimoto, M. Yanagisawa, Y. Fukunaka, T. Homma, Effect of Li^+ Addition on Growth Behavior of ZnO during Anodic Dissolution of Zn Negative Electrode, *Electrochim. Acta* 305 (2019) 90-100.

[16] M. Nakamura, Y. Nakajima, N. Hoshi, H. Tajiri, O. Sakata, Effect of Non-Specifically Adsorbed Ions on the Surface Oxidation of Pt(111), *ChemPhysChem* 14 (2013) 2426-2431.

[17] F. Hirata, P. J. Rossky, An Extended RISM Equation for Molecular Polar Fluids, *Chem. Phys. Lett.* 83 (1981) 329-334.

[18] S. Nishihara, M. Otani, Hybrid Solvation Models for Bulk, Interface, and Membrane: Reference Interaction Site Methods Coupled with Density Functional Theory, *Phys. Rev. B* 96 (2017) 115429.

[19] P. Giannozzi, S. Baroni, N. Bonini, M. Calandra, R. Car, C. Cavazzoni, D. Ceresoli, G. L. Chiarotti, M. Cococcioni, I. Dabo et al., QUANTUM ESPRESSO: a Modular and Open-Source Software Project for Quantum Simulations of Materials, *J. Phys.: Condens. Mater.* 21 (2009) 395502.

[20] P. Giannozzi, O. Andreussi, T. Brumme, O. Bunau, M. B. Nardelli, M. Calandra, R. Car, C. Cavazzoni, D. Ceresoli, M. Cococcioni et al., Advanced Capabilities for Materials Modeling with QUANTUM ESPRESSO, *J. Phys.: Condens. Matter* 29 (2017) 465901.

[21] W. L. Jorgensen, J. Tirado-Rives, The OPLS Potential Functions for Proteins. Energy Minimizations for Crystals of Cyclic Peptides and Crambin, *J. Am. Chem. Soc.* 110 (1988)

1657-1666.

[22] W. L. Jorgensen, D. S. Maxwell, J. Tirado-Rives, Development and Testing of the OPLS All-Atom Force Field on Conformational Energetics and Properties of Organic Liquids, *J. Am. Chem. Soc.* 118 (1996) 11225-11236.

[23] T. Otani, M. Nagata, Y. Fukunaka, T. Homma, Morphological Evolution of Mossy Structures during the Electrodeposition of Zinc from an Alkaline Zincate Solution, *Electrochim. Acta* 206 (2016) 366-373.

[24] T. Otani, Y. Fukunaka, T. Homma, Effect of Lead and Tin Additives on Surface Morphology Evolution of Electrodeposited Zinc, *Electrochim. Acta* 242 (2017) 364-372.

[25] M. Matsunaga, Y. Ito, S. Yoshizawa, The Behavior of the Solid Zinc-Lithium Alloy Electrode in a LiCl-KCl Eutectic Melt, *DENKIKAGAKU* 48 (1980) 634-637.

[26] C. Izutani, D. Fukagawa, M. Miyasita, M. Ito, N. Sugimura, R. Aoyama, T. Gotoh, T. Shibue, Y. Igarashi, H. Oshio, The Materials Characterization Central Laboratory: An Open-Ended Laboratory Program for Fourth-Year Undergraduate and Graduate Students. *J. Chem. Educ.* 93 (2016) 1667-1670.

[27] M. A. Brown, Z. Abbas, A. Kleinbert, R. G. Green, A. Goel, S. May, T. M. Squires, , Determination of Surface Potential and Electrical Double-Layer Structure at the Aqueous Electrolyte-Nanoparticle Interface, *Phys. Rev. X* 6 (2016) 011007.

[28] G. Salitra, A. Soffer, L. Eliad, Y. Chen, D. Aurbach, Carbon Electrodes for Double-Layer Capacitors I. Relations Between Ion and Pore Dimensions, *J. Electrochem. Soc.* 147 (2000) 2486-2493.

[29] M. Aida, M. Tanaka, Influence of Alkali Metal Ion on the Solvent Water Molecules: Solvent Distribution and Orbital Interaction, *Low temperature science* 64 (2006) 21-30.

[30] K. Azumi, T. Yugiri, M. Seo, K. Tashiro, S. Kawashima, Double Zincate Pretreatment of Al Ally in a LiOH-based Zincate Solution, *J. Surf. Finish. Soc.* 51 (2000) 313-318.

[31] M. E. Taboada, D. M. Véliz, H. R. Galleguillos, T. A. Graber, Solubility, Density, Viscosity, Electrical Conductivity, and Refractive Index of Saturated Solutions of Lithium Hydroxide in Water + Ethanol, *J. Chem. Eng. Data* 50 (2005) 187-190.

Chapter 5:

Deposition Behavior of Zn Atom with Pb Additive Electrodeposition

5.1. Introduction

In Chapter 4, the additive of Li^+ was focused on as an additive that exhibits its effect from the solution side at the solid-liquid interface. Additives show the various working mechanism for the electrodeposition. However, the analysis of the effect of additives at molecular level is still difficult due to the complicated condition at the solid-liquid interface. Hence, in addition to the analysis for the solution side, it is important to clarify the working mechanisms of additives that deposit earlier than the main deposits on the surface and exhibit their effects.

As for the additives that can show their effect on the surface with the earlier deposition, metal additives have been attracting attention to avoid the irregular shape evolutions including the mossy structures and dendrites. For its suppression of both dendrite and mossy structures, the use of metal additives such as Pb, Sn, and Bi, which electrodeposit at more positive deposition potentials than Zn, has been considered. It has been suggested that Sn [1-3] and Bi [4-6] have the effect of changing the crystal structure and morphology of the electrodeposited Zn on the substrate. In particular, Pb addition has been shown to give characteristic nano-level Zn shape evolution at low current densities [7-9]. Previous studies have also suggested that Pb has little effect on the charge transfer process of Zn deposition, even if the deposition potential of Zn during electrodeposition becomes more negative due to Pb addition [7,10]. This indicates that the analysis of the process after the charge transfer is essential for elucidating the Zn deposition behavior with Pb. Analysis of the mechanism of the effect of Pb, which suppress irregular shape evolution at both low and high current densities, would be helpful in elucidating the mechanism of the effect of additive species on the surface. However, in electrodeposition with additives, it is challenging to understand the nanoscale phenomena. Since the deposition of the metal additive proceeds before the deposition of Zn, the behavior of Zn on such additive is significant.

In this chapter, density functional theory (DFT) calculations based on the first-principles calculations are performed in addition to the electrochemical measurements that analyze Zn crystal growth to clarify the mechanism of deposited Zn atom behavior

during the electrodeposition in the presence of trace amount of Pb. This analysis will provide a micro- and nanoscale understanding of the mechanism of additive action in electrodeposition.

5.2. Methods

5.2.1. Zn electrodeposition with the Pb addition

Zn electrodeposition on the negative electrode was performed with alkaline zincate solution. Two types of solution were prepared: one contained 1.0 mmol dm^{-3} PbO (Kanto Chemical, Cica-reagent grade, >99.9%) + 6.0 mol dm^{-3} KOH (Kanto Chemical, Cica-reagent grade) + 0.1 mol dm^{-3} ZnO (Kanto Chemical, Cica-reagent grade), and the other 6.0 mol dm^{-3} KOH + 0.1 mol dm^{-3} ZnO. For adjusting the Pb solution, PbO was dissolved into 48 wt% of KOH solution, and the ZnO dissolved into the solution. All solutions were deaerated by nitrogen bubbles before electrochemical measurements. According to the Pourbaix diagram, the stable state of PbO in the high pH solution is $Pb(OH)_3^-$ [11]. All solutions were deaerated by bubbling nitrogen before electrochemical measurements for 10 min.

Electrochemical measurements were performed using a three-electrodes system. Cu plate prepared by chemical mechanical polishing was used as the working electrode. This Cu plate was mirror finished by automatic lapping polishing machine (MA-400D, Musashino Denshi Co., Ltd.) with polishing slurry mainly based on ultrahigh purity colloidal silica (PLANERLITE-7101, Fujimi Incorporated). For the cross sectional scanning electron microscopy (SEM), the alternative working electrode was used as Cu (100nm)/Cr (10 nm) layer on Si(111) wafer prepared by electron beam evaporation (ULVAC, EBX-6D). The working electrode was placed horizontally at the bottom of the cell facing upward to the reference electrode to prevent the influence of the undesirable natural convection near the electrode that causes nonuniform deposition along the vertical direction. Hg/HgO (Inter Chemie. Inc.) was utilized as the reference electrode. Zn wire

(Nilaco, 99.99%) was utilized as the counter electrode, which was wrapped around the pipe of the reference electrode.

The Cu working electrode was immersed in 45.0 mL ultrapure water (18.2 MΩ cm) + 5.0 mL 96 wt% of sulfuric acid for 30 s, and the Zn counter electrode was immersed in 180 mL pure water + 20.0 mL 96 wt% of sulfuric acid for 10 s before the electrochemical measurements. After surface treatment, the electrodes were rinsed with pure water and dried in N_2 air.

All electrodeposition processes were performed using an electrochemical measurement system (HZ-7000, Hokuto Denko) at room temperature (23 °C). The current densities of all galvanostatic electrodepositions were set to −5.0 mA cm^{-2}. The surface morphology of the electrodeposited Zn was observed using scanning electron microscopy (SEM, SU-8240). The crystal structure of the deposit was analyzed in the out-of-plane and in-plane directions using an X-ray diffractometer (XRD, Rigaku, Rint-Ultima III) at the Materials Characterization Central Laboratory, Waseda University [12].

5.2.2. DFT calculations for the deposited Zn atom with co-deposited Pb atomic layers

DFT calculations in this chapter are also performed by Quantum ESPRESSO code [13,14] that the RISM component is implemented by Nishihara [15]. Kohn–Sham equations [16] were solved using a plane-wave basis within the ultrasoft pseudopotential framework [17,18]. The cutoff energies for the wave functions and augmented charge were set to 40 and 320 Ry, respectively. The Perdew–Burke–Ernzerhof form of the generalized gradient approximation was used to calculate the exchange correlation energies [19]. A unit cell was sampled with Monkhorst–Pack k-point grids [20] of 2 × 2 × 1. Geometrical optimizations were performed with convergence thresholds of 10^{-4} Ry and 10^{-3} Ry/Bohr for energy and force, respectively. ESM-RISM was used to reproduce the electrochemical solid–liquid interface [15,21] as well as the other chapters. The Kovalenko–Hirata closure model was used for the Laue-RISM calculations [22], which is a mixed boundary condition calculation in which the supercell only expands in the *x*- and *y*-directions. The electrolyte condition was assumed to be a 6.0 M KOH solution. The

simple point charge model was used for the classical force field parameter of water [23], and the optimized potential for liquid simulation was selected for the parameters of K^+ and OH^- [24,25]. The temperature was set at 300 K. Lennard–Jones parameters (ε, σ) were set to (0.790 kcal mol^{-1}, 3.46 Å) for Zn, which is identical to the previous chapters, and (2.93 kcal mol^{-1}, 3.18 Å) for Pb [26], respectively. The kinetic energy cutoff for the solvent correlation functions of the RISM components was set at 144 Ry, and the convergence thresholds for one-dimensional and three-dimensional RISM were set at 10^{-8} and 10^{-5} Ry, respectively.

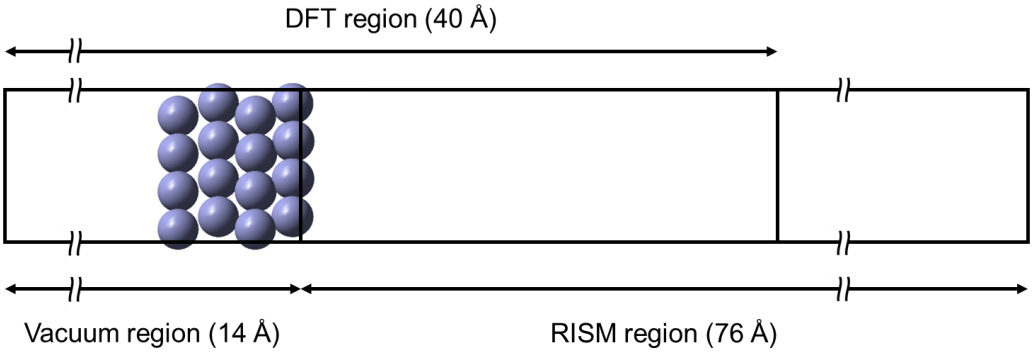

Figure 5.1. Slab model of the Zn(0001) surface. Z axis is directed to the righthand side. All balls show the Zn atom. The right side of the slab is used as the surface where the deposited atoms adsorb.

A slab model consisting of four atomic layers with 64 atoms of the Zn(0001) surface was constructed based on the Zn hexagonal close-packed (hcp) structure as shown in Figure 5.1. The deposited Pb layers on the Zn(0001) surface was optimized to evaluate Pb alignment on the Zn surface by modelling the structure based on the experiments. The behavior of deposited Zn atoms was analyzed by optimizing the incorporation of deposited Zn atoms into defects of the Pb layer. The relative energies, ΔE, were calculated by subtracting the total energy of the system of the deposited Zn atom located at the position near the solution side, E_{outer}, from that at the position near the Zn slab side, E_{inner}, namely, $\Delta E = E_{inner} - E_{outer}$. If ΔE is negative, the elementary step assumed can proceed thermodynamically. In addition, the charge of the calculation models was set as neutral, since deposited Zn atoms on the surface appear after the charge transfer process that is the reduction of zincate ion, $Zn(OH)_4^{2-}$.

5.3. Results and Discussion

5.3.1. Crystal structures of the Zn electrodeposits with the Pb addition

The galvanostatic electrodeposition of Zn is performed without and with the Pb addition at low current density (−5.0 mA cm^{-2}) to analyze the Pb effect at the initial stage of the Zn shape evolution. The deposits are observed without and with the Pb addition after the galvanostatic deposition of the passed charge of 0.25 C cm^{-2} (−5.0 mA cm^{-2} for 50 s) (Figure 5.2(a) and (b)). In the case without Pb addition, a layer-by-layer structures are observed. This is similar to the morphology reported in the previous study [7,27,28], which can be the initial shape of the Zn electrodeposits at low current density. In contrast, when Pb is added, hexagon-like structures are observed. The electrodeposits are also observed cross-sectionally after the electrodeposition without Pb addition for passed charge of 1.0 C cm^{-2} and 2.0 C cm^{-2} (−5.0 mA cm^{-2} for 200 s and 400 s) (Figure 5.3(a)-(d)). It was found that dense Zn is deposited on the substrate in the case without Pb addition. On the other hand, the pillar-like structures are observed as the growing shape of the initial fine hexagonal electrodeposits. The height of the pillar-like structures is almost 500 nm after the electrodeposition passed charge of 2.0 C cm^{-2}. It is indicated that the pillar-like structures are elongated with respect to the increase of the passed charge.

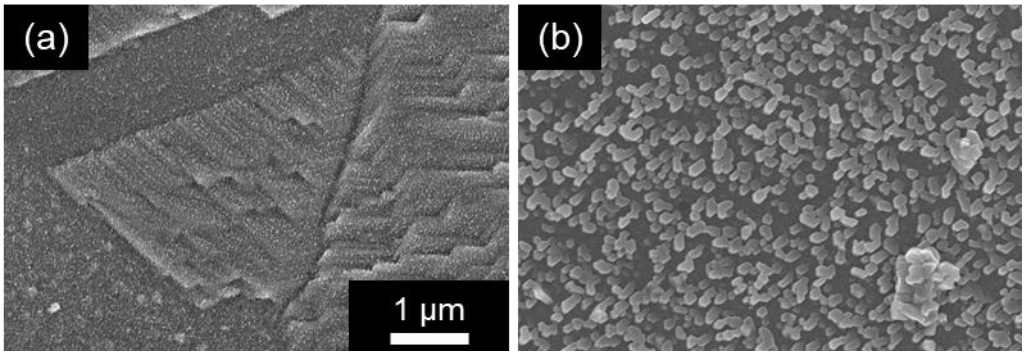

Figure 5.2. SEM images of the Zn morphology after the Zn galvanostatic electrodeposition that passed charge is set at 0.25 C cm^{-2} (at −5.0 mA cm^{-2} for 50 s): (a) without Pb, (b) with Pb. Both images are taken at the same scale.

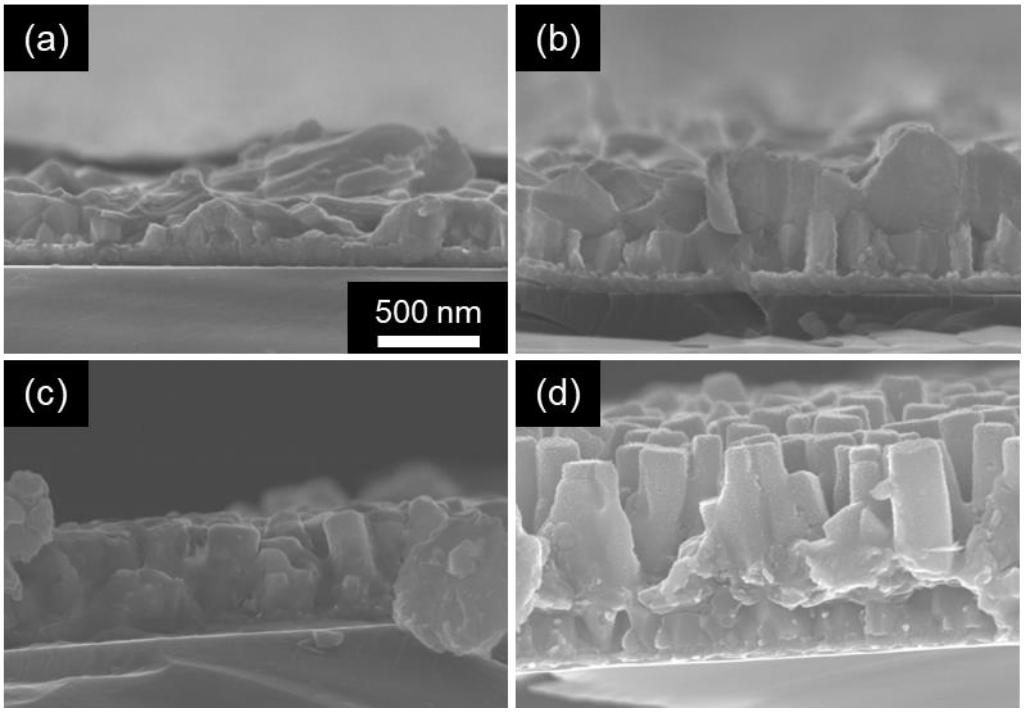

Figure 5.3. Cross-sectional images of the of the Zn morphology after Zn galvanostatic electrodeposition at −5.0 mA cm^{-2}: (a) without Pb at 1.0 C cm^{-2} (for 200 s); (b) without Pb at 2.0 C cm^{-2} (for 400 s); (c) with Pb at 1.0 C cm^{-2} (for 200 s); and (d) with Pb at 2.0 C cm^{-2} (for 400 s). All images were taken at the same scale.

The pillar-like structures were obtained under the Pb-added condition. It is important to identify whether the deposition of the pillar continuously proceed without Pb once the pillar appears on the surface because the timing when Pb influences the Zn deposition should be understood. Hence, two-step electrodeposition is performed with changing the solution at the first step and the second step to clarify that the pillar-like structures grow only in the presence of Pb. In the first step, galvanostatic electrodeposition with the solution with the Pb addition is carried out for passed charge of 1.0 C cm^{-2} (for 200 s) to deposit the pillar-like structures, and then the solution is changed to the one without the Pb addition followed by the electrodeposition of the second step after the cell was rinsed twice by the solution used in the second step. The electrodeposits obtained after these two steps are observed (Figure 5.4(a)-(d)). A large hexagonal boulder-like structure is deposited on top of the pillar-like structures. In addition, the side views of the deposits show that the pillar-like structures have grown non-uniformly and are generally shorter

than those in Figure 5.3(d) which shows the structures at the same amount of passed charge. The boulder-like structures are about 100 times larger than diameter of a pillar-like structure, suggesting that Zn is electrodeposited in these boulder-like structures in this second step. The same two-step electrodeposition was carried out using a solution with Pb in both first and second steps (Figure 5.5). The pillar-like structures are observed as same as the single-step electrodeposition with the Pb addition. This indicates that the pillar-like structures of Zn are only deposited with the co-deposition with Pb.

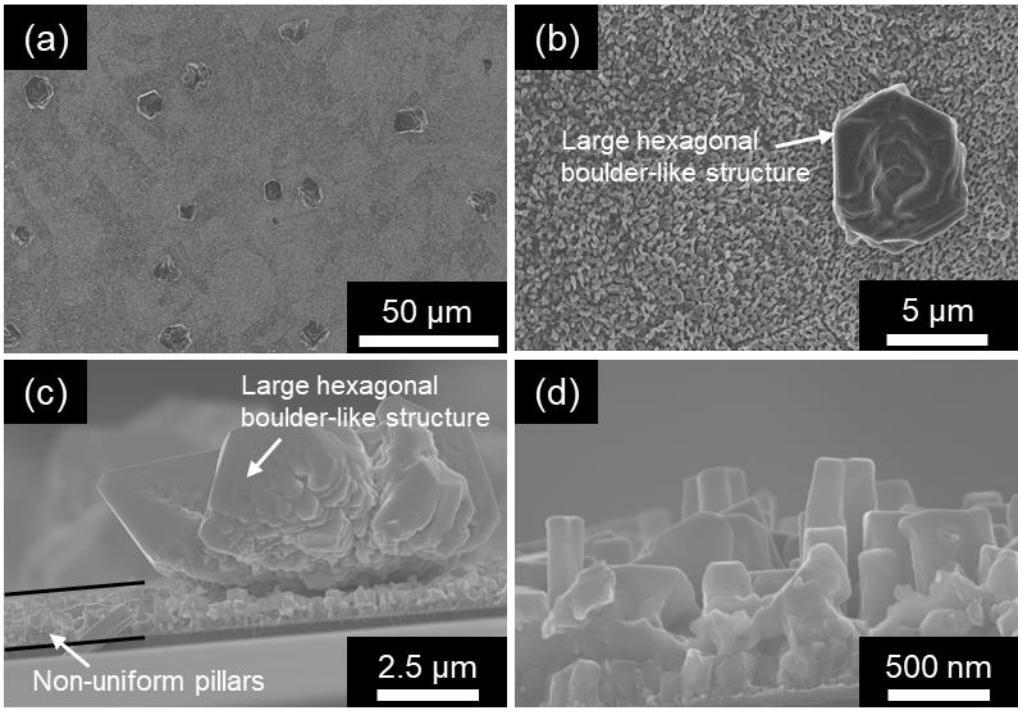

Figure 5.4. SEM images of the Zn morphology after the two-step galvanostatic electrodeposition at −5.0 mA cm^{-2} composing of the first-step electrodeposition with Pb for passed charge of 1.0 C cm^{-2} (for 200 s) and the second-step electrodeposition without Pb for passed charge of 2.0 C cm^{-2} (for 200 s). (b) is the magnified image of (a). (c) is a cross-sectional image of the boulder-like structure. (d) is a cross-sectional image of the pillar-like structures after the two-step electrodeposition.

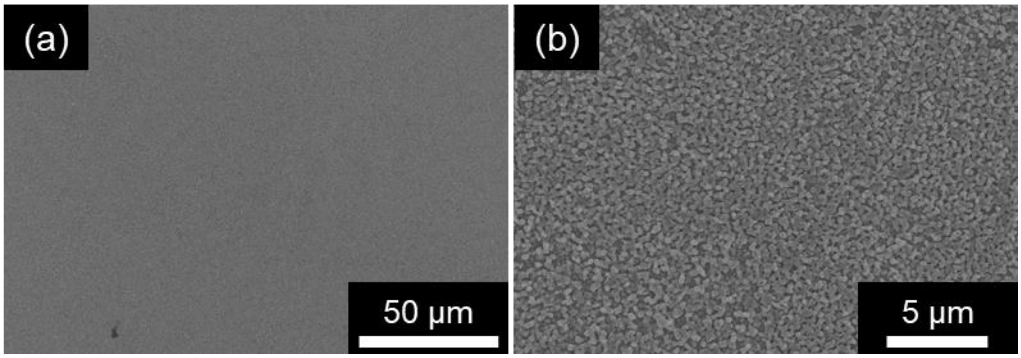

Figure 5.5. SEM images of the Zn morphology after the two-step galvanostatic electrodeposition at −5.0 mA cm^{-2} composing of the first-step electrodeposition with Pb for passed charge of 1.0 C cm^{-2} (for 200 s) and the second-step electrodeposition with Pb for passed charge of 2.0 C cm^{-2} (for 200 s). (b) is a magnified image of (a).

As for the deposition potential profile with respect to the surface condition and the solution (Figure 5.6), large overpotential is observed at the initial stage in the case without Pb on the Zn pillar-like structures, which corresponds to the condition of Figure 4. This trend is considered to be due to the overpotential required for nucleation in the initial stage of the electro-deposition [7,29]. In this case, it is considered to be the overpotential required for nucleation when the Boulder-like structures are generated on the pillar-like structures. In contrast, the potential negatively shifts smoothly in the electrodeposition on the Zn pillar used the solution with the Pb addition. This is because the pillar-like structures are deposited beforehand, and the deposition proceeds on the pillar-like structures. As the deposition proceeds, the potential shifts gradually to more negative region in this case, and it is expected that the potential will be the same as that deposited on the Cu substrate.

These results suggest that the Zn pillar-like structures need to co-deposit with Pb in order to continue to grow. Although Pb is deposited at a more positive deposition potential than Zn, which reminds a site-blocking effect for the Zn deposition caused by the earlier deposition of Pb on the substrate surface, the co-deposition of Zn and Pb is significant for the growth of this pillar-like structures, rather than the site-blocking effect by such earlier deposition of Pb.

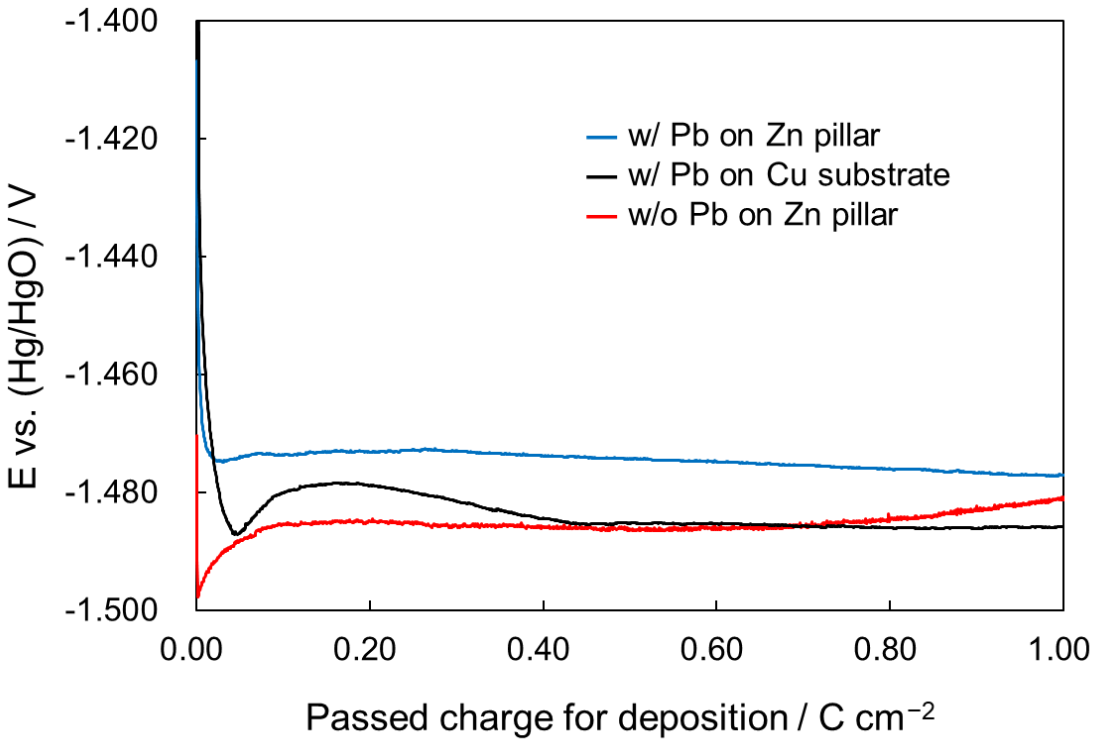

Figure 5.6. Chronopotentiogram of the galvanostatic deposition of Zn with respect to the substrate conditions. Blue line shows the profile during the electrodeposition with the Pb addition on the Zn pillar deposited by the first step electrodeposition with Pb addition. Red line shows the profile during the electrodeposition without the Pb addition on the Zn pillar deposited by the first step electrodeposition with Pb addition. Black line shows the profile during the electrodeposition with Pb addition on the polished Cu plate. Current density was −5.0 mA cm^{-2} and deposition time was 200 s in all electrodepositions. Passed charge was set at 1.0 C cm^{-2}.

In order to analyze the crystal structure of the pillar-like structures, XRD measurements were carried out on the electrodeposited film with the pillar-like structures. The crystal plane whose normal vector is perpendicular to the substrate is characterized by out-of-plane measurement (Figure 5.7(a)). An hcp-Zn(0001) peak is observed at 36°, which is overlapped with Pb(200). The existence of Pb(200) is difficult to confirm because the intensity derived from Zn is much larger than that of Pb(200). A peak around 43° shows hcp-Zn(0−111), which overlaps face-centered cubic (fcc) -Cu(111) peak of the Cu substrate. This peak mainly originates from the Cu substrate because the peak intensity

does not change with the passed charge. A peak at around 42° is probably due to Zn corrosion products or Zn-Cu alloys based on the previous study [30,31]. A peak derived from an fcc-Pb(111) appeared at approximately 31°, indicating the co-deposition of Pb. This suggests that Pb(111) may be present in the upper part of the pillar-like structures. The crystal structures oriented perpendicular to the substrate were evaluated using in-plane XRD measurements (Figure 5.7(b)). An hcp-Zn(0−110) peak at 39° was observed as a characteristic peak of the sidewalls of the pillar structures. This peak was not observed in Figure. 5.7(a) or in the XRD patterns of the electrodeposited Zn films without the Pb addition [27]. Moreover, an fcc-Pb(111) peak at 31° was observed, suggesting that Pb was also present at the sidewalls of the pillar-like structures in the (111) orientation. Peaks derived from the (0001) or Pb(200) and (0−111) facets of hcp-Zn were also observed. Peak at 36° may be attributed to Pb(200) because of the existence of the Pb(111) on the top layer. If this is derived from Zn(0001), the decrease of these peaks with respect to the increase of the amount of passed charge was caused by the growth of the pillar-like structures in the vertical direction to the substrate. These results indicates that the Zn pillar-like structures grow in the [0001] direction, while the sidewalls are oriented to the (0−110) plane. In addition, there is a possibility that Pb(111) is formed at both the top and side of the pillars.

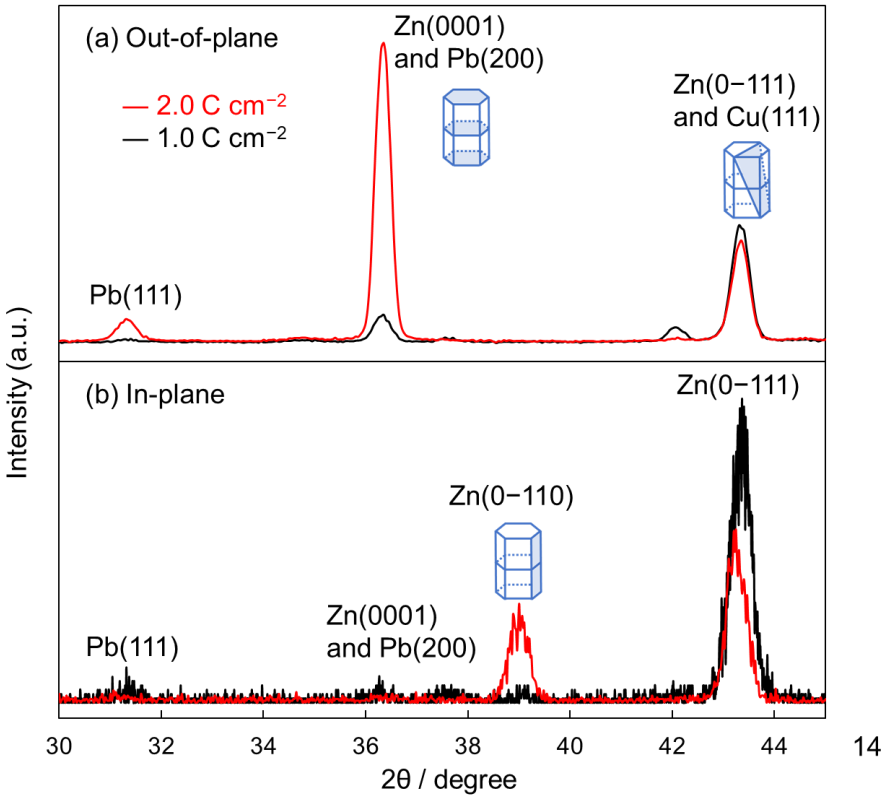

Figure 5.7. XRD patterns of electrodeposited Zn with Pb addition at 1.0 (black line) and 2.0 C cm^{-2} (red line): (a) out-of-plane and (b) in-plane.

5.3.2. Behavior of the deposited Zn atom at the Pb layer on the Zn surface

In conjunction with the above results, previous study suggested that the Pb content of the Zn electrodeposit with 1.0 mM Pb addition is approximately 1% [35]. Although the heat of sublimation of Zn is lower than that of Pb (115 kJ mol^{-1} for Zn and 179.5 kJ mol^{-1} for Pb), the surface energy of the Zn(0001) plane is lower than that of the Pb(111) plane calculated by the equivalent crystal theory (0.32 J m^{-2} for Zn and 0.27 J m^{-2} for Pb) [36]. This suggests that Pb may be present on the surface by forming a layer on the topmost surface due to the difference in surface energy. Hence, it is hypothesized that the Pb layer exists on the Zn pillars. The other possibilities will be discussed in the later section. The Pb behavior on the Zn surface should be clarified at the atomic scale. Based on these, Pb structures are optimized on the Zn(0001) surface by DFT calculations to identify the

presence of Pb on the Zn surface. Structural optimization of a Pb layer on the Zn(0001) surface is carried out shown in Figure 5.8.

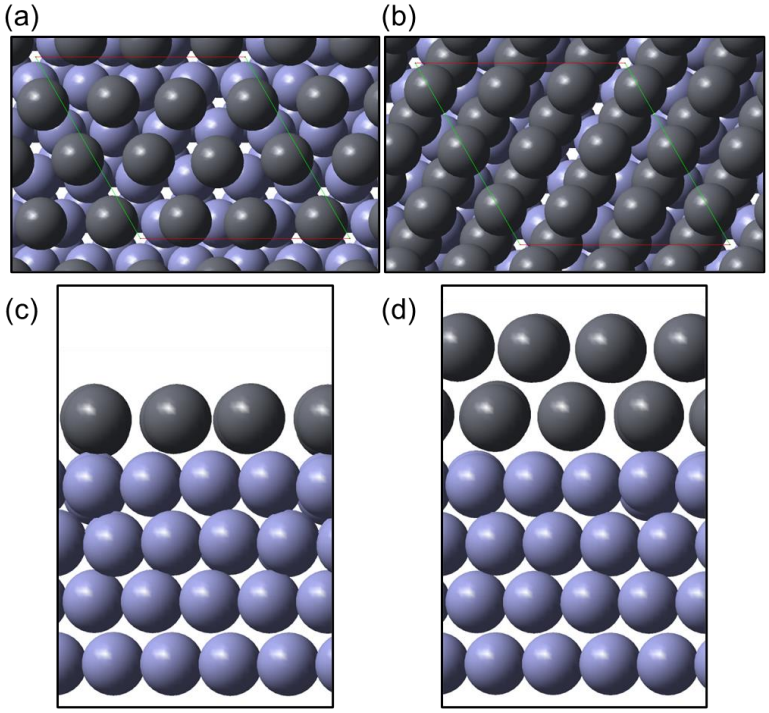

Figure 5.8. Optimized structures of the Zn(0001) surface covered with the Pb layer: top views of the Zn surface (a) with a single Pb layer, (b) with a double Pb layers. (c) and (d) are the side views of (a) and (b), respectively. Purple and gray balls show the Zn and Pb atoms, respectively. Green and red lines in (a) and (b) indicate the area of the supercell.

The result shows that the Pb layer is stable with nine Pb atoms per sixteen Zn atoms of the Zn(0001) surface, suggesting that Pb covers the Zn surface. The Pb atoms align similar to the (111) facet. The average bond length between adjacent Pb atoms in this structure is 3.56 Å. That of the Pb(111) plane is 3.50 Å. The structure with double Pb layers is also optimized shown in Figure 5.8(b), and it is indicated that the Pb atoms are arranged similar to the (111) facet as well as the case with the single Pb layer. In combination with the triangular structures formed by the Pb atoms, it is suggested that Pb forms a structure similar to the (111) facet on the surface. These calculations are in a good agreement with the results obtained by the XRD measurements. Therefore, it can be one of the possibilities from both the experimental and theoretical results suggest that Pb(111) covers the Zn surface because of the low surface energy of Pb(111). In addition, the formation of this Pb layer may change the underpotential deposition (UPD) behavior of

Zn at a less negative applied potential owing to the prior deposition of Pb on the substrate. Metal–metal interactions are important in the behavior of UPD, and the interaction between Pb and Zn can be different from that between the substrate metal and Zn. In particular, as shown in Figure 5.8, the DFT results indicate that Pb deposits on the Zn metal and attaches the solution side during the co-deposition of Pb and Zn. Zn cannot form the alloy with Pb. This suggests that the interaction between Pb and Zn is not enough strong to form the UPD layer on Pb layers. Hence, the occurrence of Zn UPD is difficult when Zn is co-deposited with Pb. However, the mechanism of the Zn continuous deposition in the presence of Pb layers on top of the Zn surface remains unclear.

The behavior of Zn atoms under the condition that the Pb(111) plane covers Zn surface is analyzed to elucidate the significant characteristics of Pb and Zn, which lead to the continuous deposition of bulk Zn. The adsorption of a deposited Zn atom on the Zn surface covered with a single Pb layer is structurally optimized shown in Figures 5.9(a) and (c). It is found that the deposited Zn atom adsorbs close to the hollow site of the Pb layer. The incorporation structures of the deposited Zn atom on the Zn layer after the penetration through the Pb layer was optimized and shown in Figures 5.9(b) and (d). The deposited Zn atom attaches on the hollow-hcp site of the Zn layer. The calculated relative energy, ΔE, compared to that of the adsorption of the Zn atom on the Pb layer was −64.7 kJ mol^{-1}. This indicates that the deposited Zn atom is thermodynamically more stable with attaching on the Zn layer than on the Pb layer.

The incorporation behavior of the deposited Zn atom inside the Pb layer is investigated for understanding of the migration of the Zn atom. The results of incorporation of the deposited Zn atoms on double Pb layers are shown in Figures 5.10(a) and (c). The Pb defect was introduced to model the co-deposition of Zn and Pb. The Zn atom is incorporated into the defect, and then the Zn atom is exchanged with the Pb atom of the inside Pb layer. The energy difference, ΔE, is −8.41 kJ mol^{-1}, suggesting that the deposited Zn atoms are thermodynamically able to migrate into the interior and reach the Zn layer. This incorporation is mainly due to the difference in surface energy between the Pb(111) and Zn(0001) facets. The exposure of Pb stabilizes the system and results in the incorporation of Zn into the interior. The difference in the surface energy allows the deposited Zn atoms to reach the interior. This indicates that Zn continues to deposit as a metal even in the presence of the Pb layers on the Zn surface. For further understanding of the Zn atom behavior, the pathway of the migration inside the Pb layer should be analyzed. One of the strategies to model is introducing the two defects in both top and bottom layers. The potential curve of the migration of the Zn atom inside the Pb layer will lead to the further understanding of its behavior.

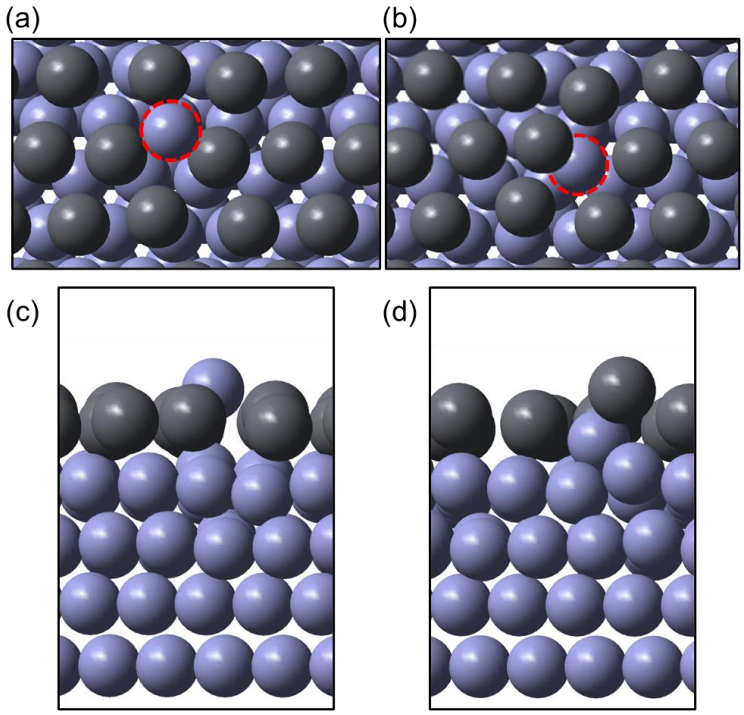

Figure 5.9. Optimized structures of the deposited Zn atom on the Zn(0001) surface covered with the single Pb layers: top views of (a) the adsorption structure and (b) the incorporation structure of the deposited Zn atom with the Pb layer on Zn metal. (c) and (d) are the side views of (a) and (b), respectively. Ball colors indicate the same elements as Figure 5.10. Red dotted circles show the deposited Zn atoms.

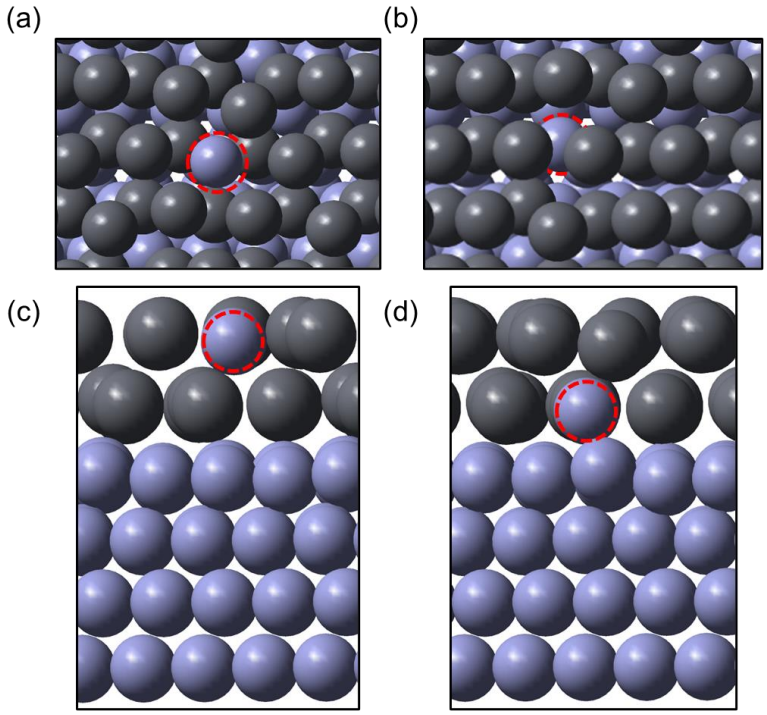

Figure 5.10. Optimized structures of the incorporation of the deposited Zn atom into the defect of the double Pb layers on the Zn(0001) surface: top views of incorporation into (a) the surface layer and (b) the inside layer. (c) and (d) are the side views of (a) and (b), respectively. Ball colors indicate the same elements as Figure 5.10. Red dotted circles in (a) and (b) show the deposited Zn atoms.

These results suggest the deposition mechanism of continuous Zn growth if deposited Pb is present on the Zn surface. First, Pb was electrodeposited, followed by Zn. This deposition order is based on the difference in deposition potential between Pb and Zn. During co-deposition of Pb and Zn, Pb forms a (111) layer, into which Zn is incorporated. The continuous incorporation of the deposited Zn atoms allowed for the continuous growth of the pillars so that the Pb layer covers the top layer. This behavior of Zn and Pb is due to the difference in surface energy of the plane. This mechanism is useful for studying the working mechanism of additive species that exhibit effects at the surface.

The Pb covering layer can be a factor for the evolution of the Zn pillar-like structures. It can be considered that this Pb deposit can cover the (0−110) plane, which inhibits the deposition of Zn on the plane. The overpotential during the Zn electrodeposition with the Pb addition is increased and negatively shifted from the pure Zn electrodeposition as

compared with the results in Chapter 4. Hence, there is a possibility that Pb layer inhibits the deposition on the (0−110) plane and the surface area of the Zn deposition is decreased. In order to clarify the shape evolution mechanism with the Pb addition, it is important to analyze the Zn shape evolution further with respect to the multiscale evolution. Details are described in the next section.

5.3.3. Hypotheses for Zn deposition mechanisms with Pb and verification methods

In this chapter, the behavior of Zn atom in the Pb layer on the surface was analyzed by simulation, assuming that Pb is present on the surface. It was found that Zn can go into the interior, suggesting that Zn can grow even when it is covered with the Pb layer. However, there are hypotheses that could be verified by further experimentation. They are listed below.

- The thickness of the Pb layer is different from that assumed in this study.
- Pb deposits not only on the surface but also as a single crystal, covering the entire surface (Figure 5.11(a)).
- Pb grows not only on the surface but also as a single crystal, covering only the (0−110) plane (Figure 5.11(b)).

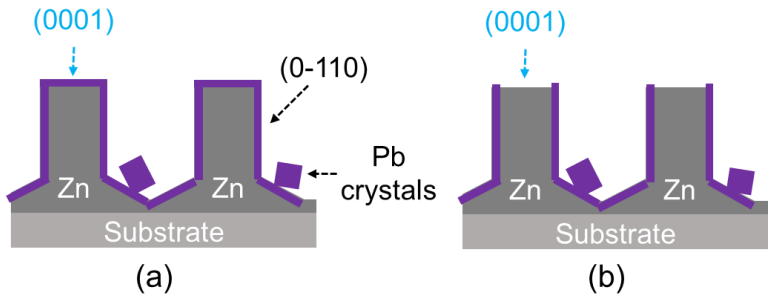

Figure 5.11. The hypotheses of the Pb deposition structures with the Zn pillars.

As for the first one, single and double Pb layers were assumed as representative

thicknesses in this study. According to the out-of-plane XRD results, the thickness is considered to be submicron meter order, and it may be worthwhile to investigate the behavior in thicker layers. On the other hand, considering the content of Pb is approximately on the order of 1%~, the Pb layer can be thinner or sparse. In the second case, the XRD result may be derived from the Pb(111) plane of the crystal. In this case, it is expected that other Pb planes will be detected. However, since the peak position of the Pb(100) plane overlaps with that of the Zn(0001) plane, it is difficult to examine, so it is effective to observe the other peaks. In the third case, the exposed Zn area is considered to be favorable for continuous deposition. X-ray photoelectron spectroscopy (XPS) is considered to be effective in verifying the distribution of Pb. Since the pillar structures of Zn are not uniformly elongated perpendicular to the substrate, it is difficult to detect the deposition on the particular orientation, although it is possible to examine the extent to which Pb is present on the exposed surface. Furthermore, in both cases, XPS measurements on the structures obtained by the two-step electrodeposition as shown in Figure 5.4 are helpful to verify whether Pb is present on the surface or not.

In all cases, the side walls of the pillar composed of the (0−110) plane is considered to be covered with Pb. A possible mechanism for the growth of the pillar-like structures is that the surface energy of the (0−110) plane is reduced by Pb. This may make the growth of the (0−110) plane slow and thus grow the pillar-like structures. One way to verify this is to compare the surface energies of the Pb-covered (0001) and (0−110) surface by the first-principles calculations. Since the supercell of the (0−110) surface as the simulation model is different from the (0001), it is necessary to examine in detail the coverage and the orientation of the Pb(111) plane that is thought to be formed on the (0−110) surface.

In the case of deposition with the hypothesis that Pb covers the (0−110) surface, the following suppression mechanism of the mossy structure by Pb is considered: The Pb layers on the surface increases the number of the reaction points by making the uncovered area working as the active sites. This allows the reaction active sites where the mossy structure can deposit to appear and react in the whole area instead of being concentrated in a certain point. It is still unclear whether the active site is on the (0001) surface or whether the deposited atom on (0−110) are incorporated into the surface and elongated in the [0001] direction. It may be necessary to analyze the difference in adsorption energy

of zincate ions on these surfaces and the behavior of Zn atoms as in the analysis performed here.

5.3.4. Expected contribution of these analyses to large-scale energy storages from these analyses

The series of the analyses thus far are expected to contribute to the development of large-scale storage batteries. There are two main points that can be expected. The first is to propose new additives to extend the practical use and life of the zinc negative electrodes, and the second is to contribute to other battery systems to improve their performance by the establishment of simulation methods, especially modelling methods.

Regarding the first point, in this dissertation, the layer-by-layer structures before the evolution of the mossy structures are simulated and the effects of additives with different working mechanisms are analyzed. This understanding will lead to the design of new additives in the future. As for the insight of the electronic structure obtained from the comparison between Zn and Cu, one guideline is to propose processes that change the electronic state of Zn such as the additives included into the Zn metal or the substrate. The result that the solvation structure affects the surface diffusion behavior, as in the case of Li^+, indicates that the parameters of surface diffusion can be adjusted by setting the solution conditions. For example, if it can be proposed the additive that shows a strong effect of solvation on the surface, increasing the activation energy of the (0001) surface diffusion is possible. This can result in the suppression of two-dimensional nucleation and suppressing the spread of the (0001) plane that appears at the bottom of the mossy structure. In addition, additives that show an effect on the surface, such as Pb, may show an effect for the control of the deposition behavior by a change in surface energy or specific adsorption. As mentioned above, if the stabilization can be achieved on a specific facet by controlling the surface energy, crystal growth of Zn can be controlled. As for an additive that shows an effect through adsorption, if it allows Zn to grow through defects as in this simulation, it may cover the specific points where nanofilaments can form and

suppress their growth. In contrast, the enhancement of the reaction on certain points can provide increase of the number of the certain points to react with, which allows the Zn precursor to gather at a specific point that can generate the mossy structures. In the other viewpoint, the clarification of the effect of Pb addition enables to aim for a Pb-free process. This is a material for considering new candidates for the electrodeposition process that could not be achieved without the use of Pb. It is thought that this will lead to an environmentally friendly process. In summary, the analysis to this point has provided knowledge for the practical use of Zn negative electrodes and the extension of the life of Zn batteries. If the Zn negative electrode can be applied in this way, it will contribute to increasing the number of options for large-scale storage batteries, and it is expected to increase the number of options for high-safety batteries.

Second, the establishment of modelling as a simulation method enables to understand the electrochemical processes related to the battery, which leads to the improvement of the battery performance by contributing to the analysis of other battery systems. The development of the KMC simulations will contribute to understanding the atomic phenomena on the other metal negative electrodes such as Li and Mg. Since the solid electrolyte interphase (SEI) is formed on the Li negative electrode, the modelling of the internal behavior of the surface, where SEI formation and other processes occur, is important. Considering the existence of such a surface layer, the results of first-principles calculations for the addition of Pb in this chapter will provide insight. The behavior of Li inside the SEI layer can be discussed if it is modelled precisely, though it shows amorphous structures which is different from the Pb layers. As analyses using molecular dynamics and other methods are reported [37], it is considered effective to combine such a method to provide the KMC parameters. This simulation can be applied to the analysis of the diffusion of Li ions into SEI. Thus, the analytical method of this study itself will help to analyze other battery systems.

It is important to utilize the results obtained from this analysis and the modelling methods as useful knowledges for the future use of Zn negative electrodes. It is expected that the combination of these simulations and experiments will lead to further development for use in renewable energy and distributed energy systems.

Conclusions

In this chapter, the crystal structure of Zn electrodeposits and the behavior of the deposited Zn atom in the presence of Pb were analyzed by the electrochemical measurements and DFT calculations. The results of these experiments and calculations suggest that the pillar-like structures only grow with the Pb-added condition, and that the deposited Zn atoms can reach the Zn metal with the defect in the Pb layers when Pb(111) covers the Zn surface. This indicates that the pillar-like structures of the electrodeposited Zn grows continuously even in the presence of the deposited Pb layers. Owing to the lower surface energy of Pb(111) compared to that of Zn(0001), Pb is more easily exposed to the solution and forms the (111) surface as the stable state. The difference in surface energies explains that the deposited Zn atoms can reach the bulk Zn and continuously grow as Zn crystals. This mechanistic understanding of the continuous Zn growth in the presence of additives on the surface provides insight into the design of more effective additives for next-generation batteries in the future, as well as the mechanism of general additives used in electrochemical deposition processes. Although Pb is not suitable for industrial use due to its toxicity, this finding can be used as an example for more efficient search and design of new additives in the future.

References

[1] F. R. McLarnon, E. J. Cairns, The Secondary Alkaline Zinc Electrode, *J. Electrochem. Soc.*, 138 (1991) 645-664.

[2] F. Mansfeld, S. Gilman, The Effect of Tin and Tetraethylammonium Ions on the Characteristics of Zinc Deposition on a Zinc Single Crystal in Aqueous KOH, *J. Electrochem. Soc.* 117 (1970) 1154-1155.

[3] H.-I. Kim, H.-C. Shin, SnO Additive for Dendritic Growth Suppression of Electrolytic Zinc, *J. Alloys Compd.* 645 (2015) 7-10.

[4] J. W. Gallaway, A. M. Gaikwad, B. Hertzberg, C. K. Erdonmez, Y.-C. K. Chen-Wiegart, L. A. Sviridov, K. Evans-Lutterodt, J. Wang, S. Banerjee, D. A. Steingartb, An In Situ Synchrotron Study of Zinc Anode Planarization by a Bismuth Additive, *J. Electrochem. Soc.* 161 (2014) A275-A284.

[5] M. Schmid, M. Willert-Porada, Zinc Particles Coated with Bismuth Oxide Based Glasses as Anode Material for Zinc Air Batteries with Improved Electrical Rechargeability, *Electrochim. Acta* 260 (2018) 246-253.

[6] J. McBreen, E. Gannon, Bismuth Oxide as an Additive in Pasted Zinc Electrodes, *J. Power Sources* 15 (1985) 169-177.

[7] T. Otani, Y. Fukunaka, T. Homma, Effect of Lead and Tin Additives on Surface Morphology Evolution of Electrodeposited Zinc, *Electrochim. Acta*, 242 (2017) 364-372.

[8] Y.-H. Wen, J. Cheng, L. Zhang, X. Yana, Y.-S. Yanga, The Inhibition of the Spongy Electrocrystallization of Zinc from Doped Flowing Alkaline Zincate Solutions, *J. Power Sources* 193 (2009) 890-894.

[9] F. Mansfeld, S. Gilman, The Effect of Lead Ions on the Dissolution and Deposition Characteristics of a Zinc Single Crystal in 6N KOH, *J. Electrochem. Soc.* 117 (1970) 588-592.

[10] J. Bressan, R. Wiart, Use of Impedance Measurements for the Control of the Dendritic Growth of Zinc Electrodeposits, *J. Appl. Electrochem.* 7 (1977) 505-510.

[11] P.A. Nikolaychuk, The Revised Potential – pH Diagram for Pb – H_2O system, *Ovidius Univ. Ann. Chem.* 29 (2018) 55-67.

[12] C. Izutani, D. Fukagawa, M. Miyasita, M. Ito, N. Sugimura, R. Aoyama, T. Gotoh, T. Shibue, Y. Igarashi, H. Oshio, The Materials Characterization Central Laboratory: An

Open-Ended Laboratory Program for Fourth-Year Undergraduate and Graduate Students. *J. Chem. Educ.* 93 (2016) 1667-1670.

[13] P. Giannozzi, S. Baroni, N. Bonini, M. Calandra, R. Car, C. Cavazzoni, D. Ceresoli, G. L. Chiarotti, M. Cococcioni, I. Dabo et al., QUANTUM ESPRESSO: a Modular and Open-Source Software Project for Quantum Simulations of Materials, *J. Phys.: Condens. Mater.* 21 (2009) 395502.

[14] P. Giannozzi, O. Andreussi, T. Brumme, O. Bunau, M. B. Nardelli, M. Calandra, R. Car, C. Cavazzoni, D. Ceresoli, M. Cococcioni et al., Advanced Capabilities for Materials Modeling with QUANTUM ESPRESSO, *J. Phys.: Condens. Matter* 29 (2017) 465901.

[15] S. Nishihara, M. Otani, Hybrid Solvation Models for Bulk, Interface, and Membrane: Reference Interaction Site Methods Coupled with Density Functional Theory, *Phys. Rev. B* 96 (2017) 115429.

[16] W. Kohn, L. J. Sham, Self-Consistent Equations Including Exchange and Correlation Effects, *Phys. Rev.* 140 (1965) A1133-A1138.

[17] D. Vanderbilt, Soft Self-Consistent Pseudopotentials in a Generalized Eigenvalue Formalism, *Phys. Rev. B* 41 (1990) 7892-7895.

[18] A. M. Rappe, K. M. Rabe, E. Kaxiras, J. D. Joannopoulos, Optimized Pseudopotentials, *Phys. Rev. B* 41 (1990) 1227-1230.

[19] J. P. Perdew, K. Burke, M. Ernzerhof, Generalized Gradient Approximation Made Simple, *Phys. Rev. Lett.* 77 (1996) 3865-3868.

[20] H. J. Monkhorst, J. D. Pack, Special Points for Brillouin-Zone Integrations, *Phys. Rev. B* 13 (1976) 5188-5192.

[21] M. Otani, O. Sugino, First-Principles Calculations of Charged Surfaces and Interfaces: A Plane-Wave Nonrepeated Slab Approach, *Phys. Rev. B* 73 (2006) 115407.

[22] K. Kovalenko, F. Hirata, Self-Consistent Description of a Metal-Water Interface by the Kohn-Sham Density Functional Theory and the Three-Dimensional Reference Interaction Site Model, *J. Chem. Phys.* 110 (1999) 10095-10112.

[23] H. J. C. Berendsen, J. P. M. Postma, W. F. von Gunstaren, J. Hermans, Interaction Models for Water in Relation to Protein Hydration, *In Intermolecular Forces, B. Pullman, Ed., Dordrecht Reidel Publishing company, Holland* (1981) pp 331-342.

[24] W. L. Jorgensen, J. Tirado-Rives, The OPLS Potential Functions for Proteins. Energy

Minimizations for Crystals of Cyclic Peptides and Crambin, *J. Am. Chem. Soc.* 110 (1988) 1657-1666.

[25] W. L. Jorgensen, D. S. Maxwell, J. Tirado-Rives, Development and Testing of the OPLS All-Atom Force Field on Conformational Energetics and Properties of Organic Liquids, *J. Am. Chem. Soc.* 118 (1996) 11225-11236.

[26] H. Heinz, R. A. Vaia, B. L. Farmer, R. R. Naik, Accurate Simulation of Surfaces and Interfaces of Face-Centered Cubic Metals Using 12-6 and 9-6 Lennard-Jones Potentials. *J. Phys. Chem. C* 112 (2008) 17281-17290.

[27] T. Otani, M. Nagata, Y. Fukunaka, T. Homma, Morphological Evolution of Mossy Structures during the Electrodeposition of Zinc from an Alkaline Zincate Solution, *Electrochim. Acta* 206 (2016) 366-373.

[28] T. Mitsuhashi, Y. Ito, Y. Takeuchi, S. Harada, T. Ujihara, Non-Uniform Electrodeposition of Zinc on the (0001) Plane, *Thin Solid Films* 590 (2015) 207-213.

[29] I. Danaee, F. Shoghi, M. D. Mobarake, M. Kameli, Electrocrystallization of Palladium from $Pd(NH_3)_4Cl_2$ Bath on Stainless Steel 316L, *J. Solid State Electrochem.* 14 (2010) 57-62.

[30] P. T. Gilbert, The Nature of Zinc Corrosion Products, *J. Electrochem. Soc.* 99 (1952) 16-21.

[31] T.B. Massalski, H. Okamoto, Binary Alloy Phase Diagrams. ASM internationa, Materials Park, Ohio, 1990.

[32] J. O'M Bockris, Z. Nagy, A. Damjanovic, On the Deposition and Dissolution of Zinc in Alkaline Solutions, *J. Electrochem. Soc.* 119 (1972) 285-295.

[33] C. Cachet, B. Soïdani, R. Wiart, The Behavior of Zinc Electrode in Alkaline Electrolytes I. A Kinetic Analysis of Cathodic Deposition, *J. Electrochem. Soc.* 138 (1991) 678-687.

[34] Y.-C. Chiu, M. A. Genshaw, A Study of Anion Adsorption on Platinum by Ellipsometry, *J. Pjys. Chem.* 73 (1969) 3571-3577.

[35] T. Otani, Analysis and Control of Interfacial Processes of Zn Negative Electrodes for Large-Scale Battery, *Waseda University* (2019) Doctoral dissertation.

[36] J. Y. Lee, M. P. J. Punkkinen, S. Schönecker, Z. Nabi, K. Kádas, V. Zólyomi, Y. M. Koo, Q. M. Hu, R. Ahuja, B. Johansson, J. Kollár, L. Vitos, S. K. Kwon, The surface

energy and stress of metals. Surface Science 674 (2018) 51-68.
[37] E. P. Kamphaus, S. Angarita-Gomez, X. Qin, M. Shao, M. Engelhard, K. T. Mueller, V. Murugesan, P. B. Balbuena, Role of Inorganic Surface Layer on Solid Electrolyte Interphase Evolution at Li-Metal Anodes, *ACS Appl. Mater. Interfaces* 11 (2019) 31467-31476.]

Chapter 6:

General Conclusions

With the growing demand for safe and inexpensive large-scale energy storages in view of the stable supply of renewable energy and efficient operation of electrical grid such as the concept of demand response, secondary batteries using the Zn negative electrode have attracted much attention as the post-Li-ion batteries. A challenge to its application in the society is the irregular shape evolution on the negative electrode during charging. In particular, an irregular deposition structure called mossy structure appears at low overpotential conditions, showing the growth of the micro-sized layer-by-layer structures in the early stage of its deposition. However, the key factor for the layer-by-layer structures are still unclear though it is necessary to understand the growth process as the initial step. Since phenomena during electrodeposition proceed on multiscale, from atomic reaction to growth at nano-level, it is challenging to understand the mechanisms using a single method in detail. In order to extend the analysis to the nano- to micro-scale phenomena, the Kinetic Monte Carlo (KMC) simulation is a useful tool because it can reproduce the motion of individual atoms based on the parameters obtained from first-principles calculations. In addition, the combination of Effective Screening Medium (ESM) and Reference Interaction Site Model (RISM) that can treat the solid-liquid interface in the first-principles calculations can be applied to obtain the parameters of KMC with the information of the electronic state. This dissertation aims to clarify the dominant factor in the growth mechanism of the layer-by-layer structures at the initial stage of the deposition on the Zn negative electrode, and to provide insight into the guideline for the suppression of the irregular shape evolution. The Zn growth process in electrodeposition was studied by complementing multiscale simulations using first-principles calculations and KMC simulations based on the ESM-RISM method with experimental analysis, and the mechanism of the effect of additives at the solid-liquid interface was also investigated.

This chapter summarizes the results obtained in each chapter and show the significant factor for the Zn shape evolution from the multiscale viewpoint to provide valuable insight for future guidelines for morphological control of Zn negative electrodes.

In Chapter 2, a multi-scale simulation with the density functional theory (DFT) calculations based on the first-principles calculations was constructed and utilized to

analyze the mechanism of the layer-by-layer structures depositing under irregular shape deposits with the aim of analyzing the growth mechanism and identifying its dominant factors during the initial stage of Zn electrodeposition on the Zn negative electrode.

The results of DFT calculations revealed that the surface diffusion at smooth Zn(0001) is rapid and the interlayer diffusion at the step-edge structures of Zn(0001) is moderately slow. The KMC simulations with the parameters indicated that this specific surface diffusion behavior of Zn causes the layer-by-layer structures at the nanometer scale, which was also observed in the experiments. Furthermore, the shape evolution after the deposition of the layer-by-layer structures is discussed to propose the hypotheses of the growth mechanism and plans for further analysis. From the analysis of this chapter, it is concluded that the specific surface diffusion behavior of Zn adatoms on the smooth Zn(0001) surface and the step-edge structure is a dominant factor in the shape evolution of the layer-by-layer structures.

In Chapter 3, the electronic state of the Zn adsorbed atom and surface is analyzed by DFT in order to clarify the origin of the specific surface diffusion behavior of Zn proposed in Chapter 2.

The results of the local density of states revealed that the specific surface diffusion behavior originated from the weak interaction of the 3d orbitals in Zn due to the stability of the 4s orbitals because a fully occupied state of electron configuration of Zn with $3d^{10}$ $4s^2$ are stable. This results in the rapid surface diffusion on the densely packed plane surfaces. Furthermore, the interaction between the 3d orbitals of the surface and adsorbed atoms is stronger at the step-edge structures, suggesting the origin of the high activation energy in the interlayer diffusion. From this analysis, the orbital interaction in the fully occupied orbitals of Zn was found to be the origin of the specific surface diffusion behavior of Zn.

In Chapter 4, Zn electrodeposition with the Li^+ addition was analyzed by multi-scale simulations constructed in Chapter 2 and electrochemical measurements to clarify the effect of Li^+ as an additive that exhibits its effect from the liquid phase side at the solid-liquid interface.

The comparison with the K^+ condition suggests that the effect of the Li^+ addition lies in the change of the solvation structure in the vicinity of the surface. This decreases the activation energy of surface diffusion at high-index surfaces such as the step-edge structure and (0−110) surface. In the Li^+ condition, the simulations and experiments indicated the preferential growth of the layer-by-layer structures. This analysis suggests a mechanism for the Zn deposition with the Li^+ addition: Li^+ forms large solvation spheres with water molecules and alters the interaction between the surface and water molecules, thereby mitigating the effect to interfere the surface diffusion. Consequently, the activation energy for the interlayer diffusion is lowered with the Li^+ addition. As proposed in Chapter 2, surface diffusion on the flat Zn(0001) surface and the interlayer diffusion are significant in the Zn shape evolution. The change in behavior of the interlayer diffusion due to the Li^+ addition results in the larger are of the layer-by-layer structures. These simulation and experimental results provide insight into the working mechanism of additives affecting the liquid phase at the solid-liquid interface.

In Chapter 5, in order to understand the working mechanism of the additive, which is electrodeposited earlier than Zn, the Zn deposition behavior with the Pb additive was analyzed by the electrochemical measurements and first-principles calculations.

The Zn electrodeposition from the solution with Pb suggest yielded a characteristic Zn pillar-like structure, which is deposited only when both Pb and Zn are present in solution with a crystal orientation of the Zn(0−110) plane on its sidewalls and the Zn(0001) plane on the bottom. Based on the hypothesis that Pb(111) covers on Zn, the Pb-coated Zn surface model constructed suggested that the deposited Zn atoms can pass through the Pb-covered layer and reach bulk Zn thermodynamically. This behavior can be attributed to the difference that the surface energy of the Pb(111) plane is smaller than that of the Zn(0001) plane. This difference in surface energy allows Pb to exist on the surface and also allows deposited Zn atoms to be incorporated into the interior. Moreover, the other possibilities of the existence of the Pb deposits are hypothesized and discussed how it is verified. Through the discussion, the strategy to control the morphological change is proposed for further analysis. At the end of the chapter, the contribution to the large-scale energy storage is discussed. These experiments and first-principles calculation

analyses clarified the behavior of deposited Zn at the atomic level and provided useful insight for investigating the working mechanism of additives that exhibit their effects on the surface.

This dissertation focused on the Zn growth process on Zn negative electrodes from the atomic and molecular level to the nanoscale by a complementary combination of multiscale simulations and experiments to identify the dominant factors in layer-by-layer structures at the initial stage of the Zn deposition, which provide insight for the development of the controlling condition of the Zn shape evolution. These analyses extend the scale of analysis for the initial stage of electrodeposition. In addition, it provides valuable insight for investigating nanoscale phenomena from the electronic state perspective. The investigation of working mechanism of additives at the atomic and molecular level indicated that the behavior of the deposited Zn atoms on the surface are significantly affected by the physical properties such as the solvation and surface energy. This research will be helpful for developing conditions to control the morphology of the Zn negative electrode during charging.

List of Achievements

1. Original Articles

"Multiscale Simulation of Irregular Shape Evolution during the Initial Stage of Zn Electrodeposition on a Negative Electrode Surface"
Yusuke Onabuta, Masahiro Kunimoto, Songyi Wang, Yasuhiro Fukunaka, Hiromi Nakai, Takayuki Homma
Journal of Physical Chemistry C 126 (March 2022) 5224-5232.
(https://doi.org/10.1021/acs.jpcc.1c09569)

"Analysis of the Behavior of Zn Atoms with Pb Additive on the Surface during Zn Electrodeposition"
Yusuke Onabuta, Masahiro Kunimoto, Fumimasa Ono, Yasuhiro Fukunaka, Hiromi Nakai, Giovanni Zangari, Takayuki Homma
Electrochemistry Communications 138 (May 2022) 107291.
(https://doi.org/10.1016/j.elecom.2022.107291)

2. Presentations

[International Conference]

"Effect of Additive Species on the Nucleation and Growth Process on Zn Negative Electrode Surface"
Takayuki Homma, Yusuke Onabuta, Tomohiro Otani, Masahiro Kunimoto, Yasuhiro Fukunaka
241st ECS Meeting, Vancouver, Canada, June 2022.

"A DFT and KMC Study for the Shape Evolution at the Initial Stage of the Zn Electrodeposition"
Yusuke Onabuta, Masahiro Kunimoto, Songyi Wang, Yasuhiro Fukunaka, Hiromi Nakai, Takayuki Homma
INTERFINISH2020 20th World Congress, Online, September 2021.

"Multiscale Simulation for Effects of the Li^+ Addition at the Initial Stage of Zn Electrodeposition Processes"
Yusuke Onabuta, Songyi Wang, Masahiro Kunimoto, Hiromi Nakai, Takayuki Homma
Pacific Rim meeting on Electrochemical &Solid-State Science (PRiME2020), Honolulu, U.S. (online), October 2020.

"Multiscale Simulation for Initial Stage of the Zn Electrodeposition with Kinetic Monte Carlo Based on First-Principle Calculation"
Yusuke Onabuta, Kosuke Onuki, Songyi Wang, Masahiro Kunimoto, Hiromi Nakai, Takayuki Homma
237th ECS Meeting with the 18th International Meeting on Chemical Sensors (IMCS 2020), Montréal, Canada (cancelled), May 2020.

[Domestic Conferences]

"Theoretical Analysis of the Effect of Heavy Metal Additives for the Adsorption Behavior of Zn Atoms during Zn Electrodeposition Process"
Fumimasa Ono, Yusuke Onabuta, Masahiro Kunimoto, Hiromi Nakai, Takayuki Homma
145th Meeting of the Surface Finishing Society of Japan, Satitama (Online), March 2022.

"Analysis of Surface Diffusion Behavior and Electronic State of Zn Atoms during Zn Electrodeposition Process"
Songyi Wang, Yusuke Onabuta, Masahiro Kunimoto, Hiromi Nakai, Takayuki Homma
ECSJ Fall Meeting, 2021, Online, September 2021.

"Multiscale Simulation of Shape Evolution on Zn Negative Electrodes in the Early Stage of Electrodeposition"
Yusuke Onabuta
2nd Web Conference on Non-ferrous Extractive Metallurgy, Online, January 2021.

"First-Principles Calculations and Kinetic Monte Carlo study of Surface Diffusion of Zn Atoms in the Early Stage of Zn Electrodeposition"
Yusuke Onabuta, Kosuke Onuki, Songyi Wang, Masahiro Kunimoto, Hiromi Nakai, Takayuki Homma
The 87th ECSJ Spring Meeting, Aichi (cancelled), March 2020.

"First-Principles Analysis of Zn Atom Surface Diffusion Behavior during Zn Electrodeposition"
Songyi Wang, Yusuke Onabuta, Kosuke Onuki, Masahiro Kunimoto, Hiromi Nakai, Takayuki Homma
141st Meeting of the Surface Finishing Society of Japan, Tokyo (cancelled), March 2020.

3. Others

[Academic Papers]

"First-Principle Study of the Oxidation Mechanism of Formaldehyde and Hypophosphite in the Electroless Deposition Process"
Yusuke Onabuta, Masahiro Kunimoto, Hiromi Nakai, Takayuki Homma
Electrochimica Acta, 307 (March 2019) 536-542.
(https://doi.org/10.1016/j.electacta.2019.03.150)

[International Conferences]

"DFT Analyses of the Facilitating Effect of Water on Interfacial Reactions"
Masahiro Kunimoto, Yusuke Onabuta, Hiromi Nakai, Masahiro Yanagisawa, Takayuki Homma
Materials Research Meeting 2021, Kanagawa, December 2021.

"First-Principle Study of the Oxidation of Formaldehyde and Hypophosphite as Reducing Agents in Electroless Deposition"
Yusuke Onabuta, Masahiro Kunimoto, Hiromi Nakai, Takayuki Homma
9th Jilin-Korea-Waseda Alliance Annual Symposium, Jilin, China, August 2019.

"Molecuar-Level Analysis of Electrodeposition Processes Using Theoretical Calculations and Surface Enhanced Raman Microscopy"
Takayuki Homma, Masahiro Kunimoto, Yusuke Onabuta, Morten Bertz, Masahiro Yanagisawa
235th Meetings of the Electrochemical Society (235th ECS Meeting), Dallas, U.S., May 2019.

"First-Principle Study of the Oxidation of Formaldehyde and Hypophosphite As Reducing Agents in Electroless Deposition"
Yusuke Onabuta, Masahiro Kunimoto, Hiromi Nakai, Takayuki Homma
Joint Symposium of Peking University & Waseda University on Energy and Nanomaterials, Beijing, China, January 2019.

"First-Principle Study of the Oxidation of Formaldehyde and hypophosphite as Reducing Agents in Electroless Deposition"
Yusuke Onabuta, Masahiro Kunimoto, Hiromi Nakai, Takayuki Homma
6th DIGIST-WASEDA Workshop on Electrochemistry, Daegu, Republic of Korea, November 2018.

"First-Principles Study of Catalytic Activity of Cu, Ni and Pd Surface for Formaldehyde and Hypophosphite As Reducing Agents in Electroless Deposition"
Yusuke Onabuta, Masahiro Kunimoto, Hiromi Nakai, Takayuki Homma
ECS and SMEQ Joint International Meeting (AiMES2018), Cancun, Mexico, October 2018.

"First-Principles Study of Reaction Mechanism of Reducing Agents on Ni and Cu in Electroless Deposition Processes"
Yusuke Onabuta, Masahiro Kunimoto, Hiromi Nakai, Takayuki Homma
22nd Topical Meeting of the International Society of Electrochemistry, Tokyo, April 2018.

[Domestic Conferences]

"First-Principles Analysis of Formaldehyde and Hypophosphite Oxidation in Electroless Deposition Processes"
Yusuke Onabuta, Kochi Shinozaki, Masahiro Kunimoto, Hiromi Nakai, Takayuki Homma
139th Meeting of the Surface Finishing Society of Japan, Kanagawa, March 2019.

"Theoretical Analysis of Formaldehyde Oxidation Reaction Process in Electroless Deposition Process by AIMD"
Kochi Shinozaki, Yusuke Onabuta, Masahiro Kunimoto, Hiromi Nakai, Takayuki Homma
139th Meeting of the Surface Finishing Society of Japan, Kanagawa, March 2019.

"First-Principles Analysis of Solvent Effect on Reductant Oxidation Process in Electroless Precipitation"
Yusuke Onabuta, Masahiro Kunimoto, Hiromi Nakai, Takayuki Homma
138th Meeting of the Surface Finishing Society of Japan, Hokkaido (cancelled), September 2018.

"Theoretical Analysis of the Interaction between Formaldehyde and Thiourea in the Electroless Cu Deposition Process"
Yusuke Onabuta, Masahiro Kunimoto, Hiromi Nakai, Takayuki Homma
135th Meeting of the Surface Finishing Society of Japan, Saitama, March 2017.

4. Awards

Best Poster Presentation Award, 6th DGIST-Waseda Workshop on Electrochemistry, November 2018.

Best Poster Award, ECSJ Kanto-branch 36th summer school, August 2018.

Acknowledgment

I am sincerely grateful to Professor Dr. Takayuki Homma for his kind support. He has made my research ability deepen with valuable advice since I joined in the Lab. I received his greatest help when I was in difficult situations. I have learned a lot of things that will help me for my next stage.

I would like to thank Professor Dr. Toshiyuki Momma, Professor Dr. Kenji Miyataka (Yamanashi University), and Dr. Kenich Uemura (NIPPON STEEL Chemical & Material CO, LTD.) for their advice on this Dissertation. Their comments gave me new insights and made this research more valuable.

I appreciate valuable advice from Professor Dr. Izumi Hirasawa, Professor Dr. Kenichi Oyaizu, Professor Dr. Suguru Noda, Professor Dr. Yoshiyuki Sugahara. This dissertation is greatly improved by their comments from deep insight.

I would like to express my gratitude to Professor Dr. Hiromi Nakai. He gave me a lot of advice from the viewpoint of computational chemistry while I was working on an experimental system. I believe that his advice has broadened my viewpoint as a researcher and will be a source of inspiration for me in the future.

I would also like to express my gratitude to Professor Dr. Akihiko Fukunaga. I received many comments on a daily basis, which were helpful for my research.

I could not have achieved the results of Chapter 5 without the discussions with Professor Dr. Giovanni Zangari. Even under these difficult circumstances, we had a lot of time for online discussions. It was really valuable time.

I would also like to thank Professor Dr. Yasuhiro Fukunaka gave me the inspiration for the KMC program, which was the cornerstone of this research. This helped me to see a direction for my research.

I appreciate his kind help from Dr. Masahiro Kunimoto. We discussed all the results obtained. He taught me a lot of the basics of electrochemistry and quantum chemistry. I also received a lot of support for my life in the Lab. Dr. Mahmudul Md. Hasan, a staff member, also supported me for a short period of time.

I would also like to thank the members of the Lab. Senior ex-colleagues of the Ph.

D. course, Dr. Siggi Wodarz, Dr. Yasuhiro Tsuyuki, Dr. Tomohiro Otani, Yelchur Venkata Akash, and Dr. Tatsuki Fujimura gave me advice from a wide range of viewpoints. I also appreciate a help from a Ph. D. candidate, Tanyanyu Wang. We helped each other to advance our research. In addition, I woulk like to appreciate daily discussions with Ph. D. course members, Kohei Ide, Collen Takaza, and Kohei Yasuda.

I would also like to thank all the laboratory members. Especially, I would like to express my appreciation to the members of the modeling group, Ayumu Sanada, Kosuke Onuki, Kochi Shinozaki, Daiki Nishikawa, Songyi Wang, Takuya Tsubokawa, Fumimasa Ono, and Momoka Yamano. I would like to thank all the members of Nakai laboratory, especially Dr. Mikito Fujinami, Chinami Takashima, and Ryo Fujisawa for their support.

Finally, I am grateful to my parents and grandparents. Full of their support lead this research to be achieved.

July, 2022
Yusuke Onabuta